CrossMark

ORIGINAL PAPER

Bi-directional Evolutionary Structural Optimization on Advanced Structures and Materials: A Comprehensive Review

Liang Xia[1] · Qi Xia[1] · Xiaodong Huang[2] · Yi Min Xie[2]

Abstract The evolutionary structural optimization (ESO) method developed by Xie and Steven (Comput Struct 49(5):885–896, 1993), an important branch of topology optimization, has undergone tremendous development over the past decades. Among all its variants, the convergent and mesh-independent bi-directional evolutionary structural optimization (BESO) method developed by Huang and Xie (Finite Elem Anal Des 43(14):1039–1049, 2007b) allowing both material removal and addition, has become a widely adopted design methodology for both academic research and engineering applications because of its efficiency and robustness. This paper intends to present a comprehensive review on the development of ESO-type methods, in particular the latest convergent and mesh-independent BESO method is highlighted. Recent applications of the BESO method to the design of advanced structures and materials are summarized. Compact Malab codes using the BESO method for benchmark structural and material microstructural designs are also provided.

✉ Liang Xia
liang.xia@utc.fr

✉ Qi Xia
qxia@hust.edu.cn

1   The State Key Laboratory of Digital Manufacturing Equipment and Technology, Huazhong University of Science and Technology, Wuhan, China

2   School of Engineering, RMIT University, GPO Box 2476, Melbourne, VIC 3001, Australia

1 Introduction

We observe over the past decades that topology optimization has undergone a remarkable development in both academic research [10, 23, 56] and industrial applications [187]. By topology optimization, one aims to find an optimal material layout within a prescribed design domain so as to maximize or minimize certain objectives meanwhile satisfying one or multiple design constraints. The most examined design case is to minimize structural compliance, i.e., maximize stiffness, subject to a volume constraint on material usage. An illustration of topology optimization is given in Fig. 1. The key merit of topology optimization over conventional shape or sizing optimizations is that the structural topology or the material layout inside the design domain is not a priori assumed, resulting much increased design freedom and consequently leading to in most cases more efficient designs.

The prior investigation of topology optimization can be traced back to over a hundred years ago by the versatile Australian inventor Michell [91], who derived optimality criteria for the least-weight layout of trusses. Michell's theory was extended until 70 years later by Rozvany and his collaborators [103, 116, 117] for exact analytical optimal solutions of grid-type structures. Numerical investigations on topology optimization started afterwards along with the revolutionary development of computing capabilities and the advancement of numerical simulation methods. Within the continuum framework, topology optimization can be formulated as a discrete problem or a binary design setting that the structure consists solely solid material or void. However, the binary setting for structural compliance designs is known as ill-posed that there exist non-convergent sequence of admissible designs with continuously refined geometrical details [17, 71–73]. Bendsøe

🗘 Springer
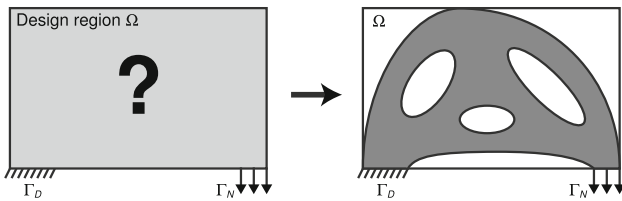
Fig. 1 Illustration of typical structural topology optimization [149]

and Kikuchi [8] proposed to relax the problem by assuming designable porous microstructures at a separated lower scale upon the homogenization theory such that the problem becomes well-posed. This paper is also recognized as the seminal paper to numerical topology optimization. Since then topology optimization has undergone remarkable development with the emergence of various methods, including in chronological sequence: density-based methods [7, 184], evolutionary procedures [161, 162], bubble method [27], topological derivative [130], level-set methods [1, 84, 122, 142, 153–158] and phase field method [11]. All these approaches are based on repeated numerical simulations and according to the updating mechanisms they can be categorized in general into two groups: either density variation or shape/boundary variation. Reviews on specific topology optimization methods have been given by Rozvany [120] for density-based methods, by Huang and Xie [55] for ESO-type methods, by van Dijk et al. [137] for level-set methods and by Deaton and Grandhi [23] for a general review on various methods and their applications. Sigmund and Maute [127] have presented a critical review and comparison on various methods.

As an important branch of topology optimization, the evolutionary structural optimization (ESO) method was initially proposed by Xie and Steven [161, 162] based on a simple concept that a structure evolves towards an optimum by gradual removing lowly stressed materials. The ESO method was also recognized as a hard-kill method and the associated discrete design space is not relaxed in contrast to density-based methods. The ESO method has been extended for various design objectives using either heuristic or empirical criteria, which may or may not be based on sensitivity information [164]. It has been reported that the ESO method is equivalent to a sequential linear programming approximate method when the strain energy is adopted as the update criterion [135]. A summary of the early developments of the ESO-type methods can be found in the first book on the subject by Xie and Steven [164].

Querin et al. [105, 107, 108] developed the early versions of bi-directional evolutionary structural optimization (BESO) method allowing the recovery of the deleted elements which are neighboring to highly stressed elements. One of the last major development of the ESO method is the proposition of the convergent and mesh-independent BESO method by Huang and Xie [48], which has incorporated a sensitivity filter scheme and a stabilization scheme using the history information. The latest version of BESO method has shown promising performance when applying for a wide range of structural design problems including stiffness and frequency optimization [59], nonlinear material and large deformation [47, 52], energy absorption [58], multiple materials [53], multiple constraints [54], periodic structures [50], and so on [55, 144]. The second phase development of the ESO method (the extension to bi-directional) and the various applications up to the year 2010 have been summarized in the second book on the subject by Huang and Xie [56].

The BESO method has been showing efficient and robust performance and has become a widely adopted design methodology for both academic researches and engineering applications. This paper intends to provide a comprehensive review on the development of ESO-type methods, meanwhile summarizes recent applications of the BESO method for the design of advanced structures and materials, in particular the contributions after the year of 2007. This review is organized as follows: Sect. 2 gives first a comprehensive review on the historical development of ESO-type methods from the original proposition of the ESO method [162] to the latest BESO method [48]; Sect. 3 provides a discussion on the famous Zhou–Rozvany problem [183]; Sect. 4 summarizes recent BESO applications for the design of advanced structures; Sect. 5 summarizes recent BESO applications for the design of material microstructures; Sect. 6 summarizes recent BESO applications for the design of multiscale structures; Sect. 7 presents two Malab codes using the BESO method together with benchmark tests on design of structures and material microstructures; conclusion is drawn in Sect. 8.

2 Historical Review on ESO/BESO Methods

Since the late 1980s, enormous progress has been made in the theory, methods and applications of topology optimization. Among various numerical methods for topology optimization, ESO/BESO methods have been extensively investigated by many researchers around the world. The first book on ESO was published by Xie and Steven in 1997 [164]. Since then the field has experienced rapid developments with a variety of new algorithms and a growing number of applications. There are many different versions of ESO/BESO algorithms proposed by several dozens of researchers in the past two decades. However, some of the algorithms appeared in the literature are unreliable and inefficient. This section provides a comprehensive and systematic discussion on the latest techniques and proper procedures for ESO/BESO, particularly the latest

convergent and mesh-independent BESO method with a presentation of the standard design procedure for continuum structures.

2.1 Original ESO Proposition

The evolutionalry structural optimization (ESO) method was originally proposed by Xie and Steven in the early 1990s [162] and has since been continuously for a wide range of topology optimization problems [164]. By observing the evolution of naturally occurring structures such as shells, bones and trees it becomes obvious that the topology and shape of such structures achieve their optimum over a long evolutionary period and adapt to whatever environment they find themselves in. With this idea in mind, the ESO method was originally proposed using the stress level as an indicator for the gradual removal of inefficient material for a structure expecting that the resulting structure could evolve towards an optimal shape and topology.

By means of a numerical simulation method, e.g., the mostly applied finite element method, the stress field of a loaded structure can be easily determined. Ideally an evenly distributed stress field is expected within the structural domain for an optimal use of material, however it is often not the case indicating the existence of inefficient material. This observation leads to the original ESO proposition that lowly stressed material is assumed to be inefficiently used and is therefore removed gradually according to a defined rejection criterion based on the local stress level. The removal of material was undertaken by deleting elements from the finite element model of the structure, for which the original ESO method is also known as a hard-kill method.

In the original ESO proposition [162], the stress level of each element is determined by comparing the element von Mises stress σ_e^{vm} with a prescribed critical or maximum von Mises stress of the whole structure σ_{max}^{vm}. A rejection ratio (c_{rr}) is defined and elements with von Mises stress lower the threshold are deleted or removed from the model

$$\sigma_e^{vm} < c_{rr} \cdot \sigma_{max}^{vm}. \tag{1}$$

The cycle of finite element analysis and element removal is repeated for several iterations using the same rejection ratio until a steady state is reached, meaning that there are no more elements satisfying this deletion threshold. The rejection ratio can then be increased according to a defined evolutionary rate c_{er}

$$c_{rr}^{new} = c_{rr}^{old} + c_{er} \tag{2}$$

and the iteration process takes place again until a new steady state is reached. The evolutionary process continues until a desired optimum is reached, for example, the stress

level of all material are below the precribed ratio of the maximum von Meses stress σ_{max}^{vm}.

Figure 2 shows the results of the evolutionary design procedure of a two-bar frame structure [162]. The dimensions of the two-bar frame structure is 10×24 m^2 and the thickness is 0.001 m. The left hand side of the structure is fully clamped and a shear stress of 1 MPa is applied on the
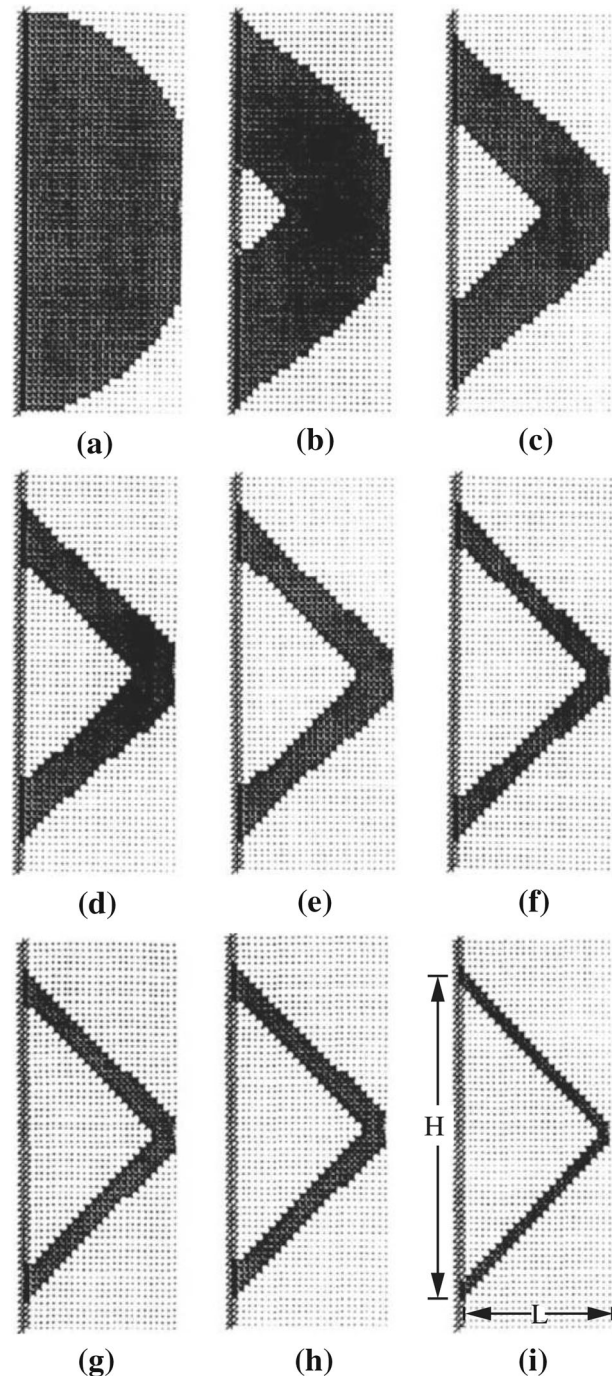

Fig. 2 ESO topologies for a two-bar frame for different rejection ratios [162]: **a** $c_{rr} = 3\%$, **b** $c_{rr} = 6\%$, **c** $c_{rr} = 9\%$, **d** $c_{rr} = 12\%$, **e** $c_{rr} = 15\%$, **f** $c_{rr} = 18\%$, **g** $c_{rr} = 21\%$, **h** $c_{rr} = 24\%$, **i** $c_{rr} = 30\%$

edge of two elements at the center of the right hand side. The whole structure is discretized into 25×60 uniform bilinear quadrilateral plane stress elements. The Young's modulus $E = 100$ GPa and the Poisson's ratio $v = 0.3$ are assumed. The ESO procedure starts from the full design using an initial rejection ratio $c_{rr} = 1\%$. The evolutionary rate ER is also set to $c_{er} = 1\%$. The resulting topologies in Fig. 2 are the steady state topologies for gradually increasing rejection ratios. As the rejection ratio increases, more and more relatively inefficient material is removed from the structure. From the early stages of the evolution, it is clear that the structure is to evolve into a two-bar frame. The final two-bar system in Fig. 2i gives $H = 2L$ which agrees well with the analytical solution.

Another example of using the ESO method for shape optimization is given in Fig. 3, in which one seeks to find the optimal shape for an object hanging in the air under its own weight [164]. Two slots are cut at the top in the initial model to create a stalk, which is fixed at the top end. By gradually removing the least stressed material from the surface, a final shape with uniform stress on the surface is obtained. The result of in Fig. 3 reminds us of certain fruits such as an apple and a cherry.

The ESO method has been extended to topology optimization of structures with such constraints as buckling load [85], frequency [163], temperature [78] or a combination of the above [104]. The ESO method has also been used for various engineering applications such as the underground excavation [113]. A summary of early applications of the ESO method on different physical field problems have been given by Steven et al. [131]. It has also been shown that the ESO method provides a useful tool for engineers and architects who are interesting in exploring structurally efficient forms and shapes during the conceptual design stage of a project [164].

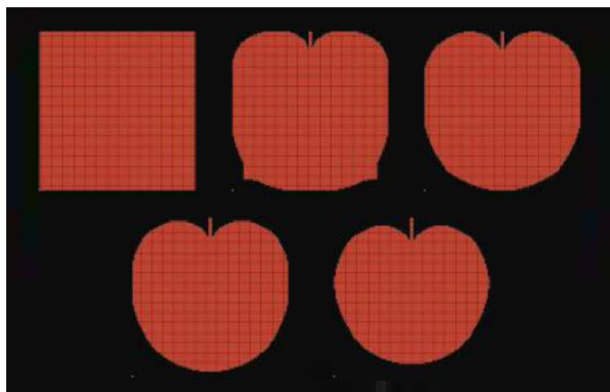To minimize the material usage under a given performance constraint, the ESO method seems to follow a

logical procedure to reduce the structural weight (or volume) by gradually removing inefficient material until the prescribed constraint can no longer be satisfied. However, it is possible that the material removed in the early evolution iterations might be required afterwards. The original ESO proposition is unable to recover the material once it has been prematurely or wrongly removed from the structure. Hence, while the ESO method is capable of producing a much improved solution over an initial guess design in most cases, the result may not necessarily be an optimum. Li et al. [76] and McKeown [87] have shown that such a fully stressed design by the ESO method is equivalent to that of the stiffness criterion, i.e. it cannot always minimize the highest stress in the structure.

2.2 Early Developments of BESO

The early ESO developments were limited by allowing only material removal from the structure, and those removed ones cannot be readmitted in the later evolution, an over-sized initial design setting is therefore required to ensure that the final design is represented by adequate elements. In certain cases the optimization is misled due to the inappropriately defined initial setting [106]. As complementary, a reverse method to the original ESO algorithm, namely additive ESO (AESO), was proposed by Querin et al. [105], by which the structure evolves from a base structure of little material by gradually adding material to highly stressed regions. Both ESO and AESO allow only one directional variation of the structural material layout by either material removal or material addition. The early version of bi-directional ESO (BESO) was proposed by Querin et al. [107] through a combination of ESO and AESO concepts. In their BESO algorithm, elements with the lowest von Mises stresses are removed satisfying the first criterion in Eq. (3), and void elements near the highest von Mises stress regions are switched on as solid elements satisfying the second equation in Eq. (3) where $\tilde{\sigma}_e$ is an approximation of the von Mises stress for void elements from neighboring solid elements. The numbers of elements to be removed and added are treated separately with a rejection ratio c_{rr} and an inclusion ratio c_{ir}, respectively. BESO allows for both material removal and addition, so that the final optimum can be reached regardless of how the initial design setting is defined. The optimality of the bi-directional ESO method was validated by Querin et al. [108].

$$\begin{cases} \sigma_e^{vm} < c_{rr} \cdot \sigma_{max}^{vm} \rightarrow \text{element removal}, \\ \tilde{\sigma}_e^{vm} > c_{ir} \cdot \sigma_{max}^{vm} \rightarrow \text{element addition}. \end{cases} \tag{3}$$

The same two-bar frame structure as presented previously in Fig. 2 was reexamined using the BESO method. In

Fig. 3 ESO solutions of an object hanging in the air under its own weight [164]

contrary to the full solid starting structure as shown in Fig. 2a, the BESO reexamination starts from a slender topology as shown in Fig. 4a. During the initial evolution iterations, elements were only added to the structure and the topologies produced had a quadratic outside shape (Fig. 4a–c). This is analogous of the equation for the optimal height of a cantilever beam subject to a single point load at the free end. As the structure continues to evolve, a cavity was subsequently created and the structure was split into two as shown in Fig. 4d. The BESO method evolved rapidly the structure afterwards to the well known classical optimal topology of Fig. 4f. It has been shown that for this 2D example, the BESO method is as efficient as the ESO method in terms of the required evolution time to reach the same optimal solution. As the design efficiency is highly dependent on the initial setting, by choosing a proper starting structural topology the BESO method ensures in general a quicker process than the ESO method.

Another initial research on BESO was conducted by Yang et al. [174] for stiffness optimization. In their study, the sensitivity numbers of the void elements are estimated through a linear extrapolation of the displacement field after the finite element analysis. The element sensitivity number α_e was defined as the variation of element compliance due to the removal or addition of the element [20]:

$$\alpha_e = \mathbf{u}_e^T \mathbf{k}_e \mathbf{u}_e \tag{4}$$

in which $\mathbf{u}_e$ and $\mathbf{k}_e$ are the element displacement vector and stiffness matrix, respectively. By ranking all elements using the corresponding sensitivity numbers, the solid elements with the lowest sensitivity numbers are removed from the structure, and the void elements with the highest sensitivity numbers are changed into solid elements. Figure 5 gives two optimal designs for two load cases using the BESO method for a lever arm, where the edge of the left hole is rigidly fixed and loads are applied at the edge of the right hole (point A). This method has been further extended to three-dimensional structures [180].

The early development of ESO/BESO methods are largely based on a heuristic concept and is lacking in theoretical rigor. Most of the early work on ESO /BESO neglected important numerical problems in topology optimization, such as existence of solution, checker-board, mesh-dependency and local optimum, etc. Continuous efforts were conducted to overcome these deficiencies, for instance: Li et al. [77] solved the checkerboard problem by averaging the sensitivity number of an element with the neighboring elements; Yang et al. [176] introduced a perimeter constraint to the BESO method; Kim et al. [68, 70] introduced cavity control techniques into the BESO method. With the purpose of reducing the computational effort, fixed grids have also been introduced to the BESO method [67, 69].
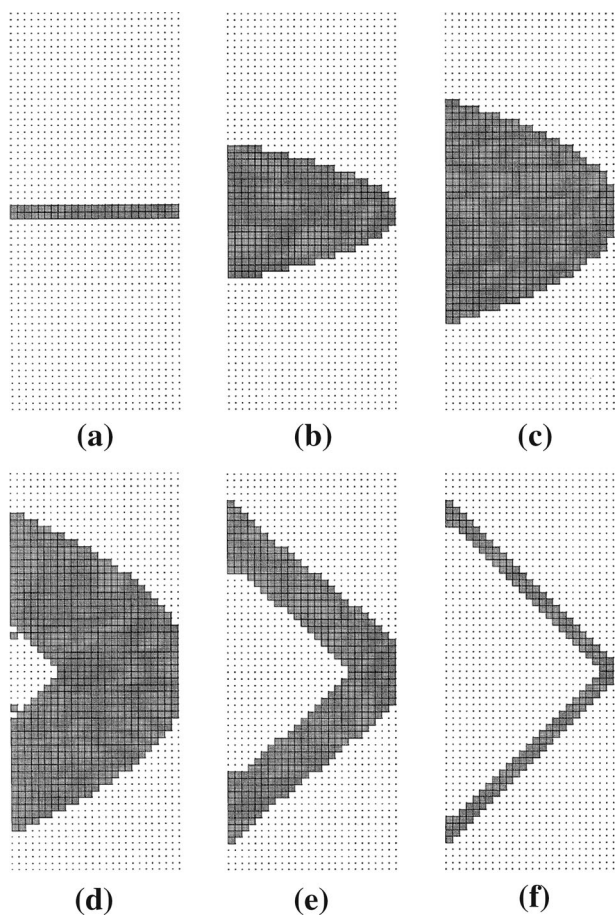

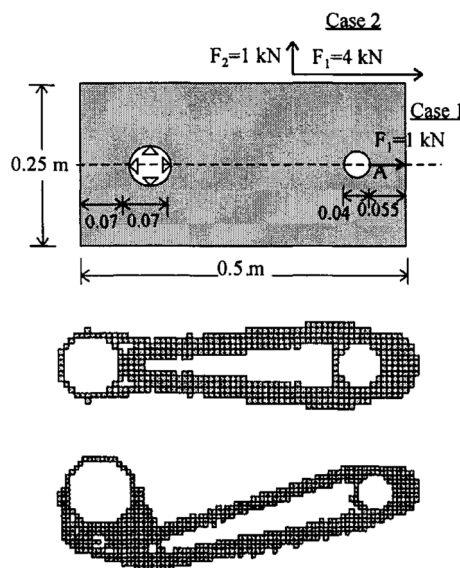**Fig. 4** BESO design for a two-bar frame [108]

Fig. 5 BESO stiffness designs of a lever arm: the problem setting, optimal design of load case 1 (tension), optimal design of load case 2 (tension and bending) from *top to bottom* [174]

2.3 Convergent and Mesh-Independent BESO

As indicated in the above, one obvious deficiency of the BESO method is mesh-dependency issue. The reason is that the introduction of more holes can always lead to a more efficient design. This effect is seen as a numerical instability where a larger number of holes appear when a finer finite element mesh is employed and it is termed as mesh dependence. This is in fact a common issue for almost all topology optimization methods not only to BESO [128]. The BESO method with perimeter control [176] has been shown to be capable of obtaining mesh-independent solutions due to the introduction of one extra constraint on the perimeter length. However, predicting the value of the perimeter constraint for a new design problem is not at all a trivial task.

Another problem is that ESO/BESO methods may result in a non-convergent solution [10, 12]. In other words, the solution may be worse and worse in terms of the objective function, e.g., compliance, if the ESO/BESO procedure continues without stop. That is one reason why the stop criterion in the original ESO/BESO method is defined with the objective volume rather than the objective function. Obviously, the solution using this type of ESO/BESO procedure is problematic when a broken member with no or low strain energy happens to be a part of the final topology [183].

To overcome the above-mentioned deficiencies, a modified and much improved BESO method was proposed by Huang and Xie [48]. The key contributions are twofold: firstly, the filter scheme is adopted to make sure the existence of the solution, meanwhile avoid the checkerboard pattern (see Fig. 6) and mesh-dependency issues; secondly, the sensitivity number is modified using the historical information to stabilize the optimization procedure. Different from the vague optimization setting in the previous ESO/BESO methods, this paper first clearly formulated the topology optimization problem with mean compliance objective subject to a volume constraint.

In order to avoid mesh-dependency and checkerboard patterns, sensitivity numbers are firstly smoothed by means of a filter scheme
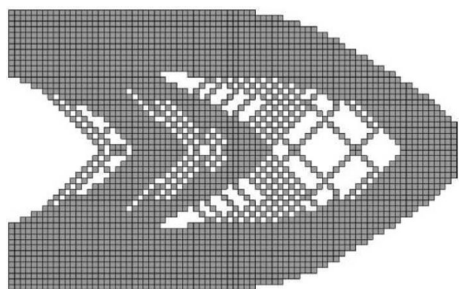

Fig. 6 A typical checkerboard pattern in the ESO method [56]

$$\alpha_e = \frac{\sum_{j=1}^{N_e} w_{ej} \alpha_j}{\sum_{j=1}^{N_e} w_{ej}}, \tag{5}$$

where w_{ej} is a linear weight factor

$$w_{ej} = \max(0, r_{\min} - \Delta(e, j)), \tag{6}$$

determined according to the prescribed filter radius $r_{\min}$ and the element center-to-center distance $\Delta(e, j)$ between elements Ω_e and Ω_j. Note that in the original proposition [48], the element sensitivity numbers are firstly distributed on nodes and the nodal sensitivity numbers are then used for the evaluation of the filtered element sensitivity numbers. The two schemes are somehow equivalent in piratical uses. Here in order to simply the notations, the element-based filter scheme is presented.

Attention needs to be paid here that the above filter scheme is similar to the mesh-independency filter used in [128] except that in Eq. (15) the element density is not included in the denominator. A schematic illustration of the filter scheme is shown in Fig. 7, where a checkerboard is filtered with $r_{\min} = 1.5$ and $r_{\min} = 3$ times element length l_e, respectively. It can be seen that the filter scheme smooths the sensitivity numbers in the whole design domain. Thus, the sensitivity numbers for void elements are automatically obtained. They may have high values due to high sensitivity numbers of the neighboring solid elements. Therefore, some of the void elements may be changed to solid elements in the next iteration.

The filter scheme is purely heuristic. However, by adopting this simple scheme, many numerical problems in topology optimization, such as checkerboard and mesh-dependency, can be effectively overcome. It produces results very similar to those obtained by applying a local gradient constraint [10]. The filter scheme requires little extra computational time and is very easy to implement in the optimization algorithm.

Despite the use of the filter scheme, the objective function and topology may not be convergent [56]. It attributes to the inaccurate assessment of sensitivity numbers especially for adding elements (originally void) which are not involved in the finite element analysis. With the purpose of circumventing this problem, the accuracy of the sensitivity numbers is further improved by considering the
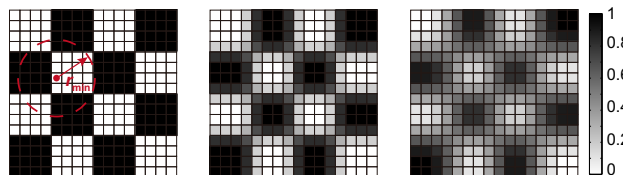

Fig. 7 A checkerboard two-phase field and the associated filtered fields ($r_{\min} = 1.5l_e$ and $3l_e$) [149]

sensitivity history of each element. A simple way to achieve this is to average the current sensitivity number with that of the previous iteration as [48, 52, 53]

$$\alpha_e^{(l)} \leftarrow (\alpha_e^{(l)} + \alpha_e^{(l-1)})/2, \tag{7}$$

where (l) and $(l-1)$ denote the current and the previous design iterations, respectively. Computational experience has shown that this heuristic stabilization scheme by averaging the sensitivity number with its historical information is an effective way to stabilize the design process and thus improve the convergence.

For the purpose of illustration, let us consider a stiffness maximization problem of a short cantilever, which is uniformly discretized into 32×20 quadrilateral bilinear elements. With the BESO method, large oscillations are often observed in the evolution history of the objective function, as illustrated in the Fig. 8a. The reason for such chaotic behavior is that the sensitivity numbers of the solid and void elements are based on discrete design variables of element presence and absence, which makes the objective function and the topology difficult to converge stably. Figure 8b shows the evolution history obtained with the adoption of the stabilization scheme defined in (17). Compared to the result in Fig. 8a, the new solution is

Fig. 8 Comparison of BESO topological evolution histories: **a** without the stabilization scheme; **b** with the stabilization scheme [48]

highly stable in both the topology and the compliance value once the volume fraction constraint (50%) is achieved. It is worth pointing out that whilst the stabilization scheme of (17) affects the search direction of the BESO algorithm it has negligible influence on the final topology design once it becomes convergent. Details of the parameters used for this example can be found in [48].

2.4 Soft-Kill BESO Method

The conventional BESO method is known as a "hard-kill" method due to the complete removal of inefficient elements. The main advantage of the hard-kill approach is that the computational time can be significantly reduced, especially in the 3D case, because the deleted elements are not involved in the subsequent finite element analyses. However, there have been some doubts among researchers about the theoretical correctness of the hard-kill ESO/BESO methods, especially after Zhou and Rozvany [183] has showed that the ESO/BESO methods fail on a certain design problem, known as "Zhou–Rozvany problem" (see Sect. 3). The complete removal of a solid element from the design domain could result in theoretical difficulties in topology optimization. It appears to be rather irrational when a design variable (an element) is directly deleted from the topology optimization problem.

An alternative effective way to "remove" an element is to reduce the elastic modulus of the element or one of the characteristic dimensions (such as the thickness) of the element to a very small value. For example, Hinton and Sienz [46] reduce the elastic modulus of elements which are to be "removed" by dividing a prescribed large factor. Rozvany and Querin [119] suggested a sequential element rejection and admission (SERA) method in which the void element is replaced by a soft element with a very low Young's modulus value. Zhu et al. [186] proposed to replace the void element by an orthotropic cellular microstructure. The prominent question is "does such an optimal solid-void solution exist?". If not, a solid-void optimization method will lose its target, and the resulting solution becomes meaningless. Huang and Xie [53] proposed a so called "soft-kill" BESO method using an artificial material interpolation scheme with penalization similar to the treatment in the SIMP model [9].

Material interpolation schemes with penalization have been widely used in the SIMP method to steer the solution to nearly solid-void designs [7, 115, 184]. Bendsøe and Sigmund [9] have compared the material interpolation schemes to various bounds for effective material properties in composite (e.g. the Hashin-Shtrikman bounds) and showed that composite materials from intermediate densities are physically realizable. More importantly, such material interpolation schemes with penalization
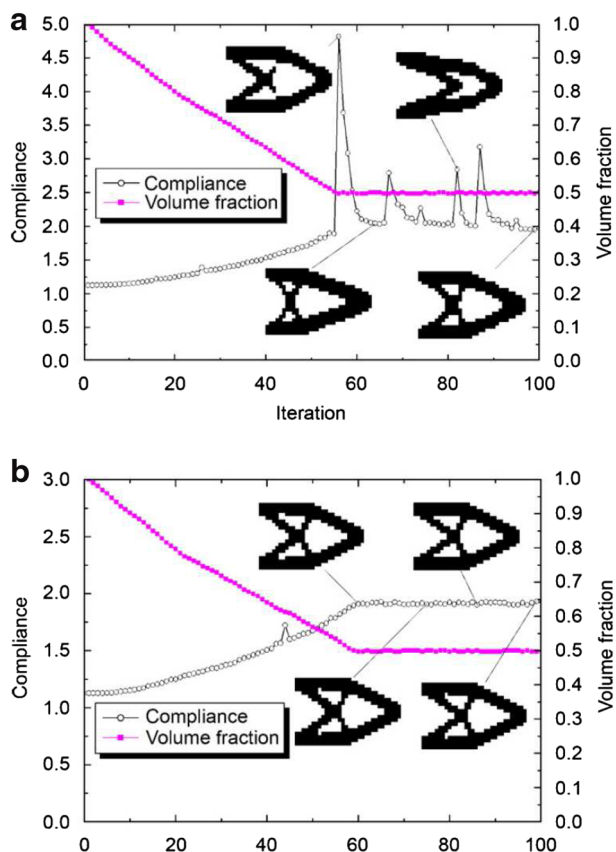
manifested that the solid-void optimal design do exist. To achieve a nearly solid-void design, Young's modulus of the intermediate material is interpolated as a function of the element density:

$$E_e = \xi_e^p E_0, \quad \xi_e = \xi_{\min} \text{ or } 1 \tag{8}$$

where E_0 denotes Young's modulus of the solid material and p the penalty exponent. The binary design variable ξ_e is attached on an element declaring the absence ($\xi_{\min}$) or presence (1) of the element. Note that $\xi_{\min}$ is an artificially defined small parameter (e.g., 0.001). It is assumed that Poisson's ratio is independent of the design variables. The global stiffness matrix $\mathbf{K}$ can thus be expressed by the element stiffness matrix $\mathbf{k}_e$ and design variables ξ_e as

$$\mathbf{K}(\boldsymbol{\xi}) = \sum_{e=1}^{N_e} \mathbf{k}_e = \sum_{e=1}^{N_e} \xi_e^p \mathbf{k}_0, \tag{9}$$

where $\mathbf{k}_0$ denotes the element stiffness matrix of solid and N_e denotes the total number of finite elements. It is assumed through out the paper that uniform mesh is used for design. Thus all element stiffness matrix of solid can be denoted by the same $\mathbf{k}_0$.

Using the adjoint method, the sensitivity of the structural compliance ($f_c = \mathbf{u}^T \mathbf{K} \mathbf{u}$) with regard to the change in the e-th element can be found as [10]

$$\frac{\partial f_c}{\partial \xi_e} = -p \xi_e^{p-1} \mathbf{u}_e^T \mathbf{k}_0 \mathbf{u}_e \tag{10}$$

where $\mathbf{u}$ and $\mathbf{u}_e$ denote the global and element displacement vectors, respectively. By the ESO/BESO methods, a structure is optimized using discrete design variables. That is to say that only two bound materials are allowed in the design. Therefore, the sensitivity number used in the ESO/BESO methods can be defined by the relative ranking of the sensitivity of an individual element as [55]

$$\alpha_e = -\frac{1}{p} \frac{\partial f_c}{\partial \xi_e} = \begin{cases} \mathbf{u}_e^T \mathbf{k}_0 \mathbf{u}_e & \text{when } \xi_e = 1 \\ \xi_{\min}^{p-1} \mathbf{u}_e \mathbf{k}_0 \mathbf{u}_e & \text{when } \xi_e = \xi_{\min}. \end{cases} \tag{11}$$

It is noted that the sensitivity numbers of solid elements are independent of the penalty exponent p and are indifferent from (4), while the sensitivity numbers of soft elements depend on the value of the penalty exponent p. The hard-kill BESO method presented in the previous sections can be viewed as a special case of the soft-kill BESO method when the penalty exponent p approaches infinity. It was also indicated that the hard-kill BESO method may not applicable for other optimization problems, e.g. frequency optimization [59].

A comparison study on the performance of the soft-kill BESO method is given in Fig. 9. Figure 9a, b show the soft-kill BESO optimal designs for $p = 1.5$ and $p = 3.0$, respectively. The results indicate that the penalty exponent
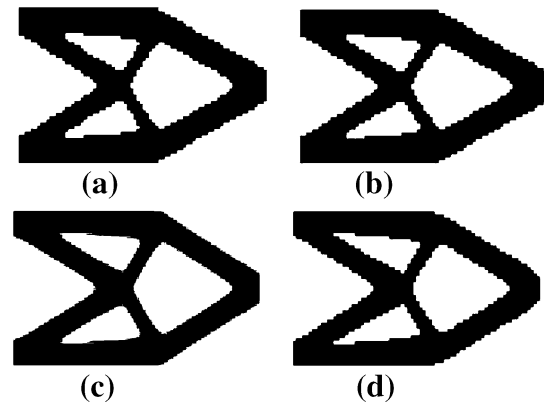

Fig. 9 Stiffness maximization designs of a cantilever: **a** soft-kill BESO with $p = 1.5$, **b** soft-kill BESO with $p = 3.0$, **c** SIMP with $p = 3.0$ and **d** the continuation method [53]

p has negligible influence on the optimal design that both optimal topologies are very close to the result of the hard-kill BESO method as shown in Fig. 8. Figure 9c shows the optimal topology using the SIMP method [10] with $p = 3.0$. Its topology is similar to soft-kill BESO designs except for "grey" elements. To avoid premature convergence to local optima, the continuation method has also bet be applied by gradually increasing the penalty exponent [118] or gradually decreasing the filter radius [124]. Figure 9d shows the final design via the continuation method and the resulted optimal topology is almost identical to Fig. 9a, b.

2.5 Standard Hard-Kill BESO Procedure

Consider a conventional structural compliance minimization problem ($f_c = \mathbf{u}^T \mathbf{K} \mathbf{u}$, i.e., stiffness maximization) subject to material volume fraction constraint as following

$$\begin{aligned} \min_{\boldsymbol{\xi}} &\quad : f_c(\boldsymbol{\xi}, \mathbf{u}) \\ \text{subject to} &\quad : \mathbf{K}\mathbf{u} = \mathbf{f} \\ &\quad : V(\boldsymbol{\xi}) = \sum \xi_e v_e = V_{\text{req}} \\ &\quad : \xi_e = 0 \quad \text{or} \quad 1, e = 1, \ldots, N_e, \end{aligned} \tag{12}$$

in which $\mathbf{K}$ and $\mathbf{u}$ are the global structural stiffness and displacement vector, v_e is the element volume, $V(\boldsymbol{\xi})$ and V_{req} are the total and required material volumes, respectively. N_e denotes the total number of finite elements. The binary design variable ξ_e is attached on an element declaring the absence (0) or presence (1) of the element.

Before elements are removed from or added to the current design, the target volume for the current design iteration $V^{(l)}$ needs to be given first. Since the required material volume V_{req} can be greater or smaller than the volume of the initial guess design, the target volume in each iteration may decrease or increase step by step until

the constraint volume is achieved. The evolution of the volume can be expressed by

$$V^{(l)} = V^{(l-1)}(1 \pm c_{\text{er}}), \tag{13}$$

in which the evolutionary ratio c_{er} determines the percentage of material to be added or removed from the design of the previous iteration. Once the target required material volume usage V_{req} is attained, the optimization algorithm alters only the topology but keeps the volume constant (up to a certain tolerance).

At each design iteration, the sensitivity numbers which denote the relative ranking of the element sensitivities are used to determine material removal and addition. When uniform meshes are used, the sensitivity number for the considered objective is defined as following using the element sensitivity as given in (4)

$$\alpha_e = \partial f_{\text{c}} / \partial \xi_e = \mathbf{u}_e^T \mathbf{k}_0 \mathbf{u}_e. \tag{14}$$

In order to avoid mesh-dependency and checkerboard patterns, sensitivity numbers are firstly smoothed by means of the filter scheme as (15)

$$\alpha_e = \frac{\sum_{j=1}^{N_e} w_{ej}\alpha_j}{\sum_{j=1}^{N_e} w_{ej}}, \tag{15}$$

where w_{ej} is a linear weight factor

$$w_{ej} = \max(0, r_{\min} - \Delta(e,j)), \tag{16}$$

determined according to the prescribed filter radius $r_{\min}$ and the element center-to-center distance $\Delta(e,j)$ between elements Ω_e and Ω_j. To improve the convergence, the filtered sensitivity numbers are further averaged with the sensitivity numbers of the previous topology iteration

$$\alpha_e^{(l)} \leftarrow (\alpha_e^{(l)} + \alpha_e^{(l-1)})/2. \tag{17}$$

The update of the topology variables by the BESO method is realized by means of two threshold parameters $\alpha_{\text{del}}^{\text{th}}$ and $\alpha_{\text{add}}^{\text{th}}$ for material removal and addition, respectively [33, 52]

$$\xi_e^{(l+1)} = \begin{cases} 0 & \text{if } \alpha_e \leq \alpha_{\text{del}}^{\text{th}} \text{ and } \xi_e^{(l)} = 1, \\ 1 & \text{if } \alpha_{\text{add}}^{\text{th}} < \alpha_e \text{ and } \xi_e^{(l)} = 0, \\ \xi_e^{(l)} & \text{otherwise.} \end{cases} \tag{18}$$

The present scheme indicates that solid elements are removed when their sensitivity numbers are less than $\alpha_{\text{del}}^{\text{th}}$ and void elements are recovered when their sensitivity numbers are greater than $\alpha_{\text{add}}^{\text{th}}$. The parameters $\alpha_{\text{del}}^{\text{th}}$ and $\alpha_{\text{add}}^{\text{th}}$ are obtained from the following iterative algorithm [48]:

1. Let $\alpha_{\text{add}}^{\text{th}} = \alpha_{\text{del}}^{\text{th}} = \alpha_{\text{th}}$, where the value α_{th} is determined iteratively such that the required material volume usage is met at the current iteration.

2. Compute the admission ratio c_{ar}, which is defined as the volume of the recovered elements divided by the total volume of the current design iteration. If $c_{\text{ar}} \leq c_{\text{ar}}^{\max}$, the maximum admission ratio, then skip the next steps; otherwise, $\alpha_{\text{del}}^{\text{th}}$ and $\alpha_{\text{add}}^{\text{th}}$ are redetermined in the next steps.

3. Determine $\alpha_{\text{add}}^{\text{th}}$ iteratively using only the sensitivity numbers of the void elements until the maximum admission ratio is met, i.e., $c_{\text{ar}} \approx c_{\text{ar}}^{\max}$.

4. Determine $\alpha_{\text{del}}^{\text{th}}$ iteratively using only the sensitivity numbers of the solid elements until the required material volume usage is met at the current iteration.

The introduction of $c_{\text{ar}}^{\max}$ stabilizes the topology optimization process by controlling the number of recovered elements. Normally, $c_{\text{ar}}^{\max}$ is set to a value greater than 1% so that it does not suppress the merit of the element recovery scheme. Note that in stiffness related designs, the above procedure can be reduced to a simpler scheme by assuming that $c_{\text{ar}} \leq c_{\text{ar}}^{\max}$ is always satisfied such that in practice only α_{th} needs to be determined.

The cycle of finite element analysis and element removal and addition continues until the target volume V_{req} is reached and the following convergence criterion defined in the variation of the objective functions is satisfied:

$$c_{\text{err}} = \frac{\left| \sum_{i=1}^{N} (f_{\text{c}}^{(l-i+1)} - f_{\text{c}}^{(l-N-i+1)}) \right|}{\sum_{i=1}^{N} f_{\text{c}}^{(l-i+1)}} \leq \delta_{\text{err}} \tag{19}$$

where l is the number of current design iteration, δ_{err} is an allowable convergence error and N is integral number which is usually selected as 5 in most design cases which means a stable compliance at least in successive 10 iterations.

3 Discussion on Zhou–Rozvany Problem

Rozvany and Zhou [183] examined the ESO/BESO methods on a specifically defined problem (see Fig. 10), known as the Zhou–Rozvany problem and a conclusion was drawn that both ESO/BESO methods are not able to always guarantee an optimal design. Huang and Xie [49]
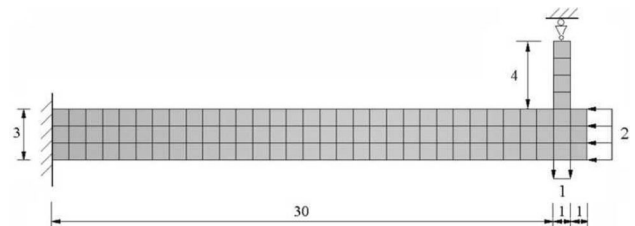

Fig. 10 Illustration of the Zhou–Rozvany problem [55]

reexamined the problem and they found that not only the ESO/BESO methods, but other well-established methods such as SIMP and level-set methods would fail as well for the Zhou–Rozvany problem. In the following a detailed discussion on the challenge Zhou–Rozvany problem is provided [183].

3.1 Zhou–Rozvany Problem [183]

The structure shown in Fig. 10 is used by Zhou and Rozvany [183] to show the breakdown of hard-kill optimization methods, such as ESO/BESO. In this example, the Young's modulus is taken as unity and the Poisson's ratio is set to zero. The mean compliance of the ground structure is about 194. If the design domain is discretized into 100 four node plane stress elements, the element in the vertical tie has the lowest strain energy density. Thus, hard-kill BESO method will remove that element from the ground structure and results in the design as shown in Fig. 11a with a mean compliance of 2186. This value is much higher than that of any intuitive design obtained by removing one element from the horizontal beam.

After removing an element in the vertical tie, the resultant structure becomes a cantilever where the vertical load is transmitted by flexural action. The region with the highest strain energy density is at the left-bottom of the cantilever. According to hard-kill ESO/BESO methods, an

Fig. 11 Designs of the Zhou–Rozvany problem: **a** hard-kill BESO design for 99% volume fraction, **b** hard-kill BESO design for 96% volume fraction, **c** a highly inefficient local optimum from SIMP method when $p \geq 3.1$ for 96% volume fraction, **d** optimal design by the continuation method for 96% volume fraction [55]

element would be added in the neighboring region rather than recovering the removed element in the vertical tie. Therefore, Zhou and Rozvany [183] concluded that hard-kill optimization methods such as ESO/BESO may produce a highly non-optimal solution. In fact, soft-kill optimization algorithms such as the level set method using continuous design variables may also produce a similar result [97]. To overcome this problem, the essence of such a solution needs to be examined first.

3.2 Is it a Non-optimal or a Local Optimal Solution?

Obviously, the answer cannot be easily found by simply comparing the objective values. Let us reconsider the above example for a volume fraction of 96%. Hard-kill optimization methods such as ESO/BESO will remove the four elements from the vertical tie as shown in Fig. 11b. This design is certainly far less efficient than an intuitive design which removes four elements from the horizontal beam.

It is known that the SIMP method with continuous design variables guarantees that its solution should be at least a local optimum. Therefore, this topology optimization problem is tested by the SIMP method starting from an initial guess design with $\xi_e = 1$ for all elements in the horizontal beam and $\xi_e = \xi_{\min} = 0.001$ for the four elements in the vertical tie. It is found that when $p \geq 3.1$ the final solution converges to the structure shown in Fig. 11c, which is exactly the same as the initial guess design. Because $\xi_{\min}$ is small, the SIMP solution in Fig. 11c can be considered to be identical to the hard-kill ESO/BESO solution in Fig. 11b. These results demonstrate that the above solutions from hard-kill ESO/BESO methods and SIMP are essentially a local optimum rather than a non-optimum. Theoretically it would be more appropriate to call such a solution *a highly inefficient local optimum* rather than a non-optimum.

The occurrence of the above 0/1 local optimal design is due to the large penalty p in the optimization algorithms. Hard-kill ESO/BESO methods have an equivalent penalty of infinity and therefore fail to obtain a better solution once they reach the highly inefficient local optimum. Similarly, the soft-kill BESO method with a finite penalty may also fail because a large penalty ($p \geq 1.5$) is normally required for topology optimization.

The exact value of the penalty p that is large enough to cause a local optimum is dependent upon the optimization problem. For the original Zhou and Rozvany [183] example given in Fig. 10, the SIMP method will produce a much more efficient solution than the one shown in Fig. 11d when $p = 3$ is used. However, if the original problem is slightly modified by reducing the vertical load from 1 to 0.5, the SIMP method with $p = 3$ will again fails in finding
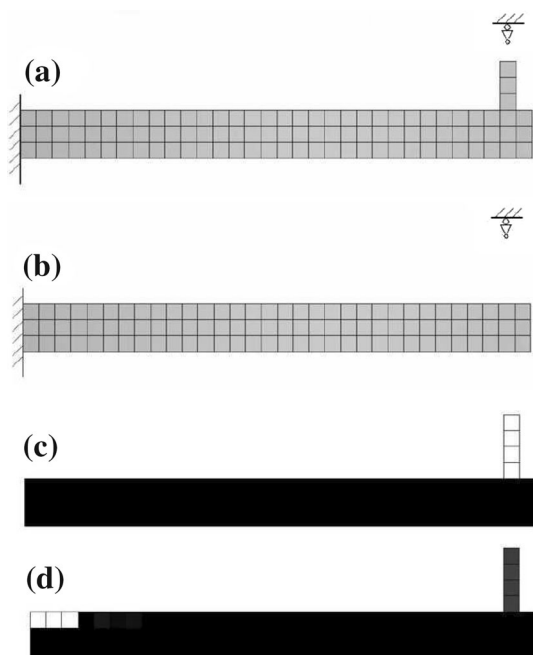
Fig. 11d but leads to the highly inefficient local optimum shown in Fig. 11c.

3.3 Avoidance of a Local Optimum Within Optimization Algorithms

It is well-known that most topology optimization problems are not convex and there exist various local optima. Meanwhile, most global optimization methods seem to be unable to handle problems of the size of a typical topology optimization problem [10]. As shown in the previous subsection, the ESO/BESO method and the SIMP method fail to ensure a global optimum and the resulting topologies are highly dependent on choices of optimization parameters and initial guesses.

Based on the experience, the local optimum can be avoided using the continuation method by gradually increasing the penalty exponent [118]. For this particular problem, the continuation method with $\Delta p = 0.1$ produces an optimal solution shown in Fig. 11d after about 700 iterations. The continuation method fails to produce a pure 0/1 global solution due to the numeric overflow although it successfully avoids the above highly inefficient local optimum. Theoretically, a global optimum cannot be guaranteed even for the continuation method as noted by Stolpe and Svanberg [133]

Therefore, it is unfair to expect the ESO/BESO methods to overcome a local optimum while other well-established methods would fail as well. To completely solve this problem, further research is required for all topology optimization methods, not just the ESO/BESO methods.

3.4 Avoidance of a Local Optimum Outside ESO/ BESO Optimization Algorithms

Nonetheless, it is necessary to find a solution outside the ESO/BESO algorithms to avoid this type of highly inefficient 0/1 local optima. Fortunately, a 0/1 highly inefficient local optimum can be easily identified even by inspection. In the above example, the cantilever is a substructure of the ground structure and its optimal solution may be a 0/1 local optimum solution of the whole structure. Therefore, 0/1 local optima widely exist in topology optimization problems for a statically indeterminate structure.

Huang and Xie [49] proposed that this inefficient local optimum can be detected by checking the boundary conditions for a statically indeterminate structure after each iteration. If a breakdown of boundary support is detected before a satisfactory solution is obtained, it may well indicate that thereafter the solution may be (but not always) a highly inefficient local optimum and the current optimization process should be stopped immediately.

Then, the problem should be re-calculated with a fine mesh to avoid breakdown of the boundary. Edwards et al. [26] and Huang and Xie [49] in their parallel but independent studies have demonstrated that an optimal design can be obtained with a refined mesh as shown in Fig. 12.

It should be noted that the mesh refinement causes the change of the original optimization problem of finding a global optimum under a given mesh as argued by Rozvany [120]. But, checking the boundary condition outside the ESO/BESO algorithms is a conservative but effective way to detect the occurrence of a highly inefficient 0/1 local optimum for this particular problem.

4 Design of Advanced Structures

The latest version of of the BESO method, i.e., the convergent and mesh-independent BESO method [48], has been applied for a wide range of structural design problems. This section summarizes various extensions and applications of the BESO method for advanced structural designs, including: stiffness optimization with multiple materials (Sect. 4.1), displacement-related structural designs (Sect. 4.2), design-dependent structural designs (Sect. 4.3), design of structural natural frequency (Sect. 4.4), design of nonlinear structures (Sect. 4.5), design of periodic structures (Sect. 4.6) and shape optimization of tunnels (Sect. 4.7).
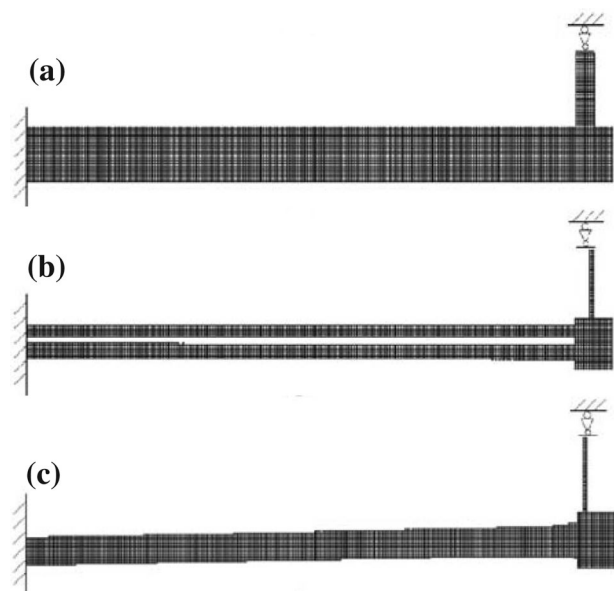

Fig. 12 Designs of the refined Zhou–Rozvany problem: **a** refined initial design (10,000 elements), **b** ESO design for 50% volume fraction, **c** BESO design for 50% volume fraction [49]

4.1 Stiffness Optimization with Multiple Materials

Huang and Xie [53] has extended the soft-kill BESO method to optimize structures composed of multiple materials with. The extension can be realized through a straightforward introduction of a multiphase material interpolation scheme following [6]. In the case of two solid materials, the material interpolation scheme can be expressed as

$$E_e = \xi_e^p E^{(1)} + (1 - \xi_e^p)E^{(2)} \tag{20}$$

where $E^{(1)}$ and $E^{(2)}$ are Young's moduli of two materials and $E^{(1)} > E^{(2)} \neq 0$. When $E^{(2)} = 0$, the above interpolation is reduced to (8) for the case of solid-void designs.

In the case of more than two solid materials, saying n types of materials with Young's moduli $E^{(1)} > E^{(2)} > \cdots > E^{(N)}$. Topology design variables need to be defined for each of the "$N - 1$" pairs of neighboring phases

$$E_e = (\xi_e^{(j)})^p E^{(j)} + (1 - (\xi_e^{(j)})^p)E^{(j+1)}, \tag{21}$$

where the design variable $\xi_e^{(j)}$ associated to the e-th element for the j-th material is defined as follows

$$\xi_e^{(j)} = \begin{cases} 1, & \text{for} \quad E_e \geq E^{(j)} \\ \xi_{\min}, & \text{for} \quad E_e \leq E^{(j+1)}. \end{cases} \tag{22}$$

The sensitivity number for compliance minimization design can be found through the sensitivity analysis with respect to the design variables $\xi_e^{(j)}$ as

$$\alpha_e^{(j)} = (\xi_e^{(j)})^{p-1}(\mathbf{u}_e^T \mathbf{k}_e^{(j)} \mathbf{u}_e - \mathbf{u}_e^T \mathbf{k}_e^{(j+1)} \mathbf{u}_e) \tag{23}$$

where $\mathbf{k}_e^{(j)}$ and $\mathbf{k}_e^{(j+1)}$ denote the element stiffness matrices calculated from using $E^{(j)}$ and $E^{(j+1)}$, respectively. It should be noted that the sensitivity number $\alpha_e^{(j)}$ is defined in the whole design domain even though it is only used for making adjustments between materials "j" and "$j + 1$".

It is noted that there exit "$N - 1$" groups of sensitivity numbers in the system to adjust the corresponding neighboring materials. The BESO procedure for multiple material designs is similar to that for solid-void designs except that the sensitivity calculation and material adjustment must be carried out for each of the "$N - 1$" groups. The BESO design starts from the full design with material 1 and triggers by evolutionary ratio which is defined as the proportion of volume reduction of material 1 relative to the total volume of material 1 in the current design. At the same time, the volume of material 2 gradually increases until the objective volume is achieved. Thereafter, the volume of material 2 keeps constant and the volume of material 3 gradually increases until the objective volume is achieved, and so on. Transition between materials 1 and 2

is carried out according to the target volume of material 1 and sensitivity numbers $\alpha_e^{(1)}$. Similarly, transition between materials 2 and 3 is carried out according to the target volume of material 2 and sensitivity numbers $\alpha_e^{(2)}$, and so on. The whole optimization procedure is stopped when objective volumes for all materials are achieved and the convergent criterion is satisfied. Figure 13 shows an optimal design example of a half-beam structure which is made of three material phases: void and two solids of different elastic moduli.

The multiphase BESO algorithm has also been applied for the design of material microstructures in both 2D and 3D cases [112], which will be detailed in Sect. 5.2. Some further improvements to the multi-material BESO algorithm have been provided recently by Ghabraie [37] with the proposition of a new filter scheme and a gradual procedure inspired by the continuation method.

4.2 Displacement-Related Structural Designs

In most cases the objective of topology optimization is to reduce the weight of structure where the constraint is imposed on the compliance or the displacement. It is of significant importance in practice to restrain the maximum deflection of the structure below a certain critical value. During the early developments, volume constraint was more preferable because of the concept of progressive removal of inefficient material. Rozvany [120] has doubted the extensibility of the ESO-type methods to displacement related designs. The first extension of the BESO method to include displacement constraint was provide by Huang and Xie [55]. In this work, the topology optimization problem was defined to minimize the material volume with a displacement constraint as
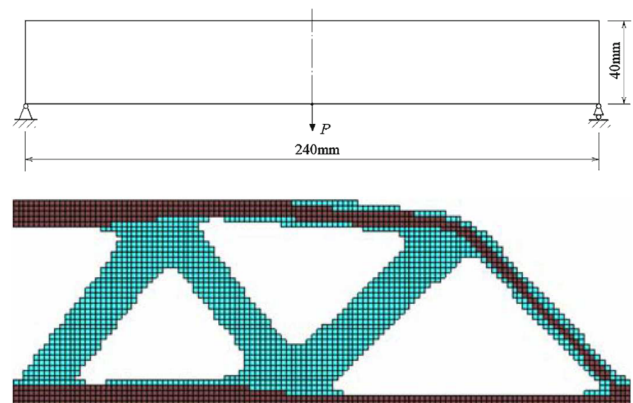

Fig. 13 BESO optimal design of a three-phase structure [53]

$$\min_{\xi} : \quad V(\xi)$$
$$\text{subject to} : \quad \mathbf{Ku} = \mathbf{f}$$
$$: \quad u_j \leq u_j^*$$
$$: \quad \xi_e = \xi_{\min} \quad \text{or} \quad 1, e = 1, \ldots, N_e, \tag{24}$$

where u_j and u_j^* are the displacement of the j-th degree of freedom and the prescribed allowable displacement value, respectively. Note that, to a certain extent the above optimization problem is equivalent to that in the conventional setting where the compliance is minimized subject to a given structural volume [18, 55].

In order to solve this problem using the BESO method, the displacement constraint was proposed to be added to the objective function with an introduction a Lagrange multiplier λ as

$$f_{\text{obj}}(\xi) = V(\xi) + \lambda(u_j - u_j^*). \tag{25}$$

It can be seen that when the displacement constraint is satisfied, the above augmented objective is equivalent to the original one and is independent on the value of the Lagrange multiplier. With the SIMP material interpolation model of (8), the derivative of the augmented objective equals

$$\frac{\partial f_{\text{obj}}}{\partial \xi_e} = v_e - \lambda p \xi_e^{p-1} \mathbf{u}_{ej}^T \mathbf{k}_0 \mathbf{u}_e, \tag{26}$$

where v_e is the element volume and the sensitivity of the displacement of the j-th degree of freedom is calculated using the adjoint method [10]. $\mathbf{u}_{ej}$ is the virtual displacement vector of the e-th element resulted from a dummy load whose j-th degree of freedom is set to unity and the remains are set to zero. When a uniform mesh is used (i.e., element volumes are the same), the relative ranking of sensitivity of each element can be defined by the following sensitivity number

$$\alpha_e = -\frac{1}{\lambda p}\left(\frac{\partial f_{\text{obj}}}{\partial \xi_e} - v_e\right) = \xi_e^{p-1}\mathbf{u}_{ej}^T\mathbf{k}_0\mathbf{u}_e. \tag{27}$$

Following the basic BESO procedure using the above sensitivity numbers, Fig. 14 shows the volume minimization design result of the the half beam structure shown in Fig. 13 subject to a displacement constraint of 0.2 mm on the loading point. The material volume of the structure is reduced to 45% of the initial full design and the resulting maximum deflection is 0.1997 mm which is very close to the prescribed constraint limit.

An extension to this work was proposed by Zuo and Xie [189] for a global control of displacements. In this extended work, the displacement constraint in (24) is substituted by a global constant

$$\max\{u\} \leq u^*, \quad \text{for} \quad \mathbf{u} \in \Omega_{\text{disp}} \tag{28}$$
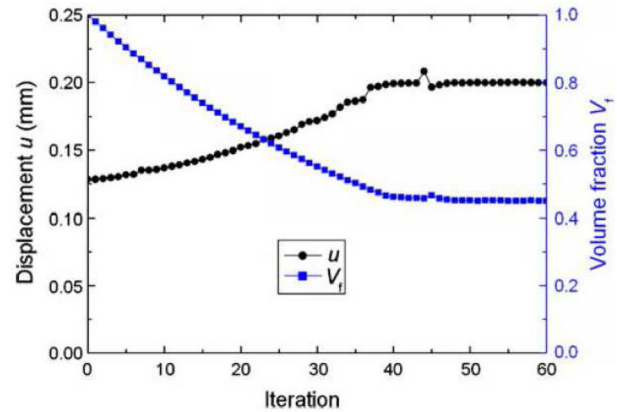

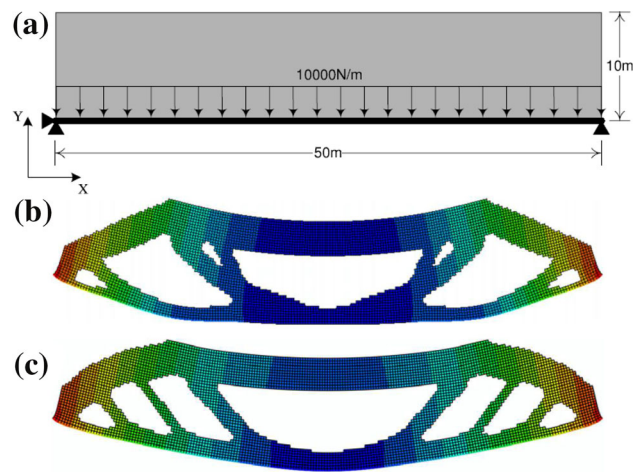Fig. 14 BESO optimal design for minimizing the structural volume against the maximum deflection [55]

Fig. 15 BESO optimal design of a simply-supported bridge: a design domain, b stiffness design with global displacement constraint of $u^* = 6.5 \times 10^{-5}$ m in Y-direction ($V = 57.8\%, u_{\max} = 6.495 \times 10^{-5}$ m), c conventional stiffness design ($V = 57.8\%, u_{\max} = 7.291 \times 10^{-5}$ m) [189]

to constraint the maximum displacement within a selected domain Ω_{disp} below the allowable critical displacement u^*. The locations and directions of maximum nodal displacements are dynamically detected, the numerical instabilities of which are adaptively dealt with by several robust stabilization strategies. Fig. 15a is an example that deals with a simply-supported bridge with a uniform distributed load on a non-designable deck layer at the bottom. The volume

is to be minimized with the deck deflection in the vertical direction (Y-direction) within a limit of 6.50×10^{-5} m. The final topology in the deformed view is shown in Fig. 15b, where the final maximum vertical deflection is 6.495×10^{-5} m which satisfies the constraint of 6.50×10^{-5} m. Stiffness optimization for this simply-supported bridge is carried out as a comparison. The final optimal topology in the deformed view is shown in Fig. 15c. The stiffness design is produced by conventional stiffness optimization under a volume constraint. With the same volume fraction (57.8%), the maximum vertical deflection of the stiffness design (7.291×10^{-5} m) is 12.3% higher than that of the deflection design. Comparing the two deformed optimal designs, it is found that the deformation of the middle part of the deck in the deflection design is flat which reduces the maximum vertical deflection and outperforms the stiffness design in this regard.

Another type of displacement related design can be formulated as the minimization of the structural compliance with constraints on both volume fraction and a certain displacement [54]. For example, a local displacement constraint may be imposed on the horizontal movement of the roller support shown in Fig. 16. Such kind of constraint arises when the displacement at a specific location, not necessarily the loading point, is required to be within a prescribed limit.

$$\min_{\xi} : \quad f_c(\xi, \mathbf{u})$$
$$\text{subject to} : \quad \mathbf{Ku} = \mathbf{f}$$
$$: \quad u_j \leq u_j^*$$
$$: \quad V(\xi) = \sum \xi_e v_e = V_{\text{req}}$$
$$: \quad \xi_e = \xi_{\min} \quad \text{or} \quad 1, e = 1, \ldots, N_e. \tag{29}$$

Similar to the previous treatment, the objective function is augmented with an introduction a Lagrange multiplier λ as

$$f_{\text{obj}}(\xi) = f_c(\xi, \mathbf{u}) + \lambda(u_j - u_j^*), \tag{30}$$
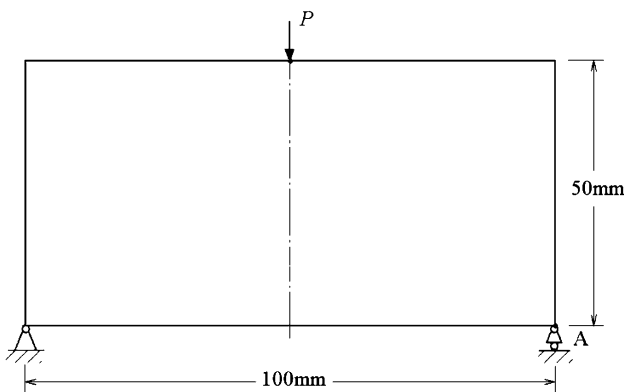
and the corresponding sensitivity numbers are [54]

$$\alpha_e = -\frac{1}{p} \frac{\partial f_{\text{obj}}}{\partial \xi_e} = \xi_e^{p-1} \left(\mathbf{u}_e^T \mathbf{k}_0 \mathbf{u}_e - \lambda \mathbf{u}_{ej}^T \mathbf{k}_0 \mathbf{u}_e \right). \tag{31}$$

Figure 16 is a stiffness topology optimization problem for a beam structure which is supported by both ends and vertically loaded ($P = 100$ N) in the middle of its upper edge as depicted. The material is assumed with the Young's modulus $E = 1$ GPa, the Poisson's ratio $= 0.3$. The volume constraint is 30% of the design domain. The optimal topology without any displacement constraint is shown in Fig. 17a for comparison. Its mean compliance is 191 Nmm and the horizontal movement of the roller support A is 1.43 mm. When the movement of the roller support is constrained to be 1.4, 1.2 or 1.0 mm, the resulting topologies are shown in Fig. 17b–d. Their according mean compliances are 191, 195 and 203 Nmm. It can be seen that there is an increase of mean compliance when a strict displacement constraint is applied.

It can be seen that the above optimization problem (29) has multiple constraints. It is certainly possible to consider other optimization problems with a local displacement constraint in a similar manner, e.g. minimizing the structural volume against two displacement constraints in which one displacement is directly related to the overall structural performance.

By a switchmen of the compliance objective and the displacement constraint in (29), the optimization model is reformulated for the design of a compliant mechanism in (32), which is usually a monolithic structure that transfers an input force or displacement to another point through elastic deformation (see Fig. 18).

$$\max_{\xi} : \quad u_{\text{out}}$$
$$\text{subject to} : \quad \mathbf{Ku} = \mathbf{f}$$
$$: \quad f_c(\mathbf{u}, \xi) \leq f_c^*$$
$$: \quad V(\xi) = \sum \xi_e v_e = V_{\text{req}}$$
$$: \quad \xi_e = \xi_{\min} \quad \text{or} \quad 1, e = 1, \ldots, N_e. \tag{32}$$

In order to realize such design by using the BESO method, Huang et al. [63] proposed to gradually vary the

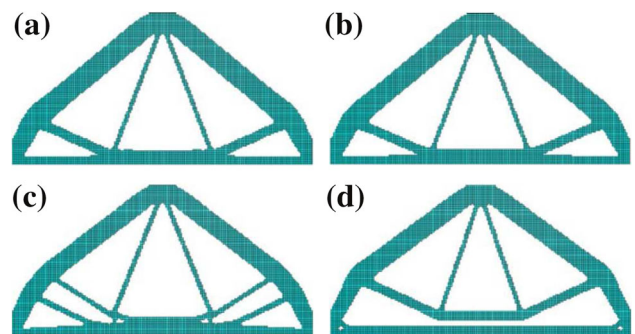Fig. 16 A beam structure supported by both ends [54]

Fig. 17 BESO optimal designs: **a** without a local displacement constraint; **b** $u_A^* = 1.4$ mm; **c** $u_A^* = 1.2$ mm; **d** $u_A^* = 1.0$ mm [54]
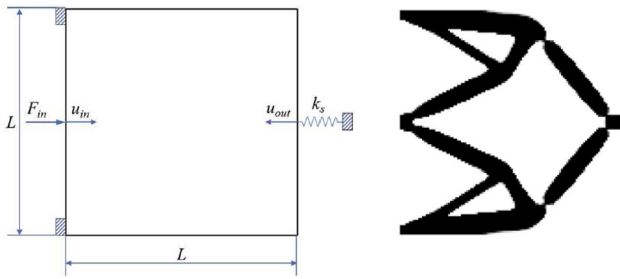
Fig. 18 Illustration of a BESO design of compliant inverter [63]

design variables according to the evaluated sensitivity numbers such that

$$\xi_e = \begin{cases} \min(\xi_e + \Delta\xi, 1) & \text{if} \quad \alpha_e \geq \alpha_{th} \\ \max(\xi_e - \Delta\xi, \xi_{min}) & \text{if} \quad \alpha_e < \alpha_{th}, \end{cases} \quad (33)$$

where $\Delta\xi$ is a user defined move limit.

4.3 Design-Dependent Structural Designs

Topology optimization of continuum structures with self-weight loads has been studied by Yang et al. [177] and Ansola et al. [4] using the modified ESO procedures (early versions of BESO). Huang and Xie [57] revisited later the same problem by using the soft/hard-kill BESO methods. The basic formulation of the topology optimization problem may also consist of minimizing the compliance of the structure with self-weight load subject to a constraint on the structural volume as given in (12)

$$\begin{aligned} \min_{\xi} : \quad & f_c(\boldsymbol{\xi}, \mathbf{u}) \\ \text{subject to} : \quad & \mathbf{Ku} = \mathbf{f} \\ : \quad & V(\boldsymbol{\xi}) = \sum \xi_e v_e = V_{req} \\ : \quad & \xi_e = \xi_{min} \quad \text{or} \quad 1, e = 1, \ldots, N_e. \end{aligned} \quad (34)$$

Different from the topology optimization problem for fixed external forces, here the applied force, $\mathbf{f}$, includes the design-dependent gravity load.

Yang et al. [177] showed that for compliance optimization of structures with design dependent loads, the ESO procedure can be carried out using a modified sensitivity number:

$$\alpha_e = \left(\mathbf{u}_e^T \mathbf{k}_e \mathbf{u}_e + 2\Delta\mathbf{f}_e^T \mathbf{u}_e\right)/v_e \quad (35)$$

where $\Delta\mathbf{f}_e$ is the change in the load vector due to the removal of the e-th element and v_e is the element volume.

As for BESO designs of the problem, Huang and Xie [57] have derived the sensitivity numbers from a strict sensitivity analysis with the adoption of the RAMP material interpolation model [132]. By the RAMP model, the density and the Young's modulus are defined in terms of the topology design variables as

$$\begin{cases} \rho_e = \xi_e \rho_0 \\ E_e = \dfrac{\xi_e}{1 - q(1 - \xi_e)} E_0, \end{cases} \quad (36)$$

where ρ_0 and E_0 are the density and Young's modulus of the solid material, q is a penalty factor which is larger than 0 for topology optimization problems. They have shown that when hard-kill BESO method is adopted, i.e., parameter q in RAMP takes infinity, the corresponding sensitivity numbers for structures with self-weight loads are the same as that for structures with fixed external forces:

$$\alpha_e = \begin{cases} \mathbf{u}_e^T \mathbf{k}_0 \mathbf{u}_e & \text{when} \quad \xi_e = 1 \\ 0 & \text{when} \quad \xi_e = \xi_{min}. \end{cases} \quad (37)$$

Figure 19 shows a simply supported rectangular plate of 1 m × 0.5 m and the corresponding hard-kill BESO design result. The objective of the problem is to find the optimal topology of the structure withstanding its self-weight. The amount of available material was restricted to 15% of the design domain. The hard-kill BESO design process yields an arch structure which spans the both end supports to optimally withstand its self-weight.

Recently, Picelli et al. [100] have extended the hard-kill BESO method for the design of structures subjected to fluid pressure. Their proposition is based on the substitution of void elements by incompressible fluid ones capable of transferring pressure through the fluid region. The pressure loading is automatically obtained by the use of coupling matrices integrated over the fluid-structure interfaces. Because of the discrete nature of the hard-kill BESO
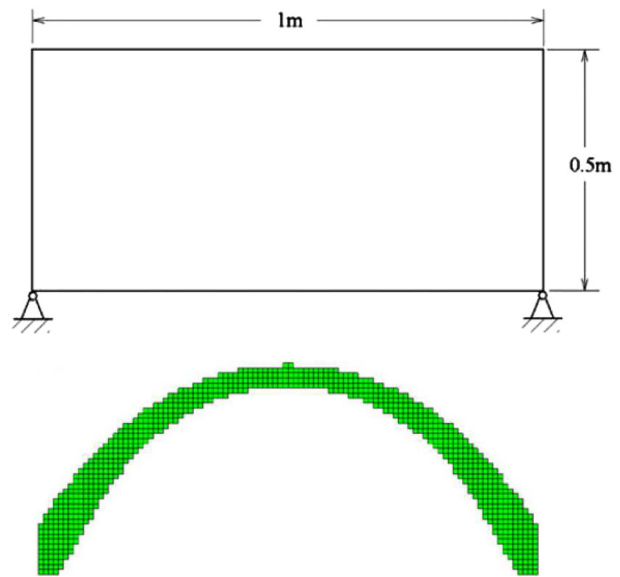

Fig. 19 Design domain of a simply supported *rectangular plate* subject to self-weight loading and the corresponding hard-kill BESO design result [57]

method, no intermediate density elements are allowed during the optimization and the problem is solved without any need for pressure load surface parametrization schemes. Figure 20 shows the right half of a unitary thickness two-dimensional piston head model and the corresponding hard-kill BESO design result where the volume fraction constraint is 30%. Due to combustion explosion, the structure suffers a fluid pressure loading in its top edge. They have shown that the BESO method provides a simple yet effective design tool for the designs involving pressure loads.

Based on the above-mentioned work, Picelli et al. [102] have further extended the hard-kill BESO method for the design of completely submerged buoyant modules with design-dependent fluid pressure loading. The submerged buoyant module is used to support offshore rig installation and pipeline transportation at all water depths. The objective of such design is to identify the buoy design that has the highest stiffness, allowing it to withstand deepwater pressure whilst uses the least material and possesses a minimum prescribed buoyancy. Figure 21 shows a subsea buoy design problem and the corresponding hard-kill BESO design result with the 30% volume fraction. Only half of the buoy is considered for design with an inner and outer radius, and the pipeline is attached to the buoy's inner edge. A inequality constraint is considered in the design to
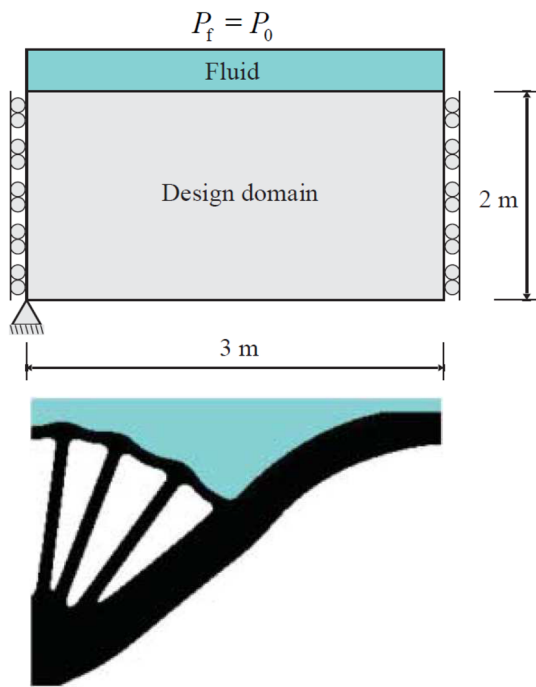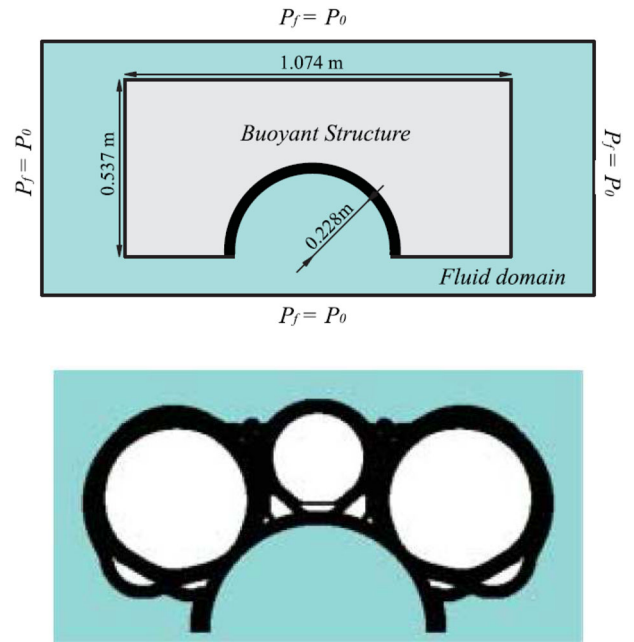

Fig. 21 A fluid-structure design problem and the corresponding hard-kill BESO design result [102]

guarantee minimum required buoyancy effects. The final topology design result in Fig. 21 is a bubble-like structure.

4.4 Design of Structural Natural Frequency

Frequency optimization is of great importance in many engineering fields, e.g., aerospace and automotive industries. Compared with the extensive research on stiffness optimization, there has been much less work concerned with topology optimization for natural frequency. By the finite element method, the dynamic behavior of a structure can be represented by the following general eigenvalue problem

$$(\mathbf{K} - \omega_j^2 \mathbf{M})\mathbf{u}^{(j)} = \mathbf{0} \tag{38}$$

where $\mathbf{K}$ is the global stiffness matrix, $\mathbf{M}$ is the global mass matrix, ω_j is the j-th natural frequency and $\mathbf{u}^{(j)}$ is the eigenvector related to the j-th natural frequency. The topology optimization model for the maximization of natural frequencies are conventionally defined as

$$
\begin{aligned}
\max_{\boldsymbol{\xi}} : \quad & \omega_j \\
\text{subject to} : \quad & (\mathbf{K} - \omega_j^2 \mathbf{M})\mathbf{u}^{(j)} = \mathbf{0} \\
: \quad & V(\boldsymbol{\xi}) = \sum \xi_e v_e = V_{\text{req}} \\
: \quad & \xi_e = \xi_{\min} \quad \text{or} \quad 1, \ e = 1, \ldots, N_e.
\end{aligned} \tag{39}
$$

Early contributions on the natural frequency design were conducted by Xie and Steven [163] and Yang et al. [175] by using the hard-kill ESO method and an early version of

Fig. 20 Design domain of a piston head structure under pressure loading and the corresponding hard-kill BESO design result [100]

BESO method, respectively. In the early works, the sensitivity number is defined as

$$\alpha_e^{(j)} = \frac{1}{m^{(j)}}(\mathbf{u}_e^{(j)})^T(\omega_j^2\mathbf{m}_e - \mathbf{k}_e)\mathbf{u}_e^{(j)} \qquad (40)$$

where $m^{(j)}$ is the modal mass corresponding to the j-th natural frequency. This sensitivity number definition gives the change of ω_j due to the removal of the j-th element.

It has been shown that soft-kill BESO method with the adoption of SIMP type material interpolation model is not suitable for frequency optimization. This is mainly due to artificial localized modes in low density regions [24, 98]. In order to adapt soft-kill BESO method for structural natural frequency designs, Huang et al. [59] developed a new material interpolation scheme for both density and Young's modulus:

$$\begin{cases} \rho_e = \xi_e\rho_0 \\ E_e = \left(\frac{\xi_{\min} - \xi_{\min}^p}{1 - \xi_{\min}^p}(1 - \xi_e^p) + \xi_e^p\right)E_0. \end{cases} \qquad (41)$$

The corresponding sensitivity numbers are derived from the sensitivities of the design variables. When $\xi_{\min}$ tends to zero and $p > 1$, the sensitivity numbers can be expressed as [59]

$$\alpha_e^{(j)} = \begin{cases} \dfrac{1}{\omega_j}(\mathbf{u}_e^{(j)})^T\left(\mathbf{k}_0 - \dfrac{\omega_j^2}{p}\mathbf{m}_0\right)\mathbf{u}_e^{(j)}, & \xi_e = 1 \\ -\dfrac{\omega_j}{2p}(\mathbf{u}_e^{(j)})^T\mathbf{m}_0\mathbf{u}_e^{(j)}, & \xi_e = \xi_{\min} \end{cases} \qquad (42)$$

in which $\mathbf{k}_0$ and $\mathbf{m}_0$ are the stiffness and mass matrices of solid elements when uniform mesh is used. Note the sensitivity numbers for soft elements do not approach to zero. This is why the hard-kill BESO method misleads the search direction and needs the artificial corrections [190].

Figure 22a shows a first natural frequency maximization design problem. The beam structure is simply supported at the two ends. The prescribed material volume fraction is 50%. The material is assumed with the Young's modulus $E = 10$ MPa, the Poisson's ratio $v = 0.3$, and mass density $\rho = 1$ kg/m^3. The optimal design result is given in Fig. 22b and the first two eigenmodes of the optimal design are given in Fig. 22c, d.

The soft-kill BESO method for frequency designs developed by Huang and Xie [59] has been extended for the frequency designs of fluid-structure [138] and acoustic-structure [101] interaction systems. The interaction between two phases follows their early development [100]. Another extension has been recently given by Munk et al. [92] for structural optimization with dynamic and buckling objectives.
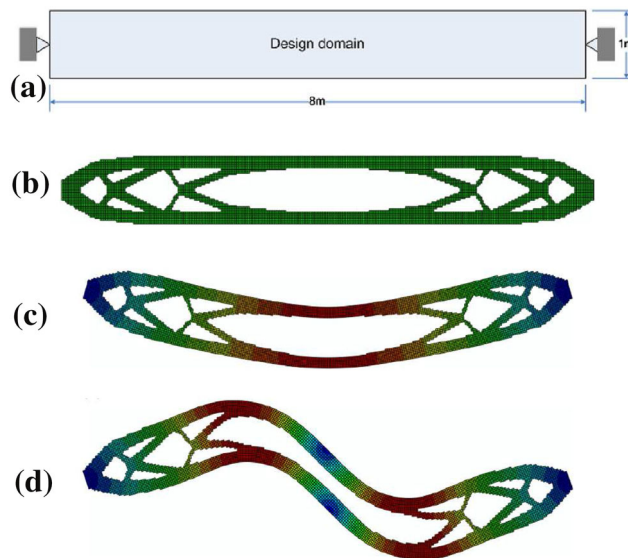

Fig. 22 Soft-kill BESO design of a simply supported beam: **a** problem illustration, **b** maximization design of the first natural frequency, **c** the first eigenmode of the optimal design, **d** the second eigenmode of the optimal design[59]

4.5 Design of Nonlinear Structures

Most of early works on topology optimization were restricted to linear structural designs. In pursuing more realistic designs, continuous efforts have been conducted to extend topology optimization to nonlinear structural designs considering various sources of nonlinearity. With regard to nonlinear structural designs, displacement-controlled loading is most widely considered due to stability considerations (e.g., [19, 52, 58, 86, 121, 179]). Within the nonlinear framework, structural stiffness maximization is equivalent to the maximization of the mechanical work expended in the course of the deformation process. In practice, the total mechanical work f_w, is approximated by numerical integration using the trapezoidal rule, i.e.

$$f_w \approx \frac{1}{2}\sum_{i=1}^{n_{\text{load}}}\left(\mathbf{f}_{\text{ext}}^{(i)} + \mathbf{f}_{\text{ext}}^{(i-1)}\right)^T\Delta\mathbf{u}^{(i)}. \qquad (43)$$

Here n_{load} is the total number of displacement increments, $\Delta\mathbf{u}^{(i)}$ is the i-th increment of the nodal displacement vector and $\mathbf{f}_{\text{ext}}^{(i)}$ is the external nodal force vector (comprising surface tractions, reaction forces and volume forces) at the i-th load increment.

During the optimization the material volume fraction is prescribed. Then the optimization problem discretized with N_e elements can be formulated as (e.g., [33, 52])

$$\begin{aligned}
\max_{\xi} : \quad & f_{\mathrm{w}}(\boldsymbol{\xi}, \mathbf{u}) \\
\text{subject to} : \quad & \mathbf{r}(\boldsymbol{\xi}, \mathbf{u}) = \mathbf{0} \\
: \quad & V(\boldsymbol{\xi}) = \sum \xi_e v_e = V_{\mathrm{req}} \\
: \quad & \xi_e = \xi_{\min} \text{ or } 1, \mathrm{e} = 1, \ldots, \mathrm{N_e}.
\end{aligned} \quad (44)$$

Here v_e is the volume of element e and the vector $\mathbf{r}$ denotes the residual

$$\mathbf{r}(\boldsymbol{\xi}, \mathbf{u}) = \mathbf{f}_{\mathrm{ext}} - \sum_{e=1}^{N_e} \xi_e \int_{\Omega_e} \mathbf{B}^T \boldsymbol{\sigma} \mathrm{d}\Omega_e. \quad (45)$$

Recall attention that by this model the hard-kill BESO model is adopted that discrete design variable $\xi_e = \xi_{\min}/1$ indicates the existence of the associated solid element e, whereas the constitutive behavior is assumed independent on ξ_e.

The prior extension of the hard-kill BESO method to the above nonlinear design problems were conducted by Huang and Xie [47, 52, 58]. In their work, the sensitivity numbers are simply defined as

$$\alpha_e = \sum_{i=1}^{n_{\mathrm{load}}} (w_e^{(i)} - w_e^{(i-1)}) = w_e^{(n)} \quad (46)$$

where $w_e^{(i)}$ is the element strain energy at the i-th load increment. The given sensitivity number means that the decrease of the total external work due to removing one element is equal to the total strain energy of the element in its final deformed state and irrelevant to the size of displacement intervals. It has been shown that with this sensitivity number definition, one may successfully conduct designs involving both material and geometrical nonlinearities.

Figure 23a shows a simply supported beam. It is assumed that the available material can only cover 30% volume of the design domain. Both material and geometrical nonlinearities are considered. The material is assumed with the Young's modulus $E = 200$ GPa, the Poisson's ratio $v = 0.3$, yield stress $\sigma_{\mathrm{y}} = 300$ MPa and plastic hardening modulus $E_{\mathrm{h}} = 0.3E$. BESO design starts from the initial guess design with 30% material of the design domain as shown in Fig. 23a to save computation time. BESO designs are carried out for three different displacement loads (20, 50, 100 mm) applied at the center of bottom edge and the design results are given in Fig. 23b–d. It can be observed that the design result is dependent on the degree of the displacement load.

Recently, Xia et al. [151] proposed anther sensitivity number definition for the nonlinear design case following a rigorous sensitivity analysis. By the adjoint method, the sensitivity of the objective with respect to design variables equals
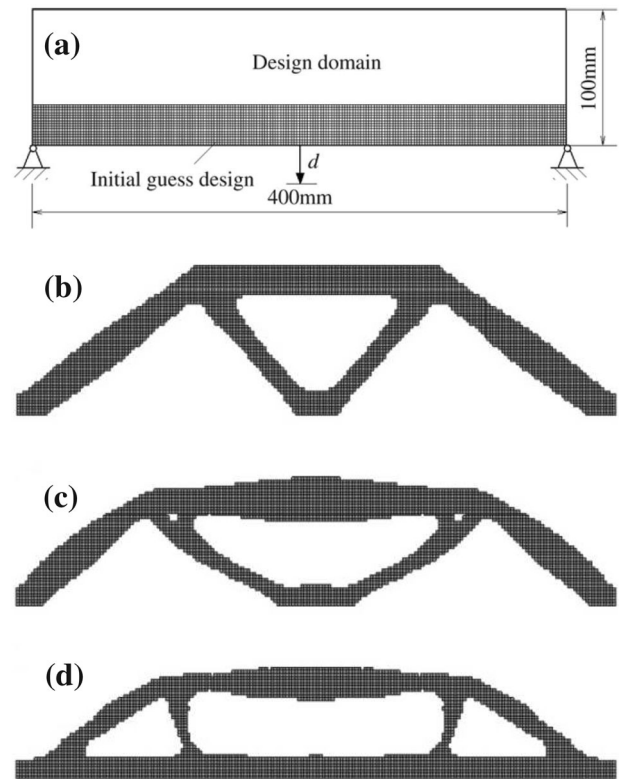

Fig. 23 BESO nonlinear designs: a design domain, initial guess design and support conditions, b design result for $d = 20$ mm, c design result for $d = 50$ mm, d design result for $d = 100$ mm [52]

$$\begin{aligned}
\frac{\partial f_{\mathrm{w}}}{\partial \xi_e} = -\frac{1}{2} \sum_{i=1}^{n_{\mathrm{load}}} \Bigg\{ & \left(\boldsymbol{\lambda}^{(i)} \right)^T \int_{\Omega_e} \mathbf{B}^T \boldsymbol{\sigma}^{(i)} \mathrm{d}\Omega_e \\
& + \left(\boldsymbol{\mu}^{(i)} \right)^T \int_{\Omega_e} \mathbf{B}^T \boldsymbol{\sigma}^{(i-1)} \mathrm{d}\Omega_e \Bigg\}
\end{aligned} \quad (47)$$

in which $\boldsymbol{\lambda}^{(i)}$ and $\boldsymbol{\mu}^{(i)}$ are the solutions of the corresponding adjoint systems (see [151] for details).

With (47) at hand, the sensitivity numbers are defined as

$$\alpha_e = \begin{cases} \left(\dfrac{\partial f_{\mathrm{w}}}{\partial \xi_e} \right)^{\beta} & \text{when } \xi_{\mathrm{e}} = 1 \\ 0 & \text{when } \xi_{\mathrm{e}} = \xi_{\min} \end{cases} \quad (48)$$

in which β is a numerical damping coefficient similar to the one applied in the Optimality Criteria method for density-based methods [10, 126]. In the presence of dissipative effects, the sensitivity numbers vary by several orders of magnitude resulting in instabilities of the topology evolution process, especially when removing certain structural branches (see e.g., [33]). For this reason, the damping scheme constraining the variance of the sensitivity numbers is introduced to stabilize the topological evolution process in particular for dissipative structural designs. In addition, another stabilization scheme was developed in

[151] by progressively reducing the sensitivity filtering radius. By setting initially a large filter radius value and reducing it gradually, the emergence of the redundant structural branches, which are to be eliminated afterwards and are the main reasons deteriorating the design process, could be avoided.

Figure 24 shows a cantilever benchmark design problem. The left end of the cantilever is clamped, and a portion of the right-end edge (20%) is prescribed with displacement loading. The volume fraction of the solid material to be preserved is set to 60%. An elastoplastic material is assumed with the elastic Young's modulus $E = 75$ GPa and the Poisson's ratio $v = 0.3$. The dissipative material behavior is described by the von Mises yield criterion with linear isotropic hardening. Hardening modulus $E_h = 1000$ MPa and yield stress $\sigma_y = 100$ MPa are used. The numerical damping coefficient is set to $\beta = 0.5$ and the filter radius is gradually reduced from the initial $r_{min} = 20l_e$ to $r_{min} = 4l_e$, where l_e is the element length.

Two plastic design results corresponding to two different displacement loads (5 and 20 mm) and their performances subject to the same 20 mm load are presented Fig. 24. For simplicity, we refer to the left design as an approximately linear design result and the right design as fully nonlinear design result. The objective value of the linear design subjected to the higher loading is 207.54 J, while the nonlinear design attains 221.23 J. By the comparison of force-displacement curves in Fig. 24, it is shown that since the mechanical response of the structure is mostly linear for the first half of the loading, the linear design slightly outperforms the nonlinear design up to 7.5 mm tip deflection which can be seen from the force displacement curve. However, as can be observed, the nonlinear design much outperforms the linear design afterwards for higher tip deflections. We can also observe that high plastic strains are concentrated at the clamped end of the linear design, while the frontal region is barely plastic at all. In comparison to the linear design, material is moved from the frontal region to the clamped end, making the plastic strains are more evenly diffused in the whole structure and resulting in advantageous nonlinear performance.

4.6 Design of Periodic Structures

Periodic structures such as the honeycomb core of a sandwich plate are widely used in structural designs due to their lightweight and ease of fabrication [140]. A lightweight cellular material usually possesses periodic microstructures. For the design of periodic structures, the macroscopic distribution of the designable material must be periodic even though the stress/strain distribution may not exhibit any periodic characteristics. Huang and Xie [51] have extend the BESO method for the design of general macroscopic structures with additional constraints on the periodicity of the geometry of substructures.

The objective of such design is to find an optimal periodic structure in terms of stiffness with a given amount of material. A two dimensional case is shown in Fig. 25 to demonstrate a periodic structure. The design domain is divided into $N_m = m_1 \times m_2$ repeatable unit cells, where m_1 and m_2 denote the number of cells along directions x and y respectively. It is noted that the special case of $N_m = 1 \times 1$ corresponds to the conventional topology optimization problem. The structural stiffness maximization
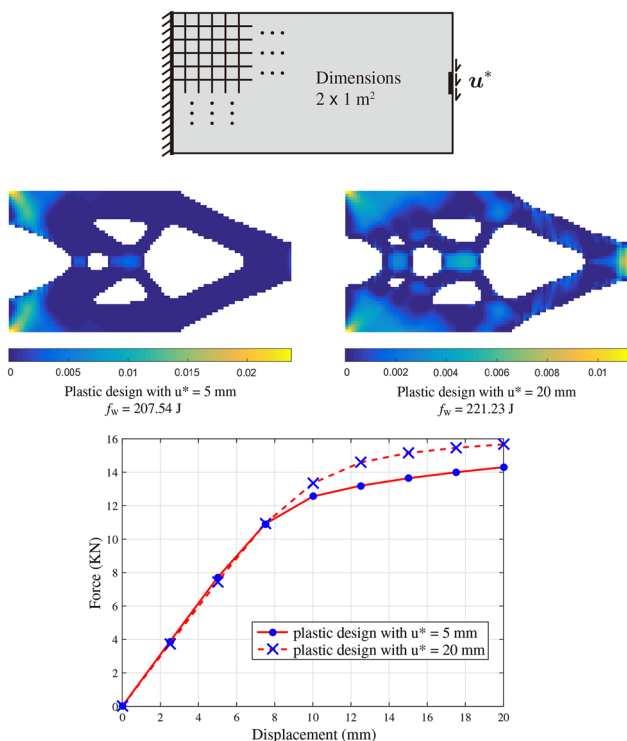

Fig. 24 BESO designs of an elastoplastic cantilever and a comparison of the force-displacement curves [151]
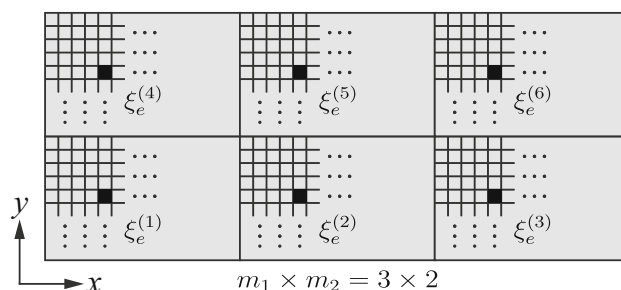

Fig. 25 A 2D design domain with $m_1 \times m_2 = 6$ repeatable cells where m_1 and m_2 denote the number of unit cells along the x and y directions; $\xi_e^{(k)}$ is the design variable associated to the e-th element of the k-th cell [51]

problem can now be formulated using the design variables $\xi_e^{(k)}$, where k and e denote the cell number and the element number in the cell, respectively (see Fig. 25), as

$$
\begin{aligned}
\min_{\{\xi^{(1)},\cdots,\xi^{(N_m)}\}} &: \quad f_c(\boldsymbol{\xi},\mathbf{u}) \\
\text{subject to} &: \quad \mathbf{Ku}=\mathbf{f} \\
&: \quad V=N_m\sum\xi_e^{(k)}v_e^{(k)}=V_{\text{req}} \\
&: \quad \xi_e^{(1)}=\cdots=\xi_e^{(N_m)}, \ e=1\ldots,N_e^{(k)}, \\
&: \quad \xi_e^{(k)}=\xi_{\min} \quad \text{or} \quad 1, k=1,\ldots,N_m.
\end{aligned}
\tag{49}
$$

where $v_e^{(k)}$ is the volume of the e-th element in the k-th unit cell and N_e is the number of elements of one unit cell. In the above equation, the condition $\xi_e^{(1)}=\cdots=\xi_e^{(N_m)}$ ensures that the status ($\xi_{\min}$ or 1) of elements at the corresponding locations in all unit cells are the same that the e-th elements in all cells are removed or added simultaneously. Therefore, the optimization process can be conducted in a representative unit cell, which can be selected from any unit cell by the user. The element sensitivity number for hard-kill BESO method is defined as the variation of the overall compliance due to the combined change of the e-th elements in all unit cells as

$$
\alpha_e=\begin{cases} \sum_{k=1}^{N_m}(\mathbf{u}_e^{(k)})^T\mathbf{k}_0\mathbf{u}_e^{(k)} & \text{when} \quad \xi_e^{(k)}=1 \\ 0 & \text{when} \quad \xi_e^{(k)}=\xi_{\min}. \end{cases}
\tag{50}
$$

By this model the topology of a periodic structure is defined by the representative unit cell, because the whole structure is divided into N_m identical cells. Therefore, the stabilization schemes in the BESO method need only to be carried out for the representative unit cell. However, it should be pointed out that the finite element analysis still needs to be performed on the whole structure because the mechanical responses in different cells are not the same.

Figure 26a shows a 2D rectangular domain with $L=32$ and $H=20$. The inner core with height $h=16$ is the design domain. The plate is fixed on the left side and loaded vertically on the right side. Hard-kill BESO method is carried out for the design of the inner core space with a volume constraint of 50%. Figure 26b–e gives the design results corresponding to four different cell resolutions ($N_m=2\times1, 4\times2, 8\times4$ and 16×8), respectively.

The BESO method for generating periodic structures [51] has been adopted for the exploration a new type of lightweight footbridge in the form of perforated tubes (see Fig. 27). The left top figure of Fig. 27 shows the BESO results of the bridge with various cross-sectional shapes. The left bottom figure of Fig. 27 is a 3D printout of a section of the periodic bridge design. The practicality of the optimal design was verified through a reinforced concrete prototype constructed in the laboratory at RMIT University as shown in the right figure of Fig. 27. The same
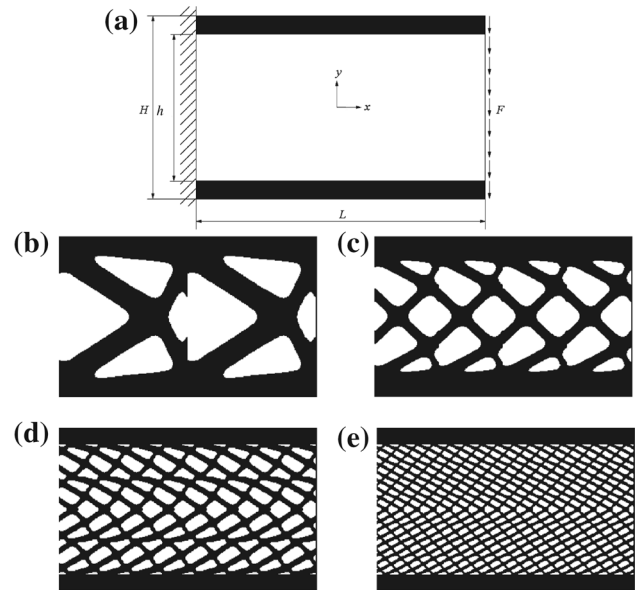

Fig. 26 BESO design of a periodic sandwich cantilever: **a** problem definition, **b** design for $N_m=2\times1$, **c** design for $N_m=4\times2$, **d** design for $N_m=8\times4$, **e** design for $N_m=16\times8$ [51]
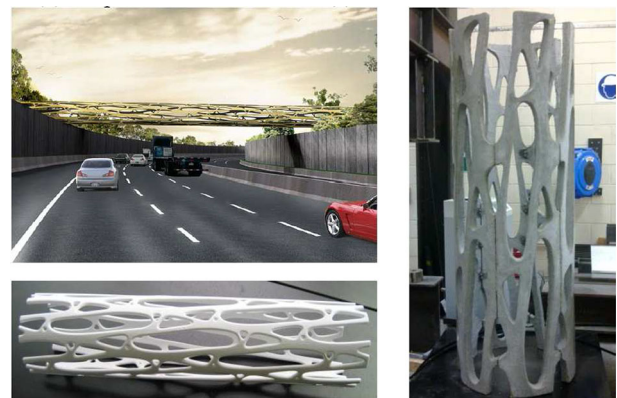

Fig. 27 BESO periodic design of a footbridge: proposal of the footbridge (*left top*), 3D printout of a section (*left bottom*), reinforced concrete prototype of a section (*right*) [56]

method has also been adopted by Zuo et al. [191] for the design of wheels with rotationally periodic patterns (see Fig. 28).

4.7 Reinforcement Design of Underground Excavations

Underground excavation in either soil or rock induces complex stress redistribution around the opening principally depending on excavation geometry, in situ stresses and material properties. Finding the optimal shape for an excavation based on stress distribution has practical significance in increasing stability and lowering support costs. Following the original stress level based rejection criterion, the ESO method was firstly applied for underground
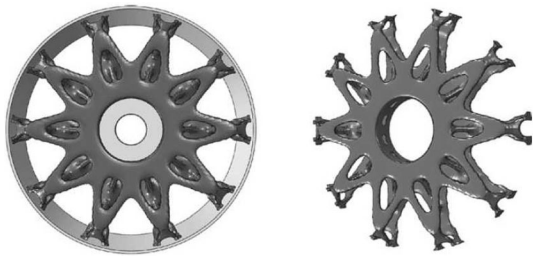
Fig. 28 CAD model of the ten-cell optimal design of the 3D wheel: front view (*left*) and perspective view of the wheel core (*right*)[191]

excavation shape optimization by Ren et al. [113]. Liu et al. [82] tackled tunnel designs by a namely fixed-grid bidirectional evolutionary structural optimisation (FG BESO). An extension of the hard-kill BESO method for a simultaneous optimization of shape and distributed reinforcement of an underground excavation was provided by Ghabraie et al. [38] for the linear elastic case. Further extensions of the BESO method to handle nonlinear materials were provided by Nguyen et al. [95] and Ren et al. [114]. Representative design results for underground excavation shape optimization and reinforcement optimization obtained by using the ESO-type methods are shown in Figs. 29 and 30, respectively.

The above-mentioned works performed shape optimization rather than topology optimization using the ESO-type methods, which means that a fixed topology of the structure is kept, i.e. no new holes shall be created to alter the original topology. In the numerical implementation, this requires no element to be removed or added except those on the boundary. To do so, an identification of boundary elements needs to be carried at the first hand. The sensitivity number ranking and element removal/addition are thereafter performed on only the identified boundary elements.

5 Design of Material Microstructures

Topology optimization has also been widely applied for design advanced materials since the pioneering work by Sigmund [123, 125]. Combined with the inverse
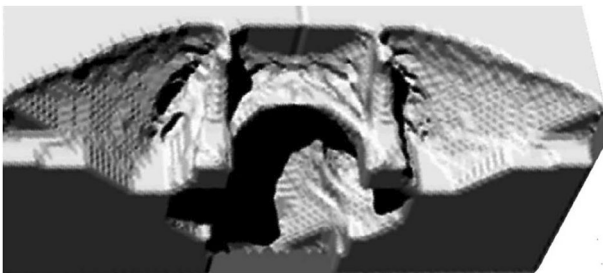

Fig. 29 ESO shape optimization of an excavation at a tunnel intersection [113]
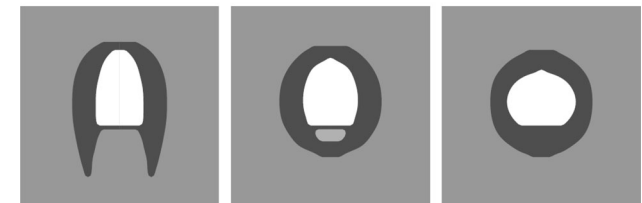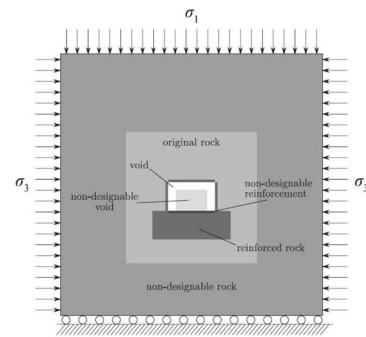

Fig. 30 Simultaneous optimization of shape and distributed reinforcement of an underground excavation using the hard-kill BESO method: *top figure* is a single tunnel under biaxial stress; *bottom figures* are the design results for load ratios of $\sigma_3/\sigma_1 = 0.4$ (*left*), $\sigma_3/\sigma_1 = 0.7$ (*middle*) and $\sigma_3/\sigma_1 = 1.2$ (*right*) [38]

homogenization method, topology optimization has been showing astonishing potentiality in design of materials with tailored constitutive properties. A series of works on the subject has been conducted using the density-based approaches afterwards concerning material properties such as thermal expansion coefficients (e.g., [39, 129]), viscoelastic behavior (e.g., [2, 16, 178]) and fluid permeability (e.g., [41, 42]). Some other works fall also into this context (e.g., [34, 66, 93, 94, 96, 134]). Similar works have also been readdressed using level-set methods (e.g., [14, 15, 143]. An overview on the subject has been given by Cadman et al. [13]. Up till now, the material topology design procedure follows a rather standard routine, which has been summarized in a recent educational paper by Xia and Breitkopf [147].

Following basically the same design routine, a series of extensions of the BESO method to material designs has been conduced by Xie and Huang's research group of in the RMIT University (e.g., [60]). It has been shown that the BESO method is not only applicable for material designs but also provides extraordinarily effectiveness in such designs for the sake of its heuristic update algorithm. In the following, we review first in Sect. 5.1 the standard material topology design routine. A series of categorized summaries on recent advancement of material designs using the BESO method is provided afterwards on design of materials with extreme properties (Sect. 5.2), design of isotropic/orthotropic materials (Sect. 5.3), design of functionally graded materials (Sect. 5.4), design of phononic/photonic bandgap materials (Sect. 5.5), and design of multiphysics materials (Sect. 5.6).

5.1 Material Topology Design

The key ingredient of material topology design is to evaluate properly the homogenized or the effective constitutive behavior of the considered cellular material microstructure. In most cases the cellular material is assumed to be periodically patterned at a separated lower scale compared to the macroscopic length scale as illustrated in Fig. 31. The periodic cellular material is also know as representative volume element (RVE) because it retains all information required to predict locally the macroscopic scale constitutive behavior. Considering design objectives and constraints related the evaluated effective properties, one may apply one method or another to update the cellular topology and repeat the procedure until the defined convergence is achieved. In the following we take the linear elastic case for instance and present several key ingredients with regard to material topology design including the homogenization theory, numerical implementations and optimization model settings.

5.1.1 Homogenization

The conventional homogenization method [40, 90] assumes two separated scales as illustrated in Fig. 31. Within the macroscopic domain Ω, the macroscopic displacement $\bar{u}(x)$, the macroscopic strain $\bar{\varepsilon}(x)$ and the macroscopic stress $\bar{\sigma}(x)$ are considered. Their counterparts at the microscopic scale are the displacement $u(x, y)$, the infinitesimal strain $\varepsilon(x, y)$ and the stress $\sigma(x, y)$. In the case of linear elasticity, we have the following relationship

$$\bar{\sigma}(x) = \mathbb{C}^{\text{hom}} : \bar{\varepsilon}(x) \tag{51}$$

in which the homogenized elastic stiffness tensor $\mathbb{C}^{\text{hom}}$ is to be determined by solving the RVE boundary value problem subject usually to periodic boundary conditions upon six independent overall strain values in the general 3D case.
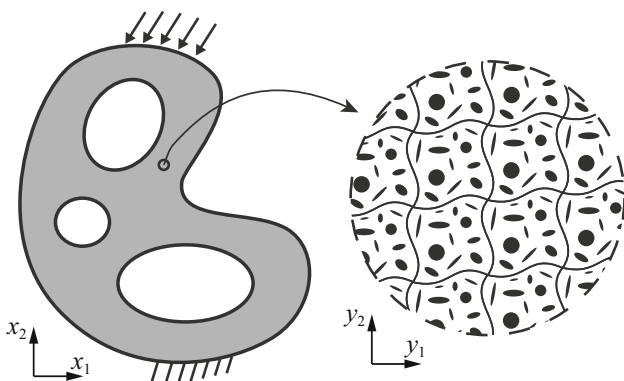

Fig. 31 Illustration of a two-scale structure and periodically patterned RVE [147]

Within the scope of linear elasticity, there exit two equivalent approaches for the determination of the effective or the homogenized stiffness tensor $\mathbb{C}^{\text{hom}}$ of periodically patterned microstructure [43]. One is the asymptotic approach, derived in a systematic way using the two-scale asymptotic expansion method [40]. Another is the energy-based approach [90, 123] employing the average stress and strain theorem as is the relationship presented in Eq. (51).

By the asymptotic approach, the homogenized stiffness tensor is given by averaging the integral over a specified the RVE Ω_{rve} as

$$C_{ijkl}^{\text{hom}} = \frac{1}{|\Omega_{\text{rve}}|} \int_{\Omega_{\text{rve}}} C_{ijpq}(\varepsilon_{pq}^{0(kl)} - \varepsilon_{pq}^{*(kl)}) \mathrm{d}\Omega_{\text{rve}}, \tag{52}$$

where the Einstein index summation notation is used and $\varepsilon_{pq}^{*(kl)}$ is the Ω_{rve}-periodic solution of

$$\int_{\Omega_{\text{rve}}} C_{ijpq} \varepsilon_{pq}^{*(kl)} \frac{\partial v_i}{\partial y_j} \mathrm{d}\Omega_{\text{rve}} = \int_{\Omega_{\text{rve}}} C_{ijpq} \varepsilon_{pq}^{0(kl)} \frac{\partial v_i}{\partial y_j} \mathrm{d}\Omega_{\text{rve}}, \tag{53}$$

where v is Ω_{rve}-periodic admissible displacement field and $\varepsilon_{pq}^{0(kl)}$ corresponds to the three (2D) or six (3D) linearly independent unit test strain fields.

The energy-based approach imposes the unit test strains directly on the boundaries of the RVE, inducing $\varepsilon_{pq}^{A(kl)}$ which corresponds to the superimposed strain fields $(\varepsilon_{pq}^{0(kl)} - \varepsilon_{pq}^{*(kl)})$ in (52). Detailed implementation of periodic boundary conditions will be given in Sect. 5.1.2. Equation (52) can be rewritten in an equivalent form in terms of mutual energies

$$C_{ijkl}^{\text{hom}} = \frac{1}{|\Omega_{\text{rve}}|} \int_{\Omega_{\text{rve}}} C_{pqrs} \varepsilon_{pq}^{A(ij)} \varepsilon_{rs}^{A(kl)} \mathrm{d}\Omega_{\text{rve}}. \tag{54}$$

Whilst most works apply the asymptotic approach for the design of material microstructures (see [13]), its extension to nonlinear material designs is not a straightforward task. In contrast, the formulation of the energy-based approach (54) is more compact that facilitates the numerical implementation [123, 147] and its extension to nonlinear material designs is also rather straightforward (e.g., [141]). The energy-based approach is adopted for for the following derivations.

5.1.2 Periodic Boundary Conditions

The microscale stress field $\sigma(x, y)$ is evaluated by solving the RVE equilibrium problem subject to the overall strain $\bar{\varepsilon}(x)$. By the assumption of periodicity, the displacement field of the RVE subjected to a given strain $\bar{\varepsilon}(x)$ can be written as the sum of a macroscopic displacement field and a periodic fluctuation field $\tilde{u}$ [90]

$$u(x, y) = \bar{\varepsilon}(x) \cdot y + \tilde{u}(y), \tag{55}$$

such that

$$\langle \varepsilon(x, y) \rangle = \bar{\varepsilon}(x), \tag{56}$$

because $\langle \tilde{u} \rangle$ vanishes for its periodicity.

In practice, constraint of (55) cannot be directly imposed on the boundaries because the periodic fluctuation term $\tilde{u}$ is unknown. The general expression of (55) needs to be transformed into a certain number of explicit constraints between the corresponding pairs of nodes on the opposite surfaces of the RVE [159]. Consider a 2D RVE as shown in Fig. 32, the displacements on a pair of opposite boundaries are

$$\begin{cases} u(x, y)^{k+} = \bar{\varepsilon}(x) \cdot y^{k+} + \tilde{u}(y) \\ u(x, y)^{k-} = \bar{\varepsilon}(x) \cdot y^{k-} + \tilde{u}(y) \end{cases} \tag{57}$$

where superscripts "$k+$" and "$k-$" denote the pair of two opposite parallel boundary surfaces that are oriented perpendicular to the k-th direction. The periodic term $\tilde{u}$ can be eliminated through the difference between the displacements

$$u(x, y)^{k+} - u(x, y)^{k-} = \bar{\varepsilon}(x) \cdot (y^{k+} - y^{k-}). \tag{58}$$

With specified $\bar{\varepsilon}(x)$, the right-hand side becomes a constant and such equations can be easily imposed in the the finite element analysis as nodal displacement constraint equations. At the same time, this form of boundary conditions meets the periodicity and continuity requirements for both displacement as well as stress when using displacement-based finite element analysis [160].

5.1.3 FEM Solution to Periodic RVE Problem

When both the geometry and the loading exhibit symmetries, which is the case here, the periodic boundary conditions can be simplified to conventional boundary conditions [45]. To keep the derivations general, such simplification is not applied here. Instead, the periodic
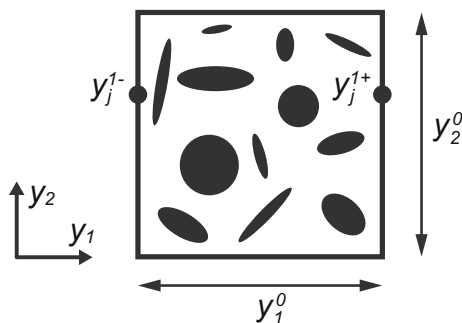

Fig. 32 An illustrative 2D rectangular RVE [146]

boundary conditions are imposed in a direct manner as presented previously. With regard to the finite element solution of Equation (58), the direct solution scheme by eliminating the redundant unknowns is adopted here. Note that, apart from the direct solution scheme, there exist two other types of solution schemes using penalty methods and Lagrange multipliers [90].

Separating the global displacement vector $\mathbf{u}$ into four parts: $\mathbf{u}_1^*$ denotes the prescribed displacement values, $\mathbf{u}_2$ denotes the unknowns corresponding to the interior nodes, $\mathbf{u}_3$ and $\mathbf{u}_4$ denote unknowns corresponding to the nodes located on the opposite boundaries of the base cell satisfying $\mathbf{u}_4 = \mathbf{u}_3 + \mathbf{w}^*$, where $\bar{\mathbf{w}}$ is a prescribed value computed via a given $\varepsilon^{0(kl)}$ according to Equation (58). The equilibrium equation the RVE problem can be expanded to

$$\begin{bmatrix} \mathbf{K}_{11} & \mathbf{K}_{12} & \mathbf{K}_{13} & \mathbf{K}_{14} \\ \mathbf{K}_{21} & \mathbf{K}_{22} & \mathbf{K}_{23} & \mathbf{K}_{24} \\ \mathbf{K}_{31} & \mathbf{K}_{32} & \mathbf{K}_{33} & \mathbf{K}_{34} \\ \mathbf{K}_{41} & \mathbf{K}_{42} & \mathbf{K}_{43} & \mathbf{K}_{44} \end{bmatrix} \begin{bmatrix} \mathbf{u}_1^* \\ \mathbf{u}_2 \\ \mathbf{u}_3 \\ \mathbf{u}_4 \end{bmatrix} = \begin{bmatrix} \mathbf{f}_1 \\ \mathbf{f}_2 \\ \mathbf{f}_3 \\ \mathbf{f}_4 \end{bmatrix}, \tag{59}$$

where $\mathbf{f}_1$ is an unknown vector and equals to the reaction forces at the nodes with prescribed displacements, $\mathbf{f}_2 = \mathbf{0}$, and $\mathbf{f}_3 + \mathbf{f}_4 = \mathbf{0}$ due to the assumption of periodicity. Note that $\mathbf{K}$ is symmetric, i.e. $\mathbf{K}_{ij} = \mathbf{K}_{ji}$ in (59). Eliminating the first row, adding the third and fourth rows, and using the relationship $\mathbf{u}_4 = \mathbf{u}_3 + \mathbf{w}^*$ reduces Equation (59) to

$$\begin{bmatrix} \mathbf{K}_{22} & \mathbf{K}_{23} + \mathbf{K}_{24} \\ sym. & \mathbf{K}_{33} + \mathbf{K}_{34} + \mathbf{K}_{43} + \mathbf{K}_{44} \end{bmatrix} \begin{bmatrix} \mathbf{u}_2 \\ \mathbf{u}_3 \end{bmatrix}$$
$$= -\begin{bmatrix} \mathbf{K}_{21} \\ \mathbf{K}_{31} + \mathbf{K}_{41} \end{bmatrix} \mathbf{u}_1^* - \begin{bmatrix} \mathbf{K}_{24} \\ \mathbf{K}_{34} + \mathbf{K}_{44} \end{bmatrix} \mathbf{w}^*. \tag{60}$$

and allows for the solution of the system.

5.1.4 Optimization Model

By the finite element method, the cellular material is discretized into N_e finite elements and the same number of topology design variables $\boldsymbol{\eta} \in \mathbb{R}^{N_e}$ are correspondingly defined. The homogenized elastic stiffness tensor derived from the energy-based approach (54) can be approximately written in the form

$$C_{ijkl}^{hom} = \frac{1}{|\Omega_e|} \sum_{e=1}^{N_e} (\mathbf{u}_e^{A(ij)})^T \mathbf{k}_e(\eta_e) \mathbf{u}_e^{A(kl)} \tag{61}$$

where $\mathbf{u}_e^{A(kl)}$ are element displacement solutions corresponding to the unit test strain fields $\varepsilon^{0(kl)}$. $\mathbf{k}_e = \eta_e \mathbf{k}_0$ is the element stiffness matrix and η_e takes values η_{min} (a small positive value) and 1 indicating void and solid materials, respectively. $\mathbf{k}_0$ is the element matrix of solid material.

The mathematical formulation for the design of cellular material with extreme properties reads as follows

$$\min_{\boldsymbol{\eta}} : \quad f_{\text{obj}}\big(C_{ijkl}^{\text{hom}}(\boldsymbol{\eta})\big)$$

$$\text{subject to} : \quad \mathbf{K}\mathbf{u}^{A(kl)} = \mathbf{f}^{(kl)}, k, l = 1, \dots, d \tag{62}$$

$$: \quad V(\boldsymbol{\eta}) = \sum v_e \eta_e = V_{\text{req}}$$

$$: \quad \eta_e = \eta_{\min} \quad \text{or} \quad 1, e = 1, \dots, N_e$$

where $\mathbf{K}$ is the global stiffness matrix, $\mathbf{u}^{A(kl)}$ and $\mathbf{f}^{(kl)}$ are the global displacement vector and the external force vector of the test case (kl), respectively. d is the spatial dimension, v_e is the element volume, $V(\boldsymbol{\xi})$ and V_{req} are the total and required material volumes, respectively.

The objective $f_{\text{obj}}(C_{ijkl}^{H}(\boldsymbol{\eta}))$ is a function of the homogenized stiffness tensors. For instance, the maximization of the material bulk modulus in the 2D case corresponds to the minimization of

$$f_{\text{obj}} = -\big(C_{1111}^{\text{hom}} + C_{1122}^{\text{hom}} + C_{2211}^{\text{hom}} + C_{2222}^{\text{hom}}\big) \tag{63}$$

and the maximization of material shear modulus corresponds to the minimization of

$$f_{\text{obj}} = -C_{1212}^{\text{hom}}. \tag{64}$$

The sensitivity of the objective function $\partial f_{obj}/\partial \eta_e$ can be computed using [123]

$$\frac{\partial C_{ijkl}^{\text{hom}}}{\partial \eta_e} = \frac{1}{|\Omega_e|} (\mathbf{u}_e^{A(ij)})^T \mathbf{k}_0 \mathbf{u}_e^{A(kl)}, \tag{65}$$

in accordance with the adopted objective definition.

With the evaluated sensitivity at hand, we can optimize the topology of the cellular material towards one optimum solution following the standard BESO update procedure presented in Sect. 2. A series of categorized summaries on recent advancement of material designs using the BESO method is provided in the following sections.

5.2 Design of Materials with Extreme Properties

Huang et al. [60] have extended for the first time the BESO method for the design of material microstructures with maximized elastic moduli. Following basically the same design routine as presented in the previous section, material microstructures of certain prescribed porosities can be designed by using the BESO method for both 2D and 3D cases, yielding maximized effective bulk and shear moduli (see Figs. 33 and 34). Figure 33 gives the designed material microstructures with maximized bulk moduli where the volume fractions of the solid are 50% in both 2D and 3D cases. Figure 34 shows the design material microstructures with maximized shear moduli where the volume fractions of the solid are 45 and 30% in 2D and 3D cases, respectively.

With the adoption of th multiphase material interpolation models in Sect. 4.1, Radman et al. [112] have further extend the work in [60] for the design of multiphase
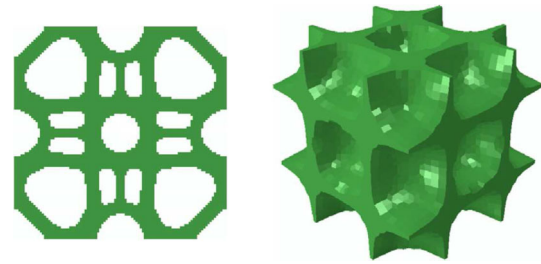

Fig. 33 Materials with maximized bulk moduli in 2D/3D cases [60]
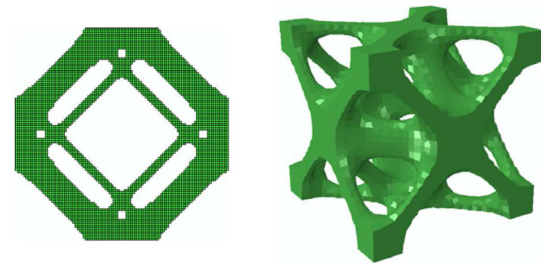

Fig. 34 Materials with maximized shear moduli in 2D/3D cases [60]

material microstructures. The designed extreme material composites made of 3 different constituent phases are given in Figs. 35 and 36 for bulk modulus maximization and shear modulus maximization, respectively.. A particular merit of the multiphase BESO method lies in the fact that distinctive interfaces are guaranteed between constituent phases in the generated microstructures which make the manufacturing of generated materials quite straightforward in comparison to the other multiphase topology optimization approaches.

Another extension of the work in [60] has been provided by Huang et al. [64] for design composite materials with optimized viscoelastic characteristics, such as damping or stiffness maximization at the operation frequency along a certain direction. The viscoelastic response of materials is often utilized for wide applications such as vibration reduction devices. In their work, both storage and loss moduli of composite materials are calculated through the

Fig. 35 Multiphase materials with maximized bulk moduli in 2D/3D cases, where the Young's moduli for *dark blue*, *light blue* and *yellow* are 4, 2, 1, respectively; the prescribed volume fractions of for three phases are 30, 40, 30% in the 2D case and 30, 50, 20% in the 3D case [112]. (Color figure online)
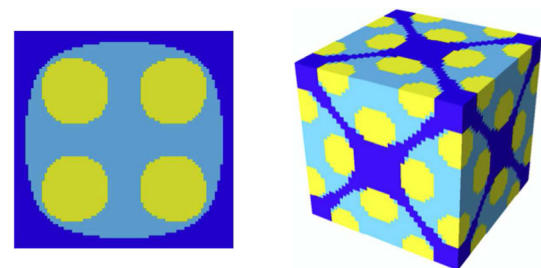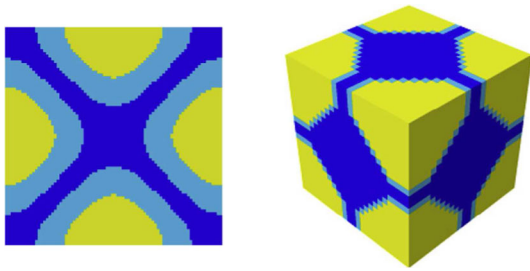
Fig. 36 Multiphase materials with maximized shear moduli in 2D/3D cases, where the Young's moduli for *dark blue*, *light blue* and *yellow* are 4, 2, 1, respectively; the prescribed volume fractions of for three phases are 30, 40, 30% in the 2D case and 25, 45, 30% in the 3D case [112]

homogenization analysis using complex variables. Composites made of two constituent phases, stiff elastic phase and soft viscoelastic phase, are designed using the BESO method for the damping maximization along both x- and y-directions in the 2D case as shown in Fig. 37. By their work, it has been shown that the damping property of composites can be greatly enhanced by properly mixing a small amount of a viscoelastic material with an elastic material, whilst negligible improvement on the stiffness of composites.

It has been shown that the BESO method is quite efficient and robust in designing materials. The number of design iterations for the design is linked to the material removal ratio in the BESO method, which results in in general less iterations required using the BESO method in comparison to the other approaches according to the authors' experience. In addition, the BESO method appears less suffering from the non-uniqueness issue in designing periodic microstructures for the sake of its intuitive variables updating scheme, which makes the BESO method an efficient design tool for material microstructural architecture.

5.3 Design of Isotropic and Orthotropic Materials

As can be observed from the representative results in the last subsection (e.g., Figs. 33, 34, 35, 36), square

Fig. 37 Optimized results for maximizing damping of composites made of stiff elastic phase (*black*) and soft viscoelastic phase (*white*) where the volume fractions of viscoelastic phase are 20, 40, 60% and corresponding loss tangents are 0.53, 0.61, 0.64 from *left to right*, respectively [64]

symmetry is automatically maintained for bulk and shear moduli maximization designs when a square symmetric initial topology guess is used and periodic boundary conditions are implemented. In practice, it is highly attractive to be able to design materials possessing particular symmetric properties to yield desirable performances. For instance, isotropic materials, in which the properties of materials are invariant with respect to material orientation, are the most common materials used in industry and attractive for engineering applications [5]. To do so, additional constraints on the relationships of the homogenized elastic tensors need to be introduced to the basic material optimization model of (62) presented in Sect. 5.1.4.

On top of the seminal work [60], Radman et al. [109] extended the BESO method for the bulk/shear modulus maximization design subject to both an isotropy constraint and a volume constraint such as

$$
\begin{aligned}
\min_{\boldsymbol{\eta}} : \quad & f_{\text{obj}}(C_{ijkl}^{\text{hom}}(\boldsymbol{\eta})) \\
\text{subject to} : \quad & \mathbf{Ku}^{A(kl)} = \mathbf{f}^{(kl)}, k, l = 1, \ldots, d \\
: \quad & g_{\text{iso}}(C_{ijkl}^{\text{hom}}(\boldsymbol{\eta})) = 0 \\
: \quad & V(\boldsymbol{\eta}) = \sum v_e \eta_e = V_{\text{req}} \\
: \quad & \eta_e = \eta_{\min} \quad \text{or} \quad 1, \text{e} = 1, \ldots, N_e
\end{aligned}
\tag{66}
$$

in which the isotropy constraint is defined satisfying in the 2D plane stress case

$$
g_{\text{iso}} = C_{1111}^{\text{hom}} + C_{2222}^{\text{hom}} - (C_{1122}^{\text{hom}} + C_{2211}^{\text{hom}}) - 4C_{1212}^{\text{hom}} = 0
\tag{67}
$$

and in the 3D case

$$
\begin{aligned}
g_{\text{iso}} = {} & 2(C_{1111}^{\text{hom}} + C_{2222}^{\text{hom}} + C_{3333}^{\text{hom}}) - (C_{1122}^{\text{hom}} + C_{3311}^{\text{hom}} \\
& + C_{2233}^{\text{hom}} + C_{2211}^{\text{hom}} + C_{1133}^{\text{hom}} + C_{3322}^{\text{hom}}) \\
& - 4(C_{2323}^{\text{hom}} + C_{1313}^{\text{hom}} + C_{1212}^{\text{hom}}) = 0.
\end{aligned}
\tag{68}
$$

To solve the above problem, a Lagrange multiplier is introduced to make a balance between fulfillment of the objective function and the isotropy constraint such that

$$
f_{\text{obj}}^* = (1 - |\lambda|)f_{\text{obj}} + \lambda + g_{\text{iso}}
\tag{69}
$$

where the Lagrange multiplier $\lambda \in [-1, 1]$ is determined using a bisection algorithm to satisfy the isotropy constraint [109]. It can be seen that the modified objective function is equivalent to the original one when the isotropy constraint is satisfied.

Isotropic materials with maximized bulk or shear modulus in both 2D and 3D cases have been provided in [109]. For illustration, Fig. 38 compares the material design results for shear modulus maximization design with and without the isotropy constraint. The volume fraction constraint of the solid phase is 25%. The comparison clearly show the difference between designing square symmetric

cellular materials without the isotropy constraint and isotropic cellular materials with the isotropy constraint.

Following basically the same design procedure of [109], Yang et al. [173] extended the BESO method for designing the stiffest orthotropic material with prescribed ratios for Young's moduli, where the ratios between the Young's moduli in three directions indicate the level of orthotropy and the bulk modulus indicates the overall stiffness. Figure 39 gives several orthotropic material design results with 50% volume constraint for various modulus ratios $a_{13} = a_{23}$ from 1.0 to 0.5, where a_{13} is the ratio of the moduli along direction 1 and 3 and similarly for a_{23}. Starting with $a_{13} = a_{23} = 1.0$, it can observed from Fig. 39a that materials are mainly distributed on three orthogonal panels yielding high moduli along the three directions. When the panels in-plane of axes 1 and 2 becomes thinner as shown in Fig. 39b, c, the two in-plane moduli along directions 1 and 2 are accordingly reduced. With $a_{13} = a_{23} = 0.7$ in Fig. 39d, the stiffeners are only left at the four corners and materials from those stiffeners are re-distributed to the four longitudinal panels with the increase of the thickness. As $a_{13} = a_{23}$ further decreases as in Fig. 39e, f, the in-plane stiffeners are completely removed and the four longitudinal panels form a cylinder-like topology, yielding relative high values of in plane moduli along directions 1 and 2.
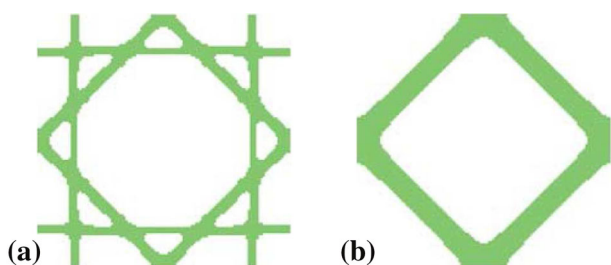

Fig. 38 Materials with maximized shear moduli: **a** with the isotropy constraint, **b** without the isotropy constraint [109]
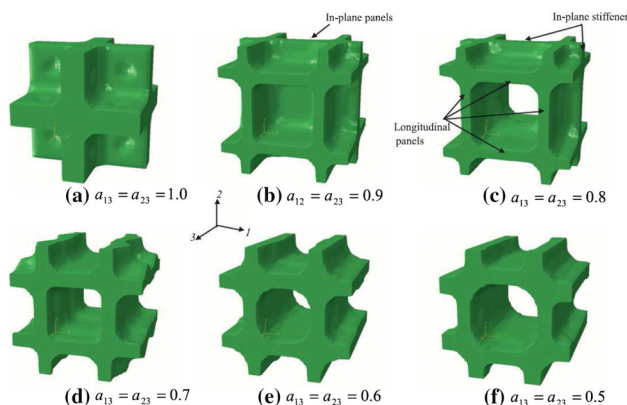

Fig. 39 Orthotropic material design results for various modulus ratios $a_{13} = a_{23}$ [173]

Another extension of the BESO method for the design of orthotropic materials was carried out by Xie et al. [166], in which a series of designs of orthotropic materials with various magnitudes of negative/zero compressibility in one or two directions were provided. Compressibility is a measure of the relative volume change of a solid or fluid as a response to a pressure change. Usually a material contracts in all directions when the pressure increases. However there are some exceptional materials which expand under hydrostatic pressure in one or two directions. There has been increasing interest in the negative compressibility behavior, mostly due to its many potential applications such as sensitive pressure sensors, pressure driven actuator and optical telecommunication cables. Apart form providing numerical designs in [166], a physical prototype of one of such material designs is fabricated using a 3D printer and tested in the laboratory under either unidirectional loading or triaxial compression. Figure 40 shows a typical negative linear compressibility (NLC) material design. In order to examine the behavior of the NLC design under uniform pressure, a triaxial compression test using a standard triaxial test machine commonly used for soil testing under hydraulic pressure. It is seen that the original cube has become narrower and taller under uniform pressure - a clear sign of the NLC effect.

5.4 Design of Functionally Graded Materials

Functionally graded materials (FGMs) have attracted great interest in recent years with applications in various areas such as aerospace/automotive structures and armor composites. As a category of inhomogeneous materials, FGMs demonstrate a gradual change in material properties. One way to design FGMs is to take advantage of variation in microstructural topology, i.e., using the microstructural design to determine the optimal spatial distribution of selected materials.
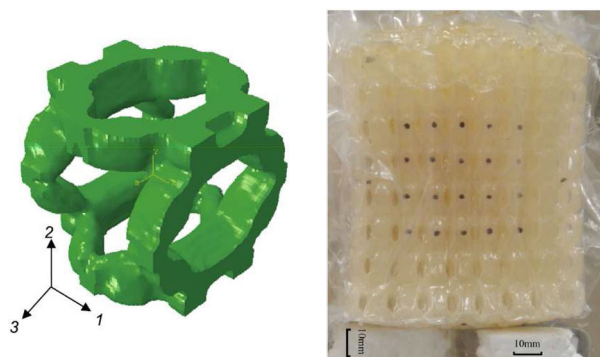

Fig. 40 A typical NLC material design and triaxial compression test on a correspondingly printed $8 \times 8 \times 8$ cells [166]

Radman et al. [110] introduced the application of BESO for the efficient design of cellular FGMs with a gradual variation of bulk or shear modulus. By this work, the design domain is divided into a series of connected cells and the elasticity characteristics within each cell are estimated using the homogenization theory. All cells are designed for the targeted stiffness with a desired gradation. In particular, the method addressed the connectivity issue of adjacent cells. Generally when designing the j-th cell, the connectivity of previous cells (as shown in Fig. 41) between cells j and $j-1$ and between $j-1$ and $j-2$ (if $j > 2$) is maintained by applying the filtering technique (15) over the these three cells together. Note that cells j, $j-1$ and $j-2$ are treated independently that cells j and $j-1$ are optimized for their individual targeted stiffness whilst the topology of cell $j-2$ is kept unchanged. Due to the effect of filtering, the material within cell $j-1$ is gradually redistributed to ensure its proper connections with neighboring cells $j-2$ and j.

An example is shown in Fig. 42 where eight cells were designed with variation in the average shear modulus from 40 to 5% of that of the solid phase. From the optimal design result, one could clearly observe that the optimized microstructures with proper connectivity between neighboring cells. The resulting shear moduli were in excellent agreement with the prescribed values along the gradation direction. A straightforward extension of the FGMs design procedure [110] has been conducted by Radman et al. [111] for stiffness maximization design of functionally graded materials with prescribed variation of thermal conductivity.

5.5 Design of Photonic/Phononic Bandgap Materials

Photonic crystals are optical structures consist of dielectric materials with different refractive indexes. They have lattice constants around the wavelength of light and periodicity in one, two or three dimensions. Photonic crystals are also called photonic band gap (PBG) structures because of their ability of prohibiting the propagation of electromagnetic waves within certain frequency ranges [29, 65]. In practice, a broader band gap means broader available bandwidth of signals and applications, so it is of great significance to design photonic crystals with large band gaps.

Toward an efficient and easy-implement optimization for photonic band gap structures, Meng et al. [88] extended recently the BESO method for maximizing photonic band gaps. Photonic crystals are assumed to be periodically composed of two dielectric materials of different permittivities. Based on the finite element analysis and sensitivity analysis, BESO starts from a simple initial design without any band gap and gradually re-distributes dielectric materials within the unit cell such that the resulting photonic crystal possesses a maximum band gap between two specified adjacent bands. Due to the polarization of electromagnetic waves, transverse magnetic polarization (TM mode) and transverse electric polarization (TE mode) can be considered separately. It has been shown that the design of photonic crystals is very sensitive to the change of the design variable when binary design variables are used ($\eta = \eta_{\min} or 1$) unless an extreme fine mesh is used. Instead of using an extreme fine mesh, the design variable of the BESO method in the work are assigned with discrete intermediate design values as is the case of (33)

$$\eta_e = \begin{cases} \min(\eta_e + \Delta\eta, 1) & \text{if} \quad \alpha_e \geq \alpha_{\text{th}} \\ \max(\eta_e - \Delta\eta, \eta_{\min}) & \text{if} \quad \alpha_e < \alpha_{\text{th}}, \end{cases} \quad (70)$$

where $\Delta\eta = 0.1$ is a user defined move limit.

Figure 43 gives several representative design results of photonic crystals for TE modes with maximum band gaps from the first to the third band and their corresponding band diagrams. It has been found that there exit many local optima for the design for PBG structures and the optimized result is highly dependent on the choice of initial guess.

The PBG design algorithm [88] has been afterwards extended for the design of photonic crystals with broad all-angle negative refraction (AANR) frequency range [89]. Negative refraction refers to the phenomenon that when light beams travel to the interface of two materials, they refract to the same side of the surface normal. By this work, the conditions of the occurrence of AANR are identified at the first hand and then the AANR frequency range is enlarged by the extended BESO design algorithm.

Meanwhile, the BESO method has also been extended for the design of phononic band gap crystals by Li et al.
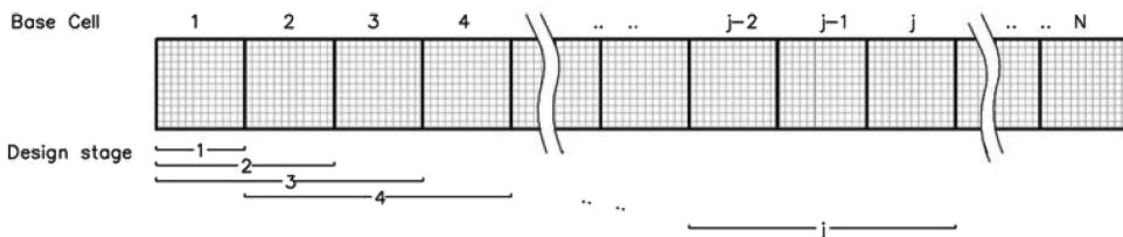

Fig. 41 Illustration of the progressive FGMs design procedure [110]

Fig. 42 3D FGMs with variation in shear moduli: **a** optimized microstructures, **b** cross section of FGMs showing internal structure [110]
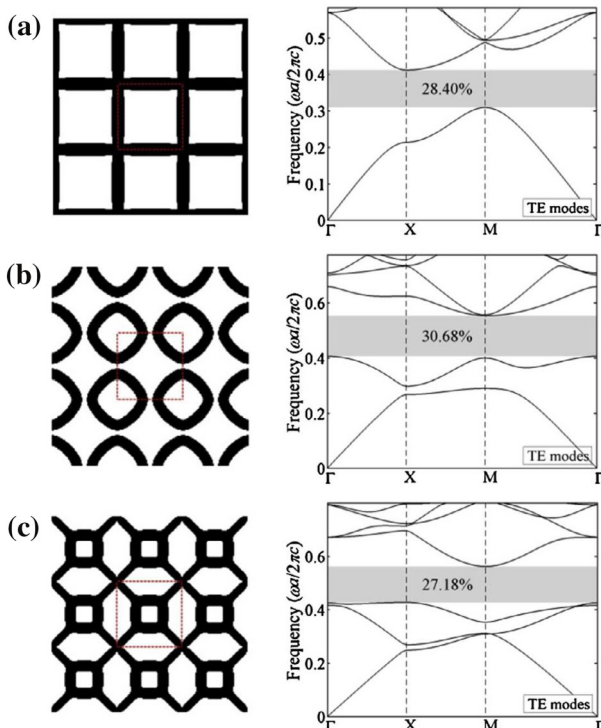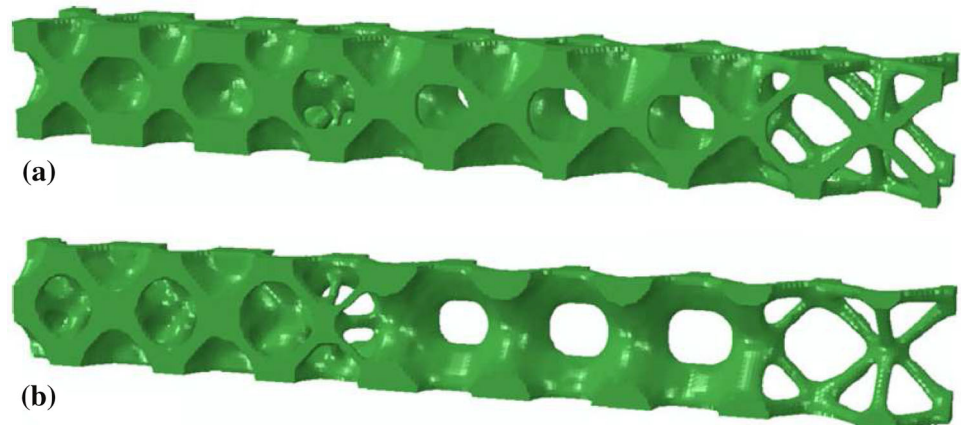

Fig. 43 Optimized 3×3 unit cells of *photonic crystals* and their band diagrams for TE band gaps where the *black* and *white colors* represent gallium arsenide and air, respectively: **a** the first band gap, **b** the second band gap, **c** the third band gap [88]

[79]. Phononic crystals are usually artificial periodic inhomogeneous composites which are constructed with inclusions embedded in a substrate, and their constituents have high contrast in mechanical properties, such as elastic modulus and mass density [83]. One important and useful feature of phononic crystals is to forbid the propagation of elastic and acoustic waves within certain range of frequencies, for which they are also named phononic band gap crystals. Applications of phononic band gap crystals including sound insulation, shock isolations, acoustic wave filtering, waveguides, negative refraction as well as acoustic cloaking [99]. Since phononic crystals to elastic waves are similar to photonic crystals to electromagnetic waves, the contribution by Li et al. [79] follows straightforwardly the BESO design algorithm developed in [88] except that both band gaps for out-of-plane and in-plane waves have been considered for the design for phononic crystals. Considering the fact that the design of phononic structures may sustain a certain amount of static loadings, Li et al. [80] have further restrained the minimum bulk or shear modulus during the maximization design of band gaps size. Figure 44 shows several representative design results of phononic crystals for out-of-plane mode with an additional constraint on bulk modulus, which results in slim connection structures.

5.6 Design of Multiphysics Materials

Apart from mechanical properties as reviewed in the previous subsections, the BESO method has also been extended for the design of periodic composites with extreme transport properties [185] and with extreme magnetic permeability and electrical permittivity [61]. In both cases, periodic composites are assumed to be made of two material phases with high contrast constitutive behaviors. For given volume fractions of both material phases, the aim is to find one appropriate distribution such that the composite possesses an extreme or a desirable effective property. The basic procedure for the design of these multiphysics materials follows tightly the standard design procedure as presented in Sect. 5.1 except for the modification of the governing equation and interested effective property according to the dealing physic problem. By these works, we may conclude that the BESO method is equivalent efficient and robust in designing multiphysics materials.

Figure 45 shows two representative optimized composites targeting for the lower and higher Hashin-Strikman (HS) bounds [44], respectively. The transport property of
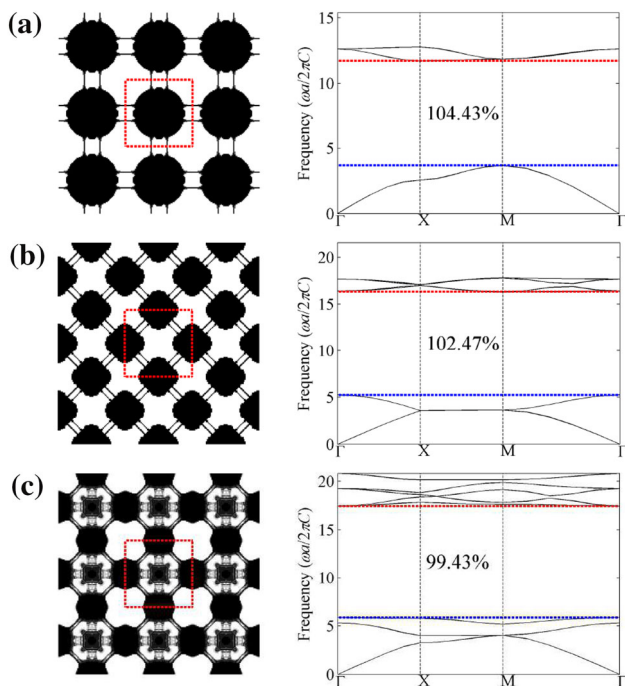
Fig. 44 Optimized 3×3 unit cells *phononic crystals* and their band diagrams for out-of-plane mode with bulk modulus constraint where the *black* and *white colors* represent silicon and air, respectively: **a** the first band gap; **b** the second band gap; **c** the third band gap [80]

the material denoted by green (light) is assumed 3 times of that of the material denoted by black (dark). The volume fraction of each material phase of the composite is set 50%. It can be observed from Fig. 45a that to reach the lower HS bound, the bi-connected low transport phase (black) forms a matrix separating the high transport phase (light green) and the high transport phase takes a circular shape. Oppositely from Fig. 45a, the areas occupied by low
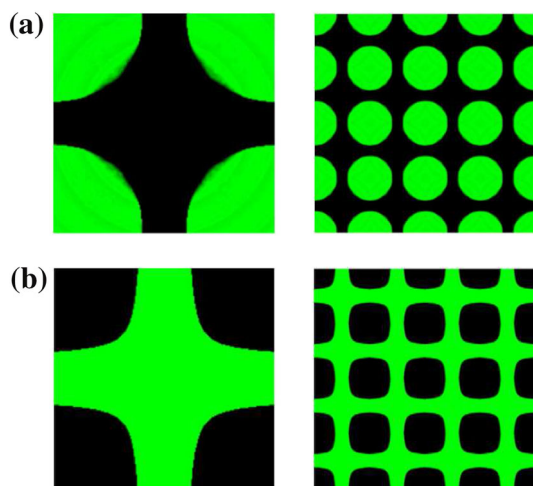

Fig. 45 Optimized unit cells and their corresponding 4×4 unit cells targeting for **a** the lower HS bound transport property, **b** the higher HS bound transport property [185]

transport phase are now occupied by the high transport phase in Fig. 45b , and vice versa to reach the higher HS bound.

6 Design of Multiscale Structures

In the recent years, there is an increasing use of high performance heterogeneous materials such as fibrous composite, concrete, metallic porous material and metal alloy for their advantageous overall characteristics, which result in superior structural mechanical response and service performance [150]. Though from the structural level point of view these materials can be considered homogeneous and conventional design approaches for homogeneous structures can still be used, the pronounced heterogeneities have significant impact on the structural behavior. Therefore, in order to allow for reliable mechanical designs, one needs to account for material microscopic heterogeneities and constituent behaviors so as to accurately assess the structural performance.

Meanwhile, the fast progress made in the field of material science allows us to control the material microstructure composition to an unprecedented extent [35, 152]. The overall behavior of heterogeneous materials depends strongly on the size, shape, spatial distribution and properties of the constituents. With all these in mind, one comes up naturally with the idea that designing materials simultaneously along with the design of structures would result in higher-performance structures. In addition, the recently emerging and rapidly developing techniques of 3D printing or additive manufacturing, such as fused deposition modeling, stereolithography, selective laser sintering, etc., provide the capability of manufacturing extremely fine and complex microstructures, which make it possible to generate more innovative, lightweight, and structurally efficient designs.

This section reviews recent applications and extensions of the BESO method to the design of multiscale structures, including: design of multiscale nonlinear structures (Sect. 6.1), design of materials for structural performance (Sect. 6.2), simultaneous design of structure and the underlying materials (Sects. 6.3 and 6.4).

6.1 Design of Multiscale Nonlinear Structures

Generally speaking, topology optimization design of multiscale structures (Fig. 46) can be viewed as an extension of conventional monoscale design except that the material constitutive law is governed by one or multiple representative volume elements (RVEs) defined at the microscopic scale. In the case of linear elasticity, topology optimization design of a structure made of the RVE is a rather

straightforward application of conventional linear design routine [55, 126], because the effective or homogenized constitutive behavior of the considered RVEs can be explicitly determined by homogenization analysis.

When nonlinearities are present at the microscopic scale, i.e., nonlinear RVEs are under consideration, topology optimization design of such multiscale structures is a rather challenging task. In particular the multiscale dilemma in terms of heavy computational burden is even more pronounced in topology optimization: not only is it required to solve the time-consuming multiscale problem once, but for many different realizations of the structural topology. For instance the most widely applied multiscale modeling approach, FE^2 following [28], asserts that each point of the macroscopic discretization is associated with a RVE of the (nonlinear) microstructured material. Then for each macroscopic equilibrium iteration a nonlinear load increment needs to be computed for each of the (many) RVEs. In return the average stress across the RVE is then used as the macroscopic stress tensor without requiring effective constitutive relations. A schematic illustration of the first-order computational method [36] is shown in Fig. 47.

Pioneering works on topology optimization of multiscale nonlinear structures have been conducted by the first author and and his collaborators [33, 146, 149]. A direct application of the BESO method for the design of multiscale nonlinear elastic structures within the FE^2 multiscale modeling framework have been given by Xia and Breitkopf [146]. As for more severe loading path dependent material nonlinearity such as plasticity, Fritzen et al. [33] have developed an extended BESO method with the adoption of an established model order reduction method potential-

based Reduced Basis Model Order Reduction (pRBMOR, [30–32]) and parallelization on modern Graphics Processing Units (GPUs). It has been shown that the implementation of pRBMOR with GPU acceleration enables to design multiscale elastoviscoplastic structures using the previously developed design framework in realistic computing time and with affordable memory requirement.

In general, FE^2-based multiscale structural design follows the same design algorithm that is presented in Sect. 4.5 , except for the application of the FE^2 method for the evaluation of structural performance. The stiffness maximization of nonlinear multiscale structures is formulated in consistent with the homogeneous case in (44) as

$$\begin{aligned} \max_{\xi} : \quad & f_w(\boldsymbol{\xi}, \bar{\mathbf{u}}) \\ \text{subject to} : \quad & \bar{\mathbf{r}}(\boldsymbol{\xi}, \bar{\mathbf{u}}) = \mathbf{0} \\ : \quad & V(\boldsymbol{\xi}) = \sum \xi_e v_e = V_{\text{req}} \\ : \quad & \xi_e = \xi_{\min} \text{or} 1, e = 1, \dots, N_e. \end{aligned} \quad (71)$$

Here $\bar{\mathbf{u}}$ is the macroscopic nodal displacement vector and $\bar{\mathbf{r}}$ denotes the macroscopic residual

$$\bar{\mathbf{r}}(\boldsymbol{\xi}, \mathbf{u}) = \bar{\mathbf{f}}_{\text{ext}} - \sum_{e=1}^{N_e} \xi_e \int_{\Omega_e} \bar{\mathbf{B}}^T \bar{\boldsymbol{\sigma}} \mathrm{d}\Omega_e. \quad (72)$$

in which $\bar{\mathbf{f}}_{\text{ext}}$ is the macroscopic loading force, $\bar{\mathbf{B}}$ is the macroscopically defined strain-displacement matrix and $\bar{\boldsymbol{\sigma}}$ is the macroscopic stress.

Figure 48 shows a two-scale cantilever structure made of periodically patterned anisotropic short-fiber reinforced composite. Following [181], the matrix material is assumed to be highly nonlinear while the fibers are assumed to be linear elastic and much more rigid than the matrix. The structural stiffness is to be maximized and the volume fraction constraint is 60%. It important to emphasize that it requires solving $4 \times 100 \times 50$ (4 Gauss integration points for each element) nonlinear RVE boundary value problems for each iteration of each load increment. This number would decrease progressively with iterations as the removed elements are no longer evaluated for the structural response.
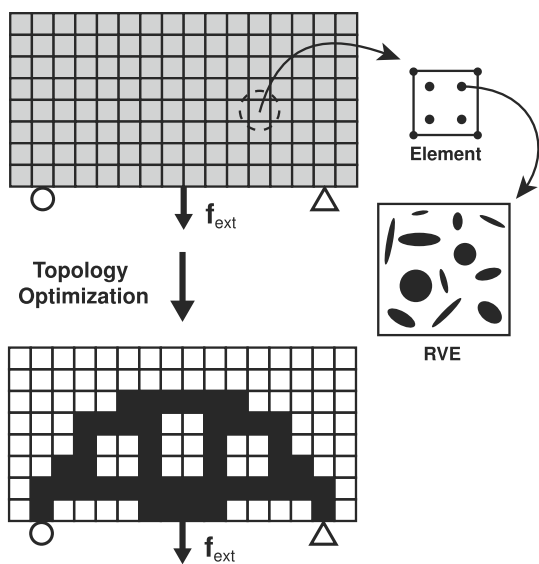

Fig. 46 Illustration of topology design of multiscale structures [146]
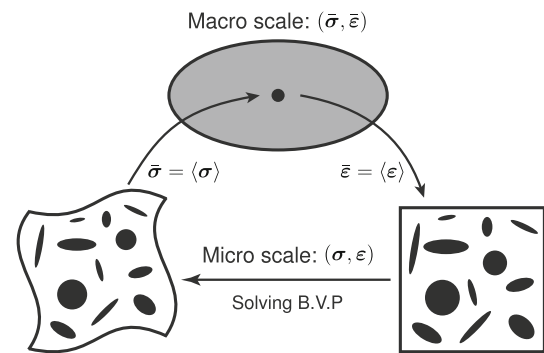

Fig. 47 First-oder computational homogenization scheme [146]

For the purpose of comparison, two different loading cases are considered and their corresponding designs are shown in Fig. 49. The topology shown in Fig. 49a is similar to the conventional linear design result, indicating that an external force load at the level of 0.01 N does not result in much difference in the design results. However, when the external load is increased to 0.2 N, one can observe obvious topological differences between the design results shown in Fig. 49a, b, which are due to the existence of the reinforcing fibers. The equivalent stress field of the topology solution in Fig. 49b is given in Fig. 50 together with the equivalent stress fields of the RVEs at several selected points. The elements neighboring the loading tip with high stress concentration are removed from the macroscale field plot for the purpose of illustration. From the deformed RVEs shown in Fig. 50, one can observe that the RVEs at points A and D are under compression, the RVE at point B is under tension, and the RVE at point C is subjected to a mechanical shear state, which are in agreement with their macroscale deformation states. One may also note from the stress fields that the presence of fibers results in higher stress concentrations at the interface of the matrix and the fibers. The higher stress concentrations are responsible for the initial material failure or crack at the microscopic scale which cannot be detected when using the conventional monoscale fracture analysis (e.g., [21]). There is also a potential application of such feature in stress-related topological designs (e.g., [25, 75, 157]), where the stress constraints may be considered to limit the maximum stress at the microscopic scale.

6.2 Design of Materials for Structural Performance

The optimized material microstructures as reviewed in Sect. 5 are only optimum in terms of general effective properties or certain desirable material properties. The structure made of the resulting materials may not be efficient or optimal for
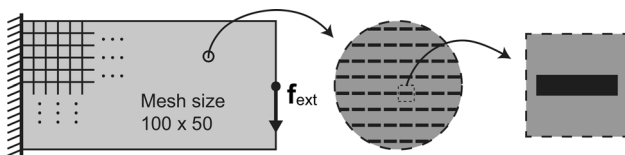

Fig. 48 A two-scale cantilever made of periodically patterned short-fiber reinforced composite [149]

Fig. 49 Design of two-scale structures in nonlinear elasticity for two different loading cases: **a** $\mathbf{f}_{\text{ext}} = 0.01$ N, **b** $\mathbf{f}_{\text{ext}} = 0.2$ N [149]
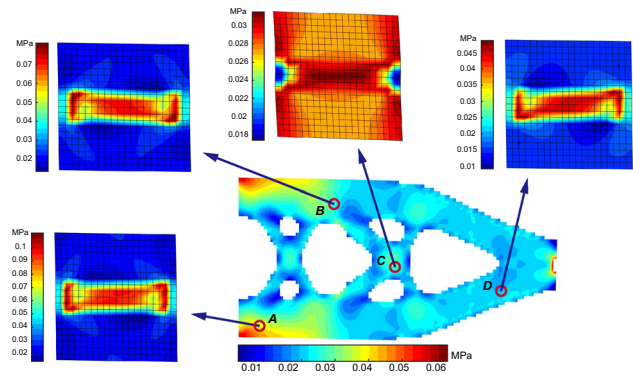

Fig. 50 The equivalent stress fields of Fig. 49b for the macroscale structure (deformation exaggerated 10 times) and for the microscale RVEs at selected points (deformation exaggerated 50 times) [149]

specific boundary conditions of practical service. For such reason, Huang et al. [62] extended the BESO method for the optimal design of the underlying material microstructures with the design objective of maximizing the macroscopic structural stiffness. By their work, the macroscale structure is assumed to be made of one universal material microstructure. The set of topology design variables $\boldsymbol{\eta}$ is defined at the microscopic scale. Note that upon the homogenization theory, the resulting material microstructures are infinitesimal in comparison to the macroscale structure. In other words, if the algorithm for designing periodic structures is adopted (Sect. 5.4), the homogenization based material design result corresponds to the periodic design result when number of periodic cells goes to infinity. A comparison study with this aim was provided by Xie et al. [165] and Zuo et al. [192].

The optimization model for this particular problem can be formulated as following

$$
\begin{aligned}
\max_{\boldsymbol{\eta}} : \quad & f_c(\boldsymbol{\eta}, \mathbf{u}) \\
\text{subject to} : \quad & \mathbf{K}(\boldsymbol{\eta})\mathbf{u} = \mathbf{f} \\
: \quad & V(\boldsymbol{\eta}) = \sum \eta_e v_e = V_{\text{req}} \\
: \quad & \eta_e = \eta_{\min} \text{ or } 1, e = 1, \ldots, N_e.
\end{aligned}
\tag{73}
$$

Different from the homogeneous case as (12), the global stiffness matrix in the above formulation is dependent on the topology of the underlying material microstructure

$$
\mathbf{K}(\boldsymbol{\eta}) = \sum_{e=1}^{N_e} \int_{\Omega_e} \mathbf{B}^T \mathbf{C}^{\text{hom}}(\boldsymbol{\eta}) \mathbf{B} \, d\Omega_e
\tag{74}
$$

in which $\mathbf{C}^{\text{hom}}$ is the homogenized elastic matrix governed by the microscale topology $\boldsymbol{\eta}$.

Figure 51a shows a two-scale half-MBB beam where the macroscale structure is discretized into $L \times H$ square shaped bilinear elements and the assumed microscale material model is discretized into 40×40 square shaped bilinear elements. The volume fraction of solid for the microscale material model is set to 60%, i.e., a micro-

(a) A two-scale half-MBB beam.

(b) L = 8, H = 16. (c) L = 24, H = 16. (d) L = 40, H = 16. (e) L = 56, H = 16.
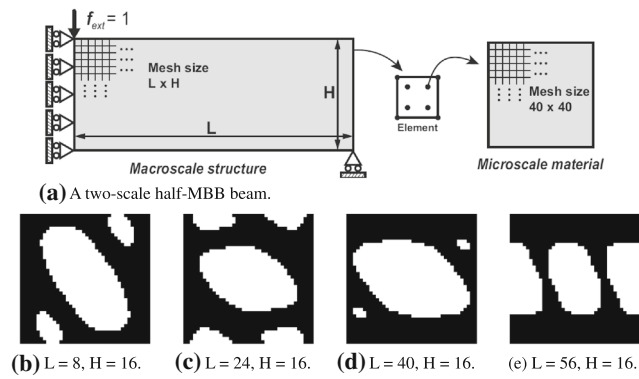
Fig. 51 A two-scale half-MBB beam and the optimized microstructures for different macroscale structure dimensions [149]

porosity of 40% is assumed. Fig. 51b–e give the optimized material topologies for different dimensions of the beam structure. The topological transition from Fig. 51b–e due to the increase of the beam length can be clearly observed. The increased beam length requires more bending resistance and results a shift of material distribution along vertical direction to horizontal direction.

Recently, Xia and Breitkopf [145] have used the BESO method and made a further step by designing pointwise varying material microstructures to maximize the macroscale structural stiffness. Within the multiscale modeling framework, the pointwise varying material microstructures are optimized in response to the macroscale structural response, meanwhile the optimized materials in turn modify the macroscopic constitutive behavior. The equilibrium problem at the macroscopic scale is therefore in general nonlinear (e.g., [10, 136]). In the work of [145], this scale-interface nonlinearity has been specially addressed by treating the microscale material design integrally as a generalized nonlinear constitutive behavior. The nonlinear interface equilibrium due to the locally optimized or adapted materials is addressed by means of FE^2 method. It has been shown that this FE^2-based design approach can provide similar topology solutions in comparison to the conventional design strategy (e.g., [62, 171]), while requiring much less computing cost due to the reduced interchange between the two scales. Another advantage of treating the material optimization process as a generalized constitutive behavior is that the existing model reduction strategies for nonlinear heterogeneous materials can be applied straightforwardly to improve the design efficiency [148].

Figure 52 shows a simple bridge-type structure and corresponding design result of the pointwise underlying material microstructures obtained by the FE^2-based design approach [145]. By reduced integration scheme, four Gauss integration points are defined for each finite element and in total 32 material models are considered at the microscopic
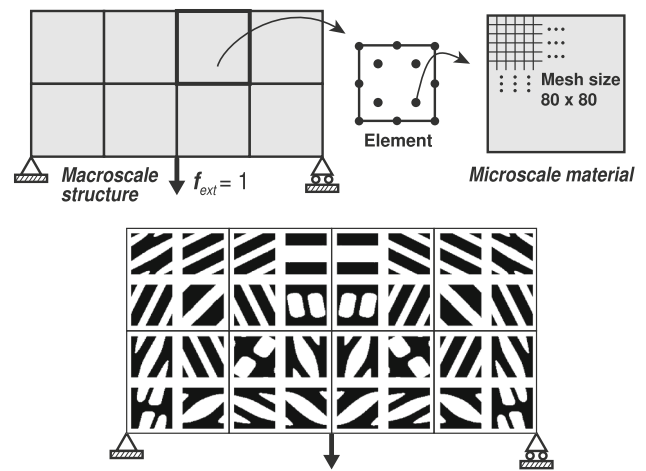

Fig. 52 Design of pointwise material microstructures for a bridge-type structure [145]

scale. Volume constraint for each cellular material model is set to 60%. Note that, Fig. 52 is a zoomed view of the design results, where the optimized cellular materials corresponding to the Gauss points are zoomed for the purpose of illustration. Upon the homogenization theory, the optimized cellular material only represents the optimal solution at the microscopic scale for that material point, i.e., Gauss integration point. Therefore, the optimized cellular materials in neighboring points represent only the tendency of the topological variations while are not necessarily continuous with their neighborhood.

6.3 Simultaneous Design of Structures and Materials

With the aforementioned works on material microstructural design, one comes up naturally with the idea of simultaneous design of both macrosacle structure and the underlying material microstructures. In other words, by topology optimization one determines not only the optimal spatial material layout distribution at the macroscopic structural scale, but also the optimal local use of the cellular material at the microscopic scale, as schematically shown in Fig. 53.

The most commonly applied strategy is designing a universal material microstructure at the microscopic scale for a simultaneously changed macroscale structure [171].

$$
\begin{aligned}
\min_{\boldsymbol{\rho},\boldsymbol{\eta}} : \quad & f_c(\boldsymbol{\rho}, \boldsymbol{\eta}, \mathbf{u}) \\
\text{subject to} : \quad & \mathbf{K}(\boldsymbol{\rho}, \boldsymbol{\eta})\mathbf{u} = \mathbf{f} \\
: \quad & V_\rho = \sum_{i=1}^{N_\rho} \rho_i = V_{\text{req}}^{\text{mac}} \\
: \quad & V_\eta = \sum_{j=1}^{N_\eta} \eta_j = V_{\text{req}}^{\text{mic}} \\
: \quad & \rho_i = \rho_{\min} \text{ or } 1, i = 1, \ldots, N_\rho \\
: \quad & \eta_j = \eta_{\min} \text{ or } 1, j = 1, \ldots, N_\eta,
\end{aligned}
\tag{75}
$$

where V_ρ and V_η are the total volumes of solid elements at the two scales, respectively. $V_{\text{req}}^{\text{mac}}$ and $V_{\text{req}}^{\text{mic}}$ are the required
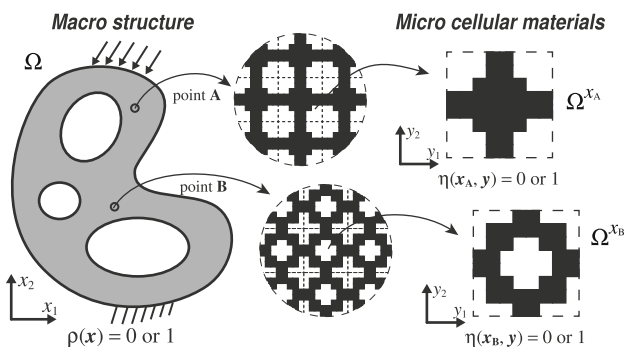
Fig. 53 Illustration of simultaneous topology optimization of structure the underlying materials [145]

volumes of solid elements defined at the two scales, respectively. The global stiffness matrix in the above formulation is dependent on both the topologies of the macroscale structure ρ and the underlying material microstructure η

$$\mathbf{K}(\boldsymbol{\rho},\boldsymbol{\eta}) = \sum_{e=1}^{N_\rho} \rho_e \int_{\Omega_e} \mathbf{B}^T \mathbf{C}^{\text{hom}}(\boldsymbol{\eta}) \mathbf{B} \mathrm{d}\Omega_e. \tag{76}$$

It has been shown by Yan et al. [171] that different from the continuum density-based method, the BESO method utilizing discrete design variables is more suitable for concurrent topology optimization of structures and materials because there is no need to assume any properties or microstructures for intermediate materials for finite element analysis. In [171] only one total weight fraction is constrained. According to the total weight fraction, the volume fractions for macro and micro scales are calculated rather than pre-assumed volume fractions. Alternatively, Xia and Breittkopf [149] readdressed the subject by constraining separately the volume fractions for the two scales. The same two-scale half-MBB beam problem considered previously in Fig. 51 is now readdressed for a simultaneous design, where both macroscale and microscale volume fraction constraints are set to 60%. As shown in Fig. 54, both scale topologies are updated iteratively and adaptively until the required material volume fractions are achieved.

Alternatively, Xia and Breitkopf [145] proposed an FE^2-based simultaneous design approach with the application of the BESO method for topology optimization at both scales. In this work, the material optimization process is treated as a generalized nonlinear constitutive behavior, and the resulting nonlinear scale-interface equilibrium problem is resolved using the FE^2 method. The proposed model enables to obtain optimal structures with spatially varying properties realized by the simultaneous design of microstructures. The same two-scale half-MBB beam structure (Fig. 51) has been investigated by the FE^2-based simultaneous design approach. The nonlinear scale-interface equilibrium is particularly addressed by the FE^2
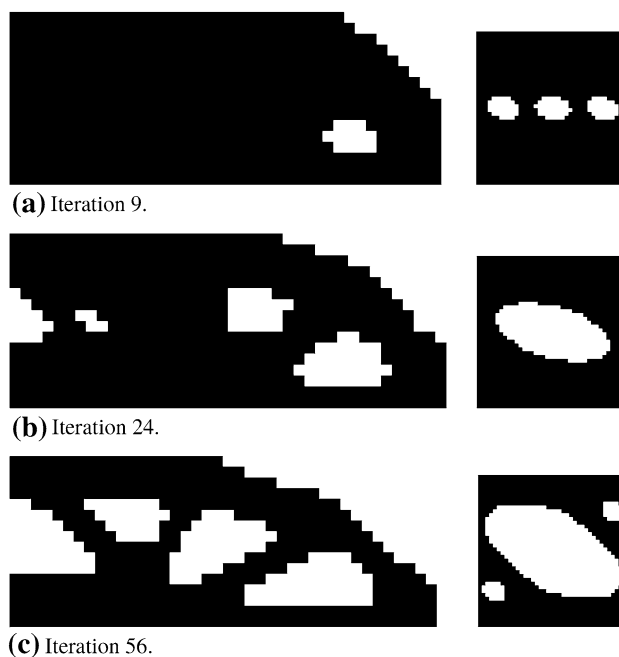

(a) Iteration 9.

(b) Iteration 24.

(c) Iteration 56.

Fig. 54 Simultaneous design of the two-scale half-MBB beam and the underlying material microstructure [149]. **a** Iteration 9. **b** Iteration 24. **c** Iteration 56

method with an initial stiffness Newton-Raphson solution scheme. Unlike the previous iterative design approach with the microscale topology updated iteratively along the macroscale topology design, the pointwise microscale micro-optimizations are solved completely for each Newton-Raphson iteration of each design iteration. Once the equilibrium is achieved, the macroscale topology is then optimized based on the converged solution response. The converged macroscale topology design result together with several typical microscale material topologies are shown in Fig. 55. Uniaxial materials may be sufficient at the main branches of the structure, while in order to have a higher structural performance, anisotropic materials have to be
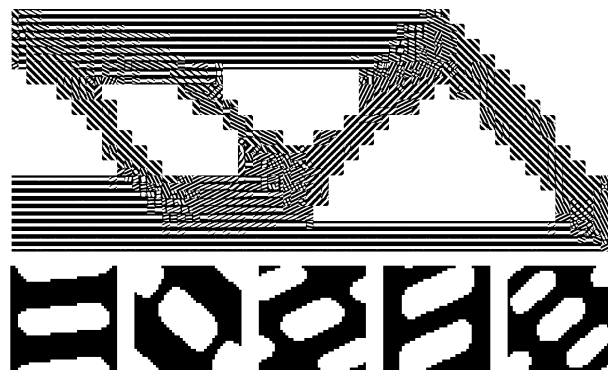

Fig. 55 FE^2-based simultaneous design of structure and the underlying pointwise material microstructures together with several typical microstructures [145]

used at the joints of the main branches due to the more complex loading status. Simultaneous design of structure and the underlying pointwise materials would improve the stiffness of the structure for almost 40% in comparison to Fig. 54c.

One particular advantage of treating the material optimization process as a generalized constitutive behavior is that the design efficiency can be drastically improved by a straightforward application of the existing model order reduction strategy for nonlinear materials. Xia and Breitkopf [148] have further integrated a reduced database model namely Numerically EXplicit Potentials (NEXP, [74, 181, 182]) to the simultaneous design framework. By the NEXP model, a database from a set of numerical experiments in the space of effective strain is built off-line. Each value in the database corresponds to the strain energy density evaluated on a material microstructure, optimized in accordance to the imposed effective strain value. As a result of this off-line phase, the effective strain-energy and stress-strain relations required for the macroscopic equilibrium solution can be evaluated in an explicit manner. As shown by Fig. 56, this explicit NEXP approximation can well serve the simultaneous design purpose providing ultra-resolution structures at a significantly reduced computational cost.

6.4 Other Simultaneous Designs

Upon the above reviewed works on simultaneous designs, there exist many other extended works on this subject using the BESO method. A short summary of these extended works on simultaneous design is provided below.

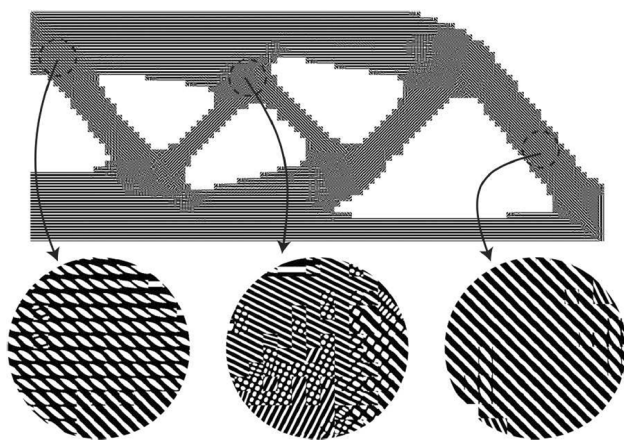With regard to dynamic problems, Zuo et al. [188] proposed a two-scale BESO optimization algorithm for

Fig. 56 FE^2-based simultaneous design of structure and the underlying pointwise material microstructures with the use of NEXP approximation for the generalized nonlinear constitutive behavior [148]

natural frequency maximization by means of simultaneous design macroscale structures and the microscale composite materials, where the two separate volume fraction constraints were assigned at two scales. Considering the limitation of setting two independent volume fraction constraints, Liu et al. [81] further extended the work by constraining the total weight of two-scale structure such that both scale volume fraction constraints are automatically determined. Instead of maximizing the natural frequency, Vicente et al. [139] extended the BESO method for minimizing the frequency responses of two-scale systems subject to harmonic loads. Another study on frequency response designs using the BESO method was conducted by Xu and Xie [167], by which the displacement response mean square is minimized subject to random excitations. Xu et al. [169] further carried out simultaneous design for the maximization of dynamic strain energy of a two-scale structure under dynamic loading based on the equivalent static loads. Figure 57 gives a representative design result of a clamped composite cantilever subject to a step load. It is assumed that the cantilever is made of two porous materials shown as the dark and light phases in Fig. 57a. By the simultaneous design, both the macroscale material layout (Fig. 57a) and the microscale architectures (Fig. 57b, c) are obtained for the a defined dynamic design objective.

With the multiple material phase interpolation scheme at hand (Sect. 4.1), it is straightforward to extend the above mentioned simultaneous design frameworks for the design of multi-phase two-scale structures. Xu et al. [170] proposed to design thermoelastic composite structures, where the macroscale structure is assumed to be made a composite material with three constituent phases. Da et al. [22] assumed the macroscale structure is made of two different composite materials and each of them consists of three to four material phases at the microscopic scale. Xu et al. [168] have also extended the dynamic compliance design of two-scale structures to the multi-phase case considering macroscale composite structures and microscale multi-phase microstructures. Figure 58a gives one representative
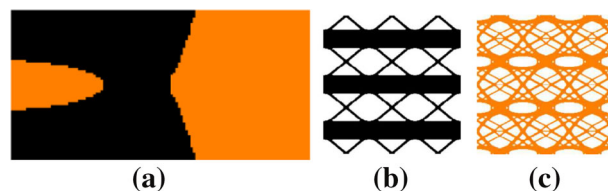

Fig. 57 Dynamic BESO simultaneous design of a composite cantilever clamped on the *left edge* subject to a step load in the middle of the *right edge*: **a** design result of the macroscale composite cantilever made of two porous underlying materials, **b** microstructural design result of the *dark phase*, **c** microstructural design result of the *light phase* [169]
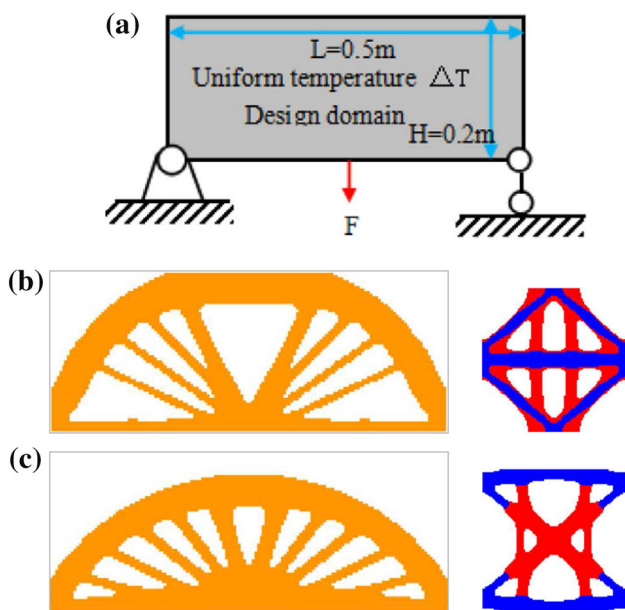
Fig. 58 BESO simultaneous design of a thermoelastic composite structure: **a** problem definitions, **b** design result for $\Delta T = 0°C$, **c** design result for $\Delta T = 500°C$ [170]

stiffness maximization design of a thermoelastic composite structure. The underlying composite material is assumed to be made of one void phase and two solid phases with different Young's moduli and thermal expansion coefficients. Figure 58b, c are the design results corresponding to cases of $\Delta T = 0°C$ and $\Delta T = 500°C$, respectively. It can be observed that the prescribed temperature has an clear influence on both macroscale and microscale topologies.

With the aim to design structures with multi-functional applications that require not only maximum structural stiffness but also superior thermal insulation capabilities, a multi-objective simultaneous design using the BESO method was conduced by Yan et al. [172]. To achieve the multi-functional needs, the two conflicting design objectives were taken into account to maximize structural stiffness at the macroscopic scale and minimize material thermal conductivity at the microscopic scale.

7 Matlab Codes for Benchmark Designs

Two Matlab codes "esoL.m" and "esoX.m" using the hard-kill BESO method are provided in the Appendix for benchmark designs of structures and material microstructures, respectively. Both codes are built on top of the 88-line code [3] with the implementation of the hard-kill BESO method. The second code "esoX.m" is a BESO version of a recent educational code "topX.m" developed by Xia and Breitkopf [147] for design of material

microstructures with extreme properties. It should be emphasized that the hard-kill BESO method is adopted here, however for programming consistency elements are not truly deleted but assigned with an extremely low Young's modulus. In addition, the BESO update algorithm presented in Sect. 2.5 is simplified here without adoption of the admission ratio control such that only one threshold α_{th} needs to be determined. The design domain is assumed to be rectangular and discretized into square plane stress elements. Please refer to the two seminal papers [3] and [147] for detailed explanations of the codes.

The main programs are called from the Matlab prompt by the commands

```
esoL(nelx,nely,volfrac,er,rmin,ctp)
```
and
```
esoX(nelx,nely,volfrac,er,rmin,ctp)
```

where `nelx` and `nely` denote the number of elements along the horizontal and vertical directions respectively, `volfrac` is the prescribed volume fraction, `er` is the evolutionary ratio, `rmin` is the filter radius, and `ctp` specifies the case type of benchmark design.

In the case of structural designs, `ctp` in "esoL.m" takes values 1, 2 and 3, denoting three benchmark design cases of stiffness maximization design subject to volume fraction constraint: half-MBB beam design (Fig. 59), clamped cantilever design (Fig. 60) and roller-supported half-wheel design (Fig. 61).

In the case of material microstructural designs, `ctp` in "esoX.m" takes values 1 and 2, denoting two benchmark design cases: bulk modulus maximization (Fig. 62) and shear modulus maximization(Fig. 63).
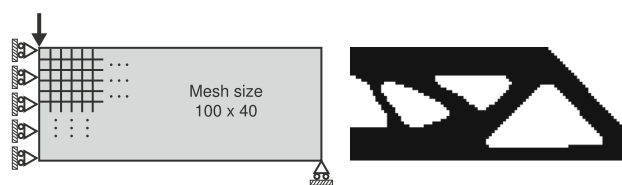

Fig. 59 Benchmark test case 1 of "esoL.m": a half-MBB beam design problem and the corresponding BESO design result obtained from calling esoL(100,40,0.6,0.02,6,1)
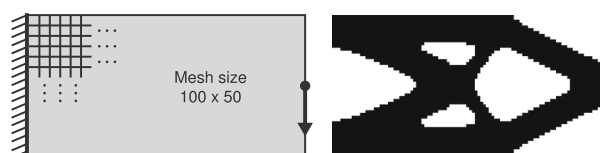

Fig. 60 Benchmark test case 2 of "esoL.m": a clamped cantilever design problem and the corresponding BESO design result obtained from calling esoL(100,50,0.6,0.02,6,2)
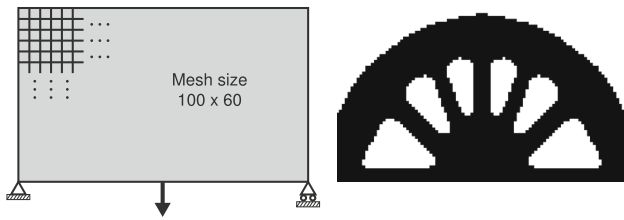
Fig. 61 Benchmark test case 3 of "esoL.m": a roller-supported half-wheel design problem and the corresponding BESO design result obtained from calling esoL(100,60,0.6,0.02,6,3)
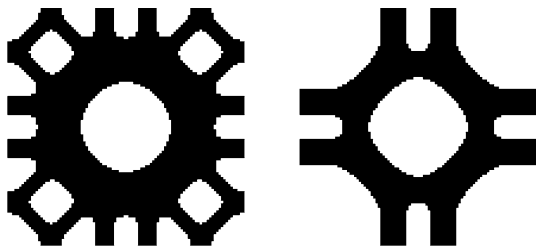
Fig. 62 Benchmark test case 1 of "esoX.m": material bulk modulus maximization design results with 60 and 40% volume constraints obtained from calling esoX(100,100,0.6,0.02,6,1) and esoX(100,100,0.4,0.02,6,1)
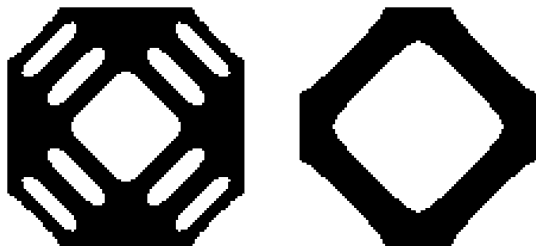
Fig. 63 Benchmark test case 2 of "esoX.m": shear bulk modulus maximization design results with 60 and 40% volume constraints obtained from calling esoX(100,100,0.6,0.02,6,2) and esoX(100,100,0.4,0.02,6,2)

8 Conclusion

This paper has provided a comprehensive review on the development of ESO-type methods, in particular the convergent and mesh-independent BESO method is highlighted. Summaries on recent extensions and applications of the BESO method are drawn for three categories: (a) design of advanced structures, (b) design of material microstructures, and (c) simultaneous design of structures and their underlying materials. It has been shown by the categorized summaries that the BESO method is high efficient and robust in dealing with various design problems. We may draw the conclusion that the BESO method has been recognized as one of the most powerful and effective design tools and widely adopted in both academic researches and engineering applications. This review expects to provide a valuable reference of the BESO method for both academic researchers and industrial designers in structural optimization design.

Compliance with Ethical Standards

Conflict of interest The authors declare that they have no conflict of interest.

Informed Consent All the authors are informed and provided their consent.

Appendix A: Matlab Code "esoL.m" Usisng the BESO Method for the Design of Structures

```matlab
1  function esoL(nelx,nely,volfrac,er,rmin,ctp)
2  %% INITIALIZATION
3  vol = 1; change = 1; ij = 0;
4  x = ones(nely,nelx);
5  %% MATERIAL PROPERTIES
6  E0 = 1; nu = 0.3;
7  %% PREPARE FINITE ELEMENT ANALYSIS
8  A11 = [12 3 -6 -3; 3 12 3 0; -6 3 12 -3; -3 0 -3
       12];
9  A12 = [-6 -3 0 3; -3 -6 -3 -6; 0 -3 -6 3; 3 -6 3
       -6];
10 B11 = [-4 3 -2 9; 3 -4 -9 4; -2 -9 -4 -3; 9 4 -3
       -4];
11 B12 = [ 2 -3 4 -9; -3 2 9 -2; 4 9 2 3; -9 -2 3
       2];
12 KE = 1/(1-nu^2)/24*([A11 A12;A12' A11]+nu*[B11
       B12;B12' B11]);
13 nodenrs = reshape(1:(1+nelx)*(1+nely),1+nely,1+
       nelx);
14 edofVec = reshape(2*nodenrs(1:end-1,1:end-1)+1,
       nelx*nely,1);
15 edofMat = repmat(edofVec,1,8)+repmat([0 1 2*nely
       +[2 3 0 1] -2 -1],nelx*nely,1);
16 iK = reshape(kron(edofMat,ones(8,1))',64*nelx*
       nely,1);
17 jK = reshape(kron(edofMat,ones(1,8))',64*nelx*
       nely,1);
18 %% DEFINE LOADS AND SUPPORTS
19 switch(ctp)
20   case 1 % HALF-MBB BEAM
21     F = sparse(2,1,-1,2*(nely+1)*(nelx+1),1);
22     fixeddofs = union(1:2:2*(nely+1), 2*(nely+1)
         *(nelx+1));
23   case 2 % CANTILEVER
24     F = sparse(2*(nely+1)*(nelx+1)-nely,1,-1,2*(
         nely+1)*(nelx+1),1);
25     fixeddofs = (1:2*(nely+1));
26   case 3 % HALF-WHEEL
27     F = sparse(2*(nely+1)*(nelx/2+1),1,-1,2*(nely
         +1)*(nelx+1),1);
28     fixeddofs = union(2*nely+1:2*(nely+1), 2*(
         nely+1)*(nelx+1));
29 end
30 U = zeros(2*(nely+1)*(nelx+1),1);
31 alldofs = (1:2*(nely+1)*(nelx+1));
32 freedofs = setdiff(alldofs,fixeddofs);
33 %% PREPARE FILTER
34 iH = ones(nelx*nely*(2*(ceil(rmin)-1)+1)^2,1);
35 jH = ones(size(iH)); sH = zeros(size(iH)); k =
       0;
36 for i1 = 1:nelx
37   for j1 = 1:nely
38     e1 = (i1-1)*nely+j1;
39     for i2 = max(i1-(ceil(rmin)-1),1):min(i1+(
         ceil(rmin)-1),nelx)
40       for j2 = max(j1-(ceil(rmin)-1),1):min(j1+(
           ceil(rmin)-1),nely)
41         e2 = (i2-1)*nely+j2; k = k+1; iH(k) = e1;
               jH(k) = e2;
42         sH(k) = max(0,rmin-sqrt((i1-i2)^2+(j1-j2)
               ^2));
43       end
44     end
45   end
46 end
47 H = sparse(iH,jH,sH); Hs = sum(H,2);
48 %% START ITERATION
49 while change > 0.001
50   ij = ij + 1; vol = max(vol*(1-er), volfrac);
51   if ij > 1; olddc = dc; end
52   %% FE-ANALYSIS
53   sK = reshape(KE(:)*max(1e-9,x(:))'*E0,64*nelx*
         nely,1);
54   K = sparse(iK,jK,sK); K = (K+K')/2;
55   U(freedofs) = K(freedofs,freedofs)\F(freedofs)
         ;
56   %% OBJECTIVE FUNCTION AND SENSITIVITY ANALYSIS
57   ce = reshape(sum((U(edofMat)*KE).*U(edofMat)
         ,2),nely,nelx);
58   c(ij) = sum(sum((x.*E0).*ce));
59   dc = (x.*E0).*ce;
60   %% FILTERING/MODIFICATION OF SENSITIVITIES
61   dc(:) = H*dc(:)./Hs;
62   if ij > 1; dc = (dc+olddc)/2.; end
63   %% PRINT RESULTS & PLOT DENSITIES
64   if ij > 10; change =abs(sum(c(ij-9:ij-5))-sum(
         c(ij-4:ij)))/sum(c(ij-4:ij)); end
65   fprintf('It.:%3i Obj.:%8.4f Vol.:%4.3f ch
         .:%4.3f\n',(ij),c(ij),mean(x(:)),change);
66   colormap(gray); imagesc(-x); axis equal; axis
         tight; axis off; pause(1e-6);
67   %% OPTIMALITY CRITERIA UPDATE OF DESIGN
         VARIABLES
68   l1 = min(dc(:)); l2 = max(dc(:));
69   while (l2-l1)/(l1+l2) > 1.0e-9
70     th = (l1+l2)/2.0;
71     x = max(0,sign(dc-th)) ;
72     if mean(x(:)) - vol > 0;
73       l1 = th;
74     else
75       l2 = th;
76     end
77   end
78 end
```

Appendix B: Matlab Code "`esoX.m`" Using the BESO Method for the Design of Material Microstructures

```matlab
1  function esoX(nelx,nely,volfrac,er,rmin,ctp)
2  %% INITIALIZATION
3  x = ones(nely,nelx);
4  x(nely/2:nely/2+1,nelx/2:nelx/2+1) = 0;
5  vol = mean(x(:)); change = 1; ij = 0;
6  qe = cell(3,3); Q = zeros(3,3); dQ = cell(3,3);
7  %% MATERIAL PROPERTIES
8  E0 = 1; nu = 0.3;
9  %% PREPARE FINITE ELEMENT ANALYSIS
10 A11 = [12 3 -6 -3; 3 12 3 0; -6 3 12 -3; -3 0 -3
       12];
11 A12 = [-6 -3 0 3; -3 -6 -3 -6; 0 -3 -6 3; 3 -6 3
       -6];
12 B11 = [-4 3 -2 9; 3 -4 -9 4; -2 -9 -4 -3; 9 4 -3
       -4];
13 B12 = [ 2 -3 4 -9; -3 2 9 -2; 4 9 2 3; -9 -2 3
       2];
14 KE = 1/(1-nu^2)/24*([A11 A12;A12' A11]+nu*[B11
       B12;B12' B11]);
15 nodenrs = reshape(1:(1+nelx)*(1+nely),1+nely,1+
       nelx);
16 edofVec = reshape(2*nodenrs(1:end-1,1:end-1)+1,
       nelx*nely,1);
17 edofMat = repmat(edofVec,1,8)+repmat([0 1 2*nely
       +[2 3 0 1] -2 -1],nelx*nely,1);
18 iK = reshape(kron(edofMat,ones(8,1))',64*nelx*
       nely,1);
19 jK = reshape(kron(edofMat,ones(1,8))',64*nelx*
       nely,1);
20 %% PREPARE FILTER
21 iH = ones(nelx*nely*(2*(ceil(rmin)-1)+1)^2,1);
22 jH = ones(size(iH)); sH = zeros(size(iH)); k =
       0;
23 for i1 = 1:nelx
24   for j1 = 1:nely
25     e1 = (i1-1)*nely+j1;
26     for i2 = max(i1-(ceil(rmin)-1),1):min(i1+(
         ceil(rmin)-1),nelx)
27       for j2 = max(j1-(ceil(rmin)-1),1):min(j1+(
           ceil(rmin)-1),nely)
28         e2 = (i2-1)*nely+j2; k = k+1; iH(k) = e1;
               jH(k) = e2;
29         sH(k) = max(0,rmin-sqrt((i1-i2)^2+(j1-j2)
               ^2));
30       end
31     end
32   end
33 end
34 H = sparse(iH,jH,sH); Hs = sum(H,2);
35 %% PERIODIC BOUNDARY CONDITIONS
36 e0 = eye(3);
37 ufixed = zeros(8,3);
38 U = zeros(2*(nely+1)*(nelx+1),3);
39 alldofs = (1:2*(nely+1)*(nelx+1));
40 n1 = [nodenrs(end,[1,end]),nodenrs(1,[end,1])];
41 d1 = reshape([(2*n1-1);2*n1],1,8);
42 n3 = [nodenrs(2:end-1,1)',nodenrs(end,2:end-1)];
43 d3 = reshape([(2*n3-1);2*n3],1,2*(nelx+nely-2));
44 n4 = [nodenrs(2:end-1,end)',nodenrs(1,2:end-1)];
45 d4 = reshape([(2*n4-1);2*n4],1,2*(nelx+nely-2));
46 d2 = setdiff(alldofs,[d1,d3,d4]);
47 for j = 1:3
48   ufixed(3:4,j) =[e0(1,j),e0(3,j)/2;e0(3,j)/2,e0
         (2,j)]*[nelx;0];
49   ufixed(7:8,j) = [e0(1,j),e0(3,j)/2;e0(3,j)/2,
         e0(2,j)]*[0;nely];
50   ufixed(5:6,j) = ufixed(3:4,j)+ufixed(7:8,j);
51 end
52 wfixed = [repmat(ufixed(3:4,:),nely-1,1); repmat
       (ufixed(7:8,:),nelx-1,1)];
53 %% START ITERATION
54 while change > 0.001
55   ij = ij + 1; vol = max(vol*(1-er), volfrac);
56   if ij > 1; olddc = dc; end
57   %% FE-ANALYSIS
58   sK = reshape(KE(:)*max(1e-9,x(:))'*E0,64*nelx*
         nely,1);
59   K = sparse(iK,jK,sK); K = (K+K')/2;
60   Kr = [K(d2,d2), K(d2,d3)+K(d2,d4); K(d3,d2)+K(
         d4,d2), K(d3,d3)+K(d4,d3)+K(d3,d4)+K(d4,d4
         )];
61   U(d1,:) = ufixed;
62   U([d2,d3],:) = Kr\(-[K(d2,d1); K(d3,d1)+K(d4,
         d1)]*ufixed-[K(d2,d4); K(d3,d4)+K(d4,d4)]*
         wfixed);
63   U(d4,:) = U(d3,:)+wfixed;
64   %% OBJECTIVE FUNCTION AND SENSITIVITY ANALYSIS
65   for i = 1:3
66     for j = 1:3
67       U1 = U(:,i); U2 = U(:,j);
68       qe{i,j} = reshape(sum((U1(edofMat)*KE).*U2(
           edofMat),2),nely,nelx)/(nelx*nely);
69       Q(i,j) = sum(sum((x.*E0).*qe{i,j}));
70       dQ{i,j} = (x.*E0).*qe{i,j};
71     end
72   end
73   switch(ctp)
74     case 1 % BULK MODULUS MAXIMIZATION
75       c(ij) = (Q(1,1)+Q(2,2)+Q(1,2)+Q(2,1));
76       dc = (dQ{1,1}+dQ{2,2}+dQ{1,2}+dQ{2,1});
77     case 2 % SHEAR MODULUS MAXIMIZATION
78       c(ij) = Q(3,3);
79       dc = dQ{3,3};
80   end
81   %% FILTERING/MODIFICATION OF SENSITIVITY
         NUMBERS
82   dc(:) = H*dc(:)./Hs;
83   if ij >10; dc = (dc+olddc)/2.; end
84   %% PRINT RESULTS & PLOT DENSITIES
85   if ij > 10; change = abs(sum(c(ij-9:ij-5))-sum
         (c(ij-4:ij)))/abs(sum(c(ij-4:ij))); end
86   fprintf('It.:%3i Obj.:%8.4f Vol.:%4.3f ch
         .:%4.3f\n',(ij),c(ij),mean(x(:)),change);
87   colormap(gray); imagesc(-x); axis equal; axis
         tight; axis off; pause(1e-6);
88   %% OPTIMALITY CRITERIA
89   l1 = min(dc(:)); l2 = max(dc(:));
90   while (l2-l1)/(l1+l2) > 1.0e-9
91     th = (l1+l2)/2.0;
92     x = max(0,sign(dc-th)) ;
93     if mean(x(:)) - vol > 0;
94       l1 = th;
95     else
96       l2 = th;
97     end
98   end
99 end
```

References

1. Allaire G, Jouve F, Toader AM (2002) A level-set method for shape optimization. CR Math 334(12):1125–1130
2. Andreassen E, Jensen J (2014) Topology optimization of periodic microstructures for enhanced dynamic properties of viscoelastic composite materials. Struct Multidiscip Optim 49(5):695–705
3. Andreassen E, Clausen A, Schevenels M, Lazarov BS, Sigmund O (2011) Efficient topology optimization in matlab using 88 lines of code. Struct Multidiscip Optim 43(1):1–16
4. Ansola R, Canales J, Tárrago JA (2006) An efficient sensitivity computation strategy for the evolutionary structural optimization (ESO) of continuum structures subjected to self-weight loads. Finite Elem Anal Des 42(14):1220–1230
5. Barbero EJ (2010) Introduction to composite materials design. CRC Press, Boca Raton
6. Bendsøe M, Sigmund O (1999a) Material interpolation schemes in topology optimization. Arch Appl Mech 69(9–10):635–654
7. Bendsøe MP (1989) Optimal shape design as a material distribution problem. Struct Optim 1(4):193–202
8. Bendsøe MP, Kikuchi N (1988) Generating optimal topologies in structural design using a homogenization method. Comput Methods Appl Mech Eng 71(2):197–224
9. Bendsøe MP, Sigmund O (1999b) Material interpolation schemes in topology optimization. Arch Appl Mech 69:635–654
10. Bendsøe MP, Sigmund O (2003) Topology optimization: theory, methods and applications. Springer, Berlin
11. Bourdin B, Chambolle A (2003) Design-dependent loads in topology optimization. ESAIM Control Optim Calc Var 9:19–48
12. Bruns T, Tortorelli D (2003) An element removal and reintroduction strategy for the topology optimization of structures and compliant mechanisms. Int J Numer Methods Eng 57(10):1413–1430
13. Cadman J, Zhou S, Chen Y, Li Q (2013) On design of multifunctional microstructural materials. J Mater Sci 48(1):51–66
14. Challis VJ, Roberts AP, Wilkins AH (2008) Design of three dimensional isotropic microstructures for maximized stiffness and conductivity. Int J Solids Struct 45(14–15):4130–4146
15. Challis VJ, Guest JK, Grotowski JF, Roberts AP (2012) Computationally generated cross-property bounds for stiffness and fluid permeability using topology optimization. Int J Solids Struct 49(23–24):3397–3408
16. Chen W, Liu S (2014) Topology optimization of microstructures of viscoelastic damping materials for a prescribed shear modulus. Struct Multidiscip Optim 50(2):287–296
17. Cheng K, Olhoff N (1981) An investigation concerning optimal design of solid elastic plates. Int J Solids Struct 17(3):305–323
18. Chiandussi G (2006) On the solution of a minimum compliance topology optimisation problem by optimality criteria without a priori volume constraint specification. Comput Mech 38(1):77–S99
19. Cho S, Jung HS (2003) Design sensitivity analysis and topology optimization of displacement-loaded non-linear structures. Comput Methods Appl Mech Eng 192(22–23):2539–2553
20. Chu DN, Xie YM, Hira A, Steven GP (1996) Evolutionary structural optimization for problems with stiffness constraints. Finite Elem Anal Des 21(4):239–251
21. Coenen EWC, Kouznetsova VG, Geers MGD (2012) Multi-scale continuous–discontinuous framework for computational-homogenization-localization. J Mech Phys Solids 60(8):1486–1507
22. Da D, Cui X, Long K, Li G (2016) Concurrent topological design of composite structures and the underlying multi-phase materials. Comput Struct. doi:10.1016/j.compstruc.2016.10.006
23. Deaton JD, Grandhi RV (2014) A survey of structural and multidisciplinary continuum topology optimization: post 2000. Struct Multidiscip Optim 49(1):1–38
24. Du J, Olhoff N (2007) Topological design of freely vibrating continuum structures for maximum values of simple and multiple eigenfrequencies and frequency gaps. Struct Multidiscip Optim 34(2):91–110
25. Duysinx P, Bendsøe MP (1998) Topology optimization of continuum structures with local stress constraints. Int J Numer Methods Eng 43(8):1453–1478
26. Edwards C, Kim H, Budd C (2007) An evaluative study on ESO and SIMP for optimising a cantilever tie-beam. Struct Multidiscip Optim 34(5):403–414
27. Eschenauer H, Kobelev V, Schumacher A (1994) Bubble method for topology and shape optimization of structures. Struct Optim 8(1):42–51
28. Feyel F, Chaboche J (2000) FE ^{2} multiscale approach for modelling the elastoviscoplastic behaviour of long fibre sic/ti composite materials. Comput Methods Appl Mech Eng 183(3–4):309–330
29. Fleming J, Lin S, El-Kady I, Biswas R, Ho K (2002) All-metallic three-dimensional photonic crystals with a large infrared bandgap. Nature 417(6884):52–55
30. Fritzen F, Hodapp M (2016) The finite element square reduced (fe^{2R}) method with gpu acceleration: towards three-dimensional two-scale simulations. Int J Numer Methods Eng. doi:10.1002/nme.5188
31. Fritzen F, Leuschner M (2013) Reduced basis hybrid computational homogenization based on a mixed incremental formulation. Comput Methods Appl Mech Eng 260:143–154
32. Fritzen F, Hodapp M, Leuschner M (2014) Gpu accelerated computational homogenization based on a variational approach in a reduced basis framework. Comput Methods Appl Mech Eng 278:186–217
33. Fritzen F, Xia L, Leuschner M, Breitkopf P (2016) Topology optimization of multiscale elastoviscoplastic structures. Int J Numer Methods Eng. doi:10.1002/nme.5122
34. Fujii D, Chen BC, Kikuchi N (2001) Composite material design of two-dimensional structures using the homogenization design method. Int J Numer Methods Eng 50(9):2031–2051
35. Fullwood DT, Niezgoda SR, Adams BL, Kalidindi SR (2010) Microstructure sensitive design for performance optimization. Prog Mater Sci 55(6):477–562
36. Geers MGD, Kouznetsova VG, Brekelmans WAM (2010) Multi-scale computational homogenization: trends and challenges. J Comput Appl Math 234(7):2175–2182
37. Ghabraie K (2015) An improved soft-kill BESO algorithm for optimal distribution of single or multiple material phases. Struct Multidiscipl Optim 52(4):773–790
38. Ghabraie K, Xie YM, Huang X, Ren G (2010) Shape and reinforcement optimization of underground tunnels. J Comput Sci Technol 4(1):51–63
39. Gibiansky L, Sigmund O (2000) Multiphase composites with extremal bulk modulus. J Mech Phys Solids 48(3):461–498
40. Guedes J, Kikuchi N (1990) Preprocessing and postprocessing for materials based on the homogenization method with adaptive finite element methods. Comput Methods Appl Mech Eng 83(2):143–198
41. Guest JK, Prévost JH (2006) Optimizing multifunctional materials: Design of microstructures for maximized stiffness and fluid permeability. Int J Solids Struct 43(22–23):7028–7047
42. Guest JK, Prévost JH (2007) Design of maximum permeability material structures. Comput Methods Appl Mech Eng 196(4–6):1006–1017
43. Hashin Z (1983) Analysis of composite materials: a survey. J Appl Mech 50(3):481–505
44. Hashin Z, Shtrikman S (1962) A variational approach to the theory of the effective magnetic permeability of multiphase materials. J Appl Phys 33(10):3125–3131

45. Hassani B, Hinton E (1998b) A review of homogenization and topology opimization II: analytical and numerical solution of homogenization equations. Comput Struct 69(6):719–738

46. Hinton E, Sienz J (1995) Fully stressed topological design of structures using an evolutionary procedure. Eng Comput 12(3):229–244

47. Huang X, Xie YM (2007a) Bidirectional evolutionary topology optimization for structures with geometrical and material non-linearities. AIAA J 45(1):308–313

48. Huang X, Xie YM (2007b) Convergent and mesh-independent solutions for the bi-directional evolutionary structural optimization method. Finite Elem Anal Des 43(14):1039–1049

49. Huang X, Xie YM (2008a) A new look at ESO and BESO optimization methods. Struct Multidiscip Optim 35(1):89–92

50. Huang X, Xie YM (2008b) Optimal design of periodic structures using evolutionary topology optimization. Struct Multidiscip Optim 36(6):597–606

51. Huang X, Xie YM (2008c) Optimal design of periodic structures using evolutionary topology optimization. Struct Multidiscip Optim 36(6):597–606

52. Huang X, Xie YM (2008d) Topology optimization of nonlinear structures under displacement loading. Eng Struct 30(7): 2057–2068

53. Huang X, Xie YM (2009) Bi-directional evolutionary topology optimization of continuum structures with one or multiple materials. Comput Mech 43(3):393–401

54. Huang X, Xie YM (2010a) Evolutionary topology optimization of continuum structures with an additional displacement constraint. Struct Multidiscip Optim 40(1–6):409–416

55. Huang X, Xie YM (2010b) A further review of ESO type methods for topology optimization. Struct Multidiscip Optim 41(5):671–683

56. Huang X, Xie YM (2010c) Topology optimization of continuum structures: methods and applications. Wiley, Chichester

57. Huang X, Xie YM (2011) Evolutionary topology optimization of continuum structures including design-dependent self-weight loads. Finite Elem Anal Des 47(8):942–948

58. Huang X, Xie YM, Lu G (2007) Topology optimization of energy-absorbing structures. Int J Crashworthiness 12(6):663–675

59. Huang X, Zuo Z, Xie YM (2010) Evolutionary topological optimization of vibrating continuum structures for natural frequencies. Comput Struct 88(5):357–364

60. Huang X, Radman A, Xie YM (2011) Topological design of microstructures of cellular materials for maximum bulk or shear modulus. Comput Mater Sci 50(6):1861–1870

61. Huang X, Xie YM, Jia B, Li Q, Zhou SW (2012) Evolutionary topology optimization of periodic composites for extremal magnetic permeability and electrical permittivity. Struct Multidiscip Optim 46(3):385–398

62. Huang X, Zhou SW, Xie YM, Li Q (2013) Topology optimization of microstructures of cellular materials and composites for macrostructures. Comput Mater Sci 67:397–407

63. Huang X, Li Y, Zhou S, Xie YM (2014) Topology optimization of compliant mechanisms with desired structural stiffness. Eng Struct 79:13–21

64. Huang X, Zhou S, Sun G, Li G, Xie YM (2015) Topology optimization for microstructures of viscoelastic composite materials. Comput Methods Appl Mech Eng 283:503–516

65. Joannopoulos J, Johnson S, Winn J, Meade R (2011) Photonic crystals: molding the flow of light. Princeton University Press, Princeton

66. Kato J, Yachi D, Terada K, Kyoya T (2014) Topology optimization of micro-structure for composites applying a decoupling multi-scale analysis. Struct Multidiscip Optim 49(4): 595–608

67. Kim H, Garcia M, Querin O, Steven GP, Xie YM (2000a) Introduction of fixed grid in evolutionary structural optimisation. Eng Comput 17(4):427–439

68. Kim H, Querin O, Steven GP, Xie YM (2000b) A method for varying the number of cavities in an optimized topology using evolutionary structural optimization. Struct Multidiscip Optim 19(2):140–147

69. Kim H, Querin O, Steven GP, Xie YM (2002a) Improving efficiency of evolutionary structural optimization by implementing fixed grid mesh. Struct Multidiscip Optim 24(6):441–448

70. Kim H, Querin OM, Steven GP, Xie YM (2002b) Determination of an optimal topology with a predefined number of cavities. AIAA J 40(4):739–744

71. Kohn R, Strang G (1986a) Optimal design and relaxation of variational problems (part I). Commun Pure Appl Math 39(1):113–137

72. Kohn R, Strang G (1986b) Optimal design and relaxation of variational problems (part I). Commun Pure Appl Math 39(2):139–182

73. Kohn R, Strang G (1986c) Optimal design and relaxation of variational problems (part I). Commun Pure Appl Math 39(3):353–377

74. Le B, Yvonnet J, He QC (2015) Computational homogenization of nonlinear elastic materials using neural networks. Int J Numer Methods Eng 104(12):1061–1084

75. Le C, Norato J, Bruns T, Ha C, Tortorelli D (2010) Stress-based topology optimization for continua. Struct Multidiscip Optim 41(4):605–620

76. Li Q, Steven GP, Xie YM (1999) On equivalence between stress criterion and stiffness criterion in evolutionary structural optimization. Struct Optim 18(1):67–73

77. Li Q, Steven G, Xie YM (2001) A simple checkerboard suppression algorithm for evolutionary structural optimization. Struct Multidiscip Optim 22(3):230–239

78. Li Q, Steven GP, Xie YM, Querin OM (2004) Evolutionary topology optimization for temperature reduction of heat conducting fields. Int J Heat Mass Transf 47(23):5071–5083

79. Li Y, Huang X, Meng F, Zhou S (2016a) Evolutionary topological design for phononic band gap crystals. Struct Multidiscip Optim 54(3):595–617

80. Li Y, Huang X, Zhou S (2016b) Topological design of cellular phononic band gap crystals. Materials 9(3):186–208

81. Liu Q, Chan R, Huang X (2016) Concurrent topology optimization of macrostructures and material microstructures for natural frequency. Mater Des 106:380–390

82. Liu Y, Jin F, Li Q, Zhou S (2008) A fixed-grid bidirectional evolutionary structural optimization method and its applications in tunnelling engineering. Int J Numer Methods Eng 73(12):1788–1810

83. Lu M, Feng L, Chen Y (2009) Phononic crystals and acoustic metamaterials. Mater Today 12(12):34–42

84. Luo Z, Wang M, Wang S, Wei P (2008) A level set-based parameterization method for structural shape and topology optimization. Int J Numer Methods Eng 76(1):1–26

85. Manickarajah D, Xie YM, Steven GP (1998) An evolutionary method for optimization of plate buckling resistance. Finite Elem Anal Des 29(3):205–230

86. Maute K, Schwarz S, Ramm E (1998) Adaptive topology optimization of elastoplastic structures. Struct Optim 15(2):81–91

87. McKeown JJ (1997) A note on the equivalence between maximum stiffness and maximum strength trusses. Eng Optim 29(1–4):443–456

88. Meng F, Huang X, Jia B (2015) Bi-directional evolutionary optimization for photonic band gap structures. J Comput Phys 302:393–404

89. Meng F, Li S, Lin H, Jia B, Huang X (2016) Topology optimization of photonic structures for all-angle negative refraction. Finite Elem Anal Des 117:46–56

90. Michel JC, Moulinec H, Suquet P (1999) Effective properties of composite materials with periodic microstructure: a computational approach. Comput Methods Appl Mech Eng 172(1–4):109–143

91. Michell AGM (1904) Lviii. the limits of economy of material in frame-structures. Lond Edinb Dublin Philos Mag J Sci 8(47):589–597

92. Munk D, Vio G, Steven GP (2016) A simple alternative formulation for structural optimisation with dynamic and buckling objectives. Struct Multidiscip Optim. doi:10.1007/s00158-016-1544-9

93. Neves MM, Rodrigues H, Guedes JM (2000) Optimal design of periodic linear elastic microstructures. Comput Struct 76(1):421–429

94. Neves MM, Sigmund O, Bendsøe MP (2002) Topology optimization of periodic microstructures with a penalization of highly localized buckling modes. Int J Numer Methods Eng 54(6):809–834

95. Nguyen T, Ghabraie K, Tran-Cong T (2014) Applying bi-directional evolutionary structural optimisation method for tunnel reinforcement design considering nonlinear material behaviour. Comput Geotech 55:57–66

96. Niu B, Yan J, Cheng G (2009) Optimum structure with homogeneous optimum cellular material for maximum fundamental frequency. Struct Multidiscip Optim 39(2):115–132

97. Norato JA, Bendsøe MP, Haber RB, Tortorelli DA (2007) A topological derivative method for topology optimization. Struct Multidiscip Optim 33(4–5):375–386

98. Pedersen N (2000) Maximization of eigenvalues using topology optimization. Struct Multidiscip Optim 20(1):2–11

99. Pennec Y, Vasseur J, Djafari-Rouhani B, Dobrzyński L, Deymier P (2010) Two-dimensional phononic crystals: examples and applications. Surf Sci Rep 65(8):229–291

100. Picelli R, Vicente W, Pavanello R (2015a) Bi-directional evolutionary structural optimization for design-dependent fluid pressure loading problems. Eng Optim 47(10):1324–1342

101. Picelli R, Vicente W, Pavanello R, Xie YM (2015b) Evolutionary topology optimization for natural frequency maximization problems considering acoustic–structure interaction. Finite Elem Anal Des 106:56–64

102. Picelli R, van Dijk R, Vicente W, Pavanello R, Langelaar M, van Keulen F (2016) Topology optimization for submerged buoyant structures. Eng Optim. doi:10.1080/0305215X.2016.1164147

103. Prager W, Rozvany G (1977) Optimal layout of grillages. J Struct Mech 5(1):1–18

104. Proos K, Steven GP, Querin O, Xie YM (2001) Stiffness and inertia multicriteria evolutionary structural optimisation. Eng Comput 18(7):1031–1054

105. Querin O, Steven GP, Xie YM (2000a) Evolutionary structural optimisation using an additive algorithm. Finite Elem Anal Des 34(3):291–308

106. Querin OM (1997) Evolutionary structural optimisation: stress based formulation and implementation. Ph.D. thesis, Department of Aeronautical Engineering, University of Sydney, Australia

107. Querin OM, Steven GP, Xie YM (1998) Evolutionary structural optimisation (ESO) using a bidirectional algorithm. Eng Comput 15(8):1031–1048

108. Querin OM, Young V, Steven GP, Xie YM (2000b) Computational efficiency and validation of bi-directional evolutionary structural optimization. Comput Methods Appl Mech Eng 189(2):559–573

109. Radman A, Huang X, Xie YM (2013a) Topological optimization for the design of microstructures of isotropic cellular materials. Eng Optim 45(11):1331–1348

110. Radman A, Huang X, Xie YM (2013b) Topology optimization of functionally graded cellular materials. J Mater Sci 48(4):1503–1510

111. Radman A, Huang X, Xie YM (2014a) Maximizing stiffness of functionally graded materials with prescribed variation of thermal conductivity. Comput Mater Sci 82:457–463

112. Radman A, Huang X, Xie YM (2014b) Topological design of microstructures of multi-phase materials for maximum stiffness or thermal conductivity. Comput Mater Sci 91:266–273

113. Ren G, Smith J, Tang J, Xie YM (2005) Underground excavation shape optimization using an evolutionary procedure. Comput Geotech 32(2):122–132

114. Ren G, Zuo Z, Xie YM, Smith J (2014) Underground excavation shape optimization considering material nonlinearities. Comput Geotech 58:81–87

115. Rietz A (2001) Sufficiency of a finite exponent in simp (power law) methods. Struct Multidiscip Optim 21(2):159–163

116. Rozvany G (1972a) Grillages of maximum strength and maximum stiffness. Int J Mech Sci 14(10):651–666

117. Rozvany G (1972b) Optimal load transmission by flexure. Comput Methods Appl Mech Eng 1(3):253–263

118. Rozvany G, Zhou M, Sigmund O (1994) Optimization of topology. In: Adeli H (ed) Advances in design optimization. Chapman & Hall, London, pp 340–399

119. Rozvany GI, Querin OM (2002) Combining ESO with rigorous optimality criteria. Int J Veh Des 28(4):294–299

120. Rozvany GIN (2009) A critical review of established methods of structural topology optimization. Struct Multidiscip Optim 37(3):217–237

121. Schwarz S, Maute K, Ramm E (2001) Topology and shape optimization for elastoplastic structural response. Comput Methods Appl Mech Eng 190(15–17):2135–2155

122. Sethian JA, Wiegmann A (2000) Structural boundary design via level set and immersed interface methods. J Comput Phys 163(2):489–528

123. Sigmund O (1994) Materials with prescribed constitutive parameters: an inverse homogenization problem. Int J Solids Struct 31(17):2313–2329

124. Sigmund O (1997) On the design of compliant mechanisms using topology optimization. J Struct Mech 25(4):493–524

125. Sigmund O (2000) New class of extremal composites. J Mech Phys Solids 48(2):397–428

126. Sigmund O (2001) A 99 line topology optimization code written in matlab. Struct Multidiscip Optim 21(2):120–127

127. Sigmund O, Maute K (2013) Topology optimization approaches: a comparative review. Struct Multidiscip Optim 48(6):1031–1055

128. Sigmund O, Petersson J (1998) Numerical instabilities in topology optimization: a survey on procedures dealing with checkerboards, mesh-dependencies and local minima. Struct Optim 16(1):68–75

129. Sigmund O, Torquato S (1997) Design of materials with extreme thermal expansion using a three-phase topology optimization method. J Mech Phys Solids 45(6):1037–1067

130. Sokolowski J, Zochowski A (1999) On the topological derivative in shape optimization. SIAM J Control Optim 37(4):1251–1272

131. Steven GP, Li Q, Xie YM (2000) Evolutionary topology and shape design for general physical field problems. Comput Mech 26(2):129–139

132. Stolpe M, Svanberg K (2001a) An alternative interpolation scheme for minimum compliance topology optimization. Struct Multidiscip Optim 22(2):116–124

133. Stolpe M, Svanberg K (2001b) On the trajectories of penalization methods for topology optimization. Struct Multidiscip Optim 21(2):128–139

134. Su W, Liu S (2010) Size-dependent optimal microstructure design based on couple-stress theory. Struct Multidiscip Optim 42(2):243–254

135. Tanskanen P (2002) The evolutionary structural optimization method: theoretical aspects. Comput Methods Appl Mech Eng 191(47–48):5485–5498

136. Theocaris PS, Stavroulaki GE (1999) Optimal material design in composites: an iterative approach based on homogenized cells. Comput Methods Appl Mech Eng 169(1–2):31–42

137. Van Dijk N, Maute K, Langelaar M, Van Keulen F (2013) Level-set methods for structural topology optimization: a review. Struct Multidiscip Optim 48(3):437–472

138. Vicente W, Picelli R, Pavanello R, Xie YM (2015) Topology optimization of frequency responses of fluid-structure interaction systems. Finite Elem Anal Des 98:1–13

139. Vicente W, Zuo Z, Pavanello R, Calixto T, Picelli R, Xie YM (2016) Concurrent topology optimization for minimizing frequency responses of two-level hierarchical structures. Comput Methods Appl Mech Eng 301:116–136

140. Wadley H, Fleck N, Evans A (2003) Fabrication and structural performance of periodic cellular metal sandwich structures. Compos Sci Technol 63(16):2331–2343

141. Wang F, Sigmund O, Jensen J (2014a) Design of materials with prescribed nonlinear properties. J Mech Phys Solids 69(1):156–174

142. Wang MY, Wang X, Guo D (2003) A level set method for structural topology optimization. Comput Methods Appl Mech Eng 192(1–2):227–246

143. Wang Y, Luo Z, Zhang N, Kang Z (2014b) Topological shape optimization of microstructural metamaterials using a level set method. Comput Mater Sci 87:178–186

144. Xia L (2016) Multiscale structural topology optimization. Elsevier-ISTE, London

145. Xia L, Breitkopf P (2014a) Concurrent topology optimization design of material and structure within fe^2 nonlinear multiscale analysis framework. Comput Methods Appl Mech Eng 278:524–542

146. Xia L, Breitkopf P (2014b) A reduced multiscale model for nonlinear structural topology optimization. Comput Methods Appl Mech Eng 280:117–134

147. Xia L, Breitkopf P (2015a) Design of of materials using topology optimization and energy-based homogenization approach in matlab. Struct Multidiscip Optim 52(6):1229–1241

148. Xia L, Breitkopf P (2015b) Multiscale structural topology optimization with an approximate constitutive model for local material microstructure. Comput Methods Appl Mech Eng 286:147–167

149. Xia L, Breitkopf P (2016) Recent advances on topology optimization of multiscale nonlinear structures. Arch Comput Methods Eng. doi:10.1007/s11831-016-9170-7

150. Xia L, Raghavan B, Breitkopf P, Zhang W (2013) Numerical material representation using proper orthogonal decomposition and diffuse approximation. Appl Math Comput 224:450–462

151. Xia L, Fritzen F, Breitkopf P (2016) Evolutionary topology optimization of elastoplastic structures. Struct Multidiscip Optim. doi:10.1007/s00158-016-1523-1

152. Xia L, Raghavan B, Breitkopf P (2017) Towards surrogate modeling of material microstructures through the processing variables. Appl Math Comput 294:157–168

153. Xia Q, Shi T (2016a) Optimization of structures with thin-layer functional device on its surface through a level set based multiple-type boundary method. Comput Methods Appl Mech Eng 311:56–70

154. Xia Q, Shi T (2016b) Topology optimization of compliant mechanism and its support through a level set method. Comput Methods Appl Mech Eng 305:359–375

155. Xia Q, Wang M, Wang S, Chen S (2006a) Semi-lagrange method for level-set-based structural topology and shape optimization. Struct Multidiscip Optim 31(6):419–429

156. Xia Q, Shi T, Wang M (2011) A level set based shape and topology optimization method for maximizing the simple or repeated first eigenvalue of structure vibration. Struct Multidiscip Optim 43(4):473–485

157. Xia Q, Shi T, Liu S, Wang M (2012) A level set solution to the stress-based structural shape and topology optimization. Comput Struct 90–91:55–64

158. Xia Q, Wang M, Shi T (2014) A level set method for shape and topology optimization of both structure and support of continuum structures. Comput Methods Appl Mech Eng 272:340–353

159. Xia Z, Zhang Y, Ellyin F (2003) A unified periodical boundary conditions for representative volume elements of composites and applications. Int J Solids Struct 40(8):1907–1921

160. Xia Z, Zhou C, Yong Q, Wang X (2006b) On selection of repeated unit cell model and application of unified periodic boundary conditions in micro-mechanical analysis of composites. Int J Solids Struct 43(2):266–278

161. Xie YM, Steven GP (1992) Shape and layout optimization via an evolutionary procedure. In: Proceedings of the international conference on computational engineering science

162. Xie YM, Steven GP (1993) A simple evolutionary procedure for structural optimization. Comput Struct 49(5):885–896

163. Xie YM, Steven GP (1996) Evolutionary structural optimization for dynamic problems. Comput Struct 58(6):1067–1073

164. Xie YM, Steven GP (1997) Evolutionary structural optimization. Springer, London

165. Xie YM, Zuo ZH, Huang X, Rong JH (2012) Convergence of topological patterns of optimal periodic structures under multiple scales. Struct Multidiscip Optim 46(1):41–50

166. Xie YM, Yang X, Shen J, Yan X, Ghaedizadeh A, Rong J, Huang X, Zhou S (2014) Designing orthotropic materials for negative or zero compressibility. Int J Solids Struct 51(23):4038–4051

167. Xu B, Xie YM (2015) Concurrent design of composite macrostructure and cellular microstructure under random excitations. Compos Struct 123:65–77

168. Xu B, Jiang J, Xie YM (2015b) Concurrent design of composite macrostructure and multi-phase material microstructure for minimum dynamic compliance. Compos Struct 128:221–233

169. Xu B, Huang X, Xie YM (2016a) Two-scale dynamic optimal design of composite structures in the time domain using equivalent static loads. Compos Struct 142:335–345

170. Xu B, Huang X, Zhou S, Xie YM (2016b) Concurrent topological design of composite thermoelastic macrostructure and microstructure with multi-phase material for maximum stiffness. Compos Struct 150:84–102

171. Yan X, Huang X, Zha Y, Xie YM (2014) Concurrent topology optimization of structures and their composite microstructures. Comput Struct 133:103–110

172. Yan X, Huang X, Sun G, Xie YM (2015) Two-scale optimal design of structures with thermal insulation materials. Compos Struct 120:358–365

173. Yang X, Huang X, Rong J, Xie YM (2013) Design of 3D orthotropic materials with prescribed ratios for effective youngâĂŹs moduli. Comput Mater Sci 67:229–237

174. Yang XY, Xie YM, Steven GP, Querin OM (1999a) Bidirectional evolutionary method for stiffness optimization. AIAA J 37(11):1483–1488

175. Yang XY, Xie YM, Steven GP, Querin OM (1999b) Topology optimization for frequencies using an evolutionary method. J Struct Eng 125(12):1432–1438

176. Yang XY, Xie YM, Liu JS, Parks GT, Clarkson PJ (2002) Perimeter control in the bidirectional evolutionary optimization method. Struct Multidiscip Optim 24(6):430–S440
177. Yang XY, Xie YM, Steven GP (2005) Evolutionary methods for topology optimisation of continuous structures with design dependent loads. Comput Struct 83(12):956–963
178. Yi YM, Park SH, Youn SK (2000) Design of microstructures of viscoelastic composites for optimal damping characteristics. Int J Solids Struct 37(35):4791–4810
179. Yoon G, Kim Y (2007) Topology optimization of material-nonlinear continuum structures by the element connectivity parameterization. Int J Numer Methods Eng 69(10):2196–2218
180. Young V, Querin OM, Steven GP, Xie YM (1999) 3D and multiple load case bi-directional evolutionary structural optimization (BESO). Struct Optim 18(2–3):183–192
181. Yvonnet J, Gonzalez D, He QC (2009) Numerically explicit potentials for the homogenization of nonlinear elastic heterogeneous materials. Comput Methods Appl Mech Eng 198(33–36):2723–2737
182. Yvonnet J, Monteiro E, He QC (2013) Computational homogenization method and reduced database model for hyperelastic heterogeneous structures. Int J Multiscale Comput Eng 11(3):201–225
183. Zhou M, Rozvany G (2001) On the validity of ESO type methods in topology optimization. Struct Multidiscip Optim 21(1):80–83
184. Zhou M, Rozvany GIN (1991) The COC algorithm, part II: topological, geometrical and generalized shape optimization. Comput Methods Appl Mech Eng 89(1–3):309–336
185. Zhou S, Cadman J, Chen Y, Li W, Xie YM, Huang X, Appleyard R, Sun G, Li Q (2012) Design and fabrication of biphasic cellular materials with transport properties-a modified bidirectional evolutionary structural optimization procedure and matlab program. Int J Heat Mass Transf 55(25):8149–8162
186. Zhu J, Zhang W, Qiu K (2007) Bi-directional evolutionary topology optimization using element replaceable method. Comput Mech 40(1):97–109
187. Zhu J, Zhang W, Xia L (2015) Topology optimization in aircraft and aerospace structures design. Arch Comput Methods Eng. doi:10.1007/s11831-015-9151-2
188. Zuo Z, Huang X, Rong J, Xie YM (2013a) Multi-scale design of composite materials and structures for maximum natural frequencies. Mater Des 51:1023–1034
189. Zuo ZH, Xie YM (2014) Evolutionary topology optimization of continuum structures with a global displacement control. Comput Aided Des 56:58–67
190. Zuo ZH, Xie YM, Huang X (2010) An improved bi-directional evolutionary topology optimization method for frequencies. Int J Struct Stab Dyn 10(01):55–75
191. Zuo ZH, Xie YM, Huang X (2011) Reinventing the wheel. J Mech Des 133(2):024,502
192. Zuo ZH, Huang X, Yang X, Rong JH, Xie YM (2013b) Comparing optimal material microstructures with optimal periodic structures. Comput Mater Sci 69:137–147